UNIVERSITY OF NAIROBI

SOLAR-DRIVEN PHOTOCATALYTIC ACTIVITY OF PORPHYRIN SENSITIZED TiO$_2$ IN METHYLENE BLUE DEGRADATION AND SACRIFICIAL HYDROGEN GENERATION

BY

OTIENO SEBASTIAN OLOO

I56/88735/2016

A Thesis Submitted for Examination in Partial Fulfilment of the Requirements for Award of the Degree of Master of Science in Analytical Chemistry of the University of Nairobi

2020

DECLARATION

I declare that this thesis is my original work and has not been submitted elsewhere for examination, award of a degree or publication. Where other people's work or my own work has been used, this has properly been acknowledged and referenced in accordance with the University of Nairobi's requirements.

Signed .... Date ....11/09/2020....

Otieno Sebastian Oloo

I56/88735/2016

Department of Chemistry

School of Physical Sciences

University of Nairobi.
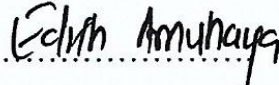
This thesis is submitted for examination with our approval as the research supervisors:

	Signed	Date
Dr. Solomon Derese		11/09/2020
Department of Chemistry-UON		
P.O. Box 30197-00100		
Dr. Edith K. Amuhaya	Edith Amuhaya	11-9-2020
Department of Pharmacy-USIU-Africa		
P.O. Box 14634-00800		
Dr. Ruth Odhiambo		14/09/2020
Department of Chemistry- UON		
P.O. Box 30197-00100		

DEDICATION

I dedicate this thesis to my beloved mum. Mum had immense influence in my academic journey supporting me and encouraging me all the way from a tender age.

ACKNOWLEDGEMENTS

ABSTRACT

Access to clean water and sustainable energy is increasingly becoming limited due to rapid population growth and industrial activities which are highly polluting and energy intensive. One approach that is currently being pursued to access clean water and generate energy is photocatalysis. A semiconductor that has been pursued for such application is TiO_2. However, TiO_2 is a wide bandgap semiconductor which suffers from poor activity or no activity at all in the visible spectrum limiting its use of solar radiation. Several approaches have been employed with the aim of extending the absorption profile of TiO_2. Among these is depositing porphyrins on TiO_2 surface. Porphyrins have excellent absorption in the visible spectrum. The porphyrin-TiO_2 (P-TiO_2) photocatalysts can utilize a broader spectrum of the solar energy in photocatalysis. In this study, the photocatalytic activity of the P-TiO_2 composites versus bare TiO_2 were evaluated and the influence of metallated porphyrin over free base porphyrin in photosensitization of TiO_2 for photocatalysis established. *Meso*-tetra (4-bromophenyl)porphyrin and *meso*-tetra (5-bromo-2-thienyl)porphyrin and their indium, zinc and gallium complexes were synthesized. The synthesized porphyrins were characterized using CHN elemental analysis, ^{1}H-NMR, mass spectrometry and UV/Vis spectroscopy. Density functional theory (DFT) and time dependent density functional theory (TD-DFT) calculations were performed on the porphyrins to gain insight into their electron injection abilities. The calculations revealed the suitability of the porphyrins for electron injection based on the position of their lowest unoccupied molecular orbitals being higher than the TiO_2 conduction band. The photocatalytic activity of the synthesized porphyrins on TiO_2 were investigated by methylene blue (MB, a model organic waste) degradation experiments and hydrogen generation under irradiation by solar simulator. Metalloporphyrin-TiO_2 systems showed better degradation efficiency than freebase porphyrin-TiO_2 systems. However, in hydrogen generation, freebase porphyrin-TiO_2 systems were better compared to the metalloporphyrin-TiO_2 systems. This study showed the porphyrin-TiO_2 systems had enhanced photocatalytic activity over bare TiO_2 hence has potential application in degradation of organic pollutants in water as well as generation of hydrogen, a clean source of energy.

TABLE OF CONTENTS

LIST OF TABLES

LIST OF FIGURES

LIST OF SCHEMES

LIST OF ABBREVIATIONS

AOP	Advanced oxidation processes
CB	Conduction Band
ClGa	Chloro Galium
ClIn	Chloro Indium
DFT	Density Functional Theory
DSSC	Dye-Sensitized Solar Cells
GHG	Greenhouse Gases
HOMO	Highest Occupied Molecular Orbital
ISC	Intersystem Crossing
IRENA	International Renewable Energy Agency
LUMO	Lowest Unoccupied Molecular Orbital
MB	Methylene Blue
Mtoe	Millions of Tonnes of Oil Equivalent
PACT	Photodynamic Antimicrobial Chemotherapy
PDT	Photodynamic Therapy
POPs	Persistent Organic Pollutants
ROS	Reactive Oxygen Species
SED	Sacrificial Electron Donor
SolSim	Solar Simulator
SSA	Sub Saharan Africa
TDDFT	Time- Dependent Density Functional Theory
TPP	Tetraphenylporphyrin
VB	Valency Band

CHAPTER ONE

INTRODUCTION

1.1. Background to the Study

Water is life, a timeless adage that cannot be over-emphasized. Fresh water is a vital component for the survival of all living organisms. United Nations' world water report of 2019 recognizes access to clean water and sanitation as a fundamental human right and one of the main indicators of Sustainable Development Goals (World Water Development Report, 2019). Despite water covering nearly two thirds of the earth's surface, access to clean drinking water remains a challenge (Cosgrove & Loucks, 2015). This is mainly due to rapid population growth which has increased the stress on available fresh water sources and its pollution. Surface water sources like lakes, rivers and oceans have continually been contaminated through human activities. The main sources of water pollution are eroded soil particles, industrial effluents, urban waste effluents, microbial landfill contents, agricultural and domestic waste effluents (Goel, 2006; Hammer, 1989; Sykes & Skinner, 2015). These effluents are rich in pollutants which have significant effects on human health and ecosystem when consumed making water unsafe for use (Wright *et al*., 2004).

Eliminating pollutants from waterways and water resources has mainly focused on conventional techniques such as biodegradation, steam stripping, adsorption, flocculation and chemical methods like chlorination amongst others (Adams *et al*., 2002; Jiang & Adams, 2006; Stackelberg *et al*., 2007; Zhou *et al*., 2014). These techniques have not proven successful in removing total hazardous potential of the pollutants (Li *et al.*, 2008). In particular, persistent organic pollutants (POPs) which are capable of bio accumulating in human and animal tissues have often been found in drinking water (Miranda-García *et al*., 2011; Oller *et al.*, 2011). It is therefore desirable to develop advanced water treatment technologies which are highly efficient even for POPs.

On the other hand, rapid growth in world population and increased industrial activities have led to a steady rise in global energy consumption (Chow, 2003; Fyfe *et al*., 1993; Hossain, 2012). According to the BP Statistical Review of World Energy, global consumption stands at 13.9 Mtoe and this figure is expected to double by the year 2050 (BP Statistical Review of World Energy 2019). Currently, 90% of global energy running the transport and industrial sector come from fossil

fuels. This has led to increased emission of greenhouse gases (GHGs) as well as significant depletion of carbon-based sources of energy that could have been alternatively used to produce valuable chemicals (Dougherty *et al*., 2009; Perera, 2017). The key to reduction of emissions (NO_x, SO_x and GHGs) is by increasing the efficiency in energy production and consumption while reducing fossil fuel component in the energy mix (Hirscher, 2010). There is a crucial need to allocate clean renewable source of energy a significant share in the future energy mix in order to mitigate effects of fossil fuel consumption.

Advanced oxidation processes (AOPs) like photocatalysis have been employed extensively in the decomposition of hazardous and persistent organic pollutants as well as generation of hydrogen from sacrificial electron donors (SED) in aqueous media. AOPs mechanism of action is based on photocatalytic processes within certain semiconductors which generate active radicals on absorption of light at an appropriate wavelength destroying organic matter and/or splitting water to generate hydrogen (Gaya & Abdullah, 2008; Kim *et al*., 2014; Leung *et al*., 2010; Teh & Mohamed, 2011). A semiconductor that has been pursued for such application is TiO_2. However, TiO_2 being a wide bandgap semiconductor has its application restricted to the UV region of the solar spectrum (Dong *et al*., 2015). In order to extend the photo response spectrum of TiO_2 photocatalyst into the visible spectrum, photosensitization with porphyrin dyes has been one successful method (Chang et al., 2009; Meng et al., 2007).

This research, therefore, investigated the photocatalytic efficiency of a series of different metal porphyrin complexes and the corresponding free base porphyrins after adsorption on TiO_2. *Meso*-tetra(4-bromophenyl)porphyrin (PP1) and *meso*-tetra(5-bromo-2-thienyl)porphyrin (PP2) and their In(III), Zn(II) and Ga(III) metal complexes were synthesized and characterized. To understand the intrinsic optical properties of the porphyrins, quantum chemical calculations were carried out using the density functional theory (DFT) and time-dependent density functional theory (TD−DFT) methods. The porphyrins were adsorbed on nanometric TiO_2 to yield porphyrin-TiO_2 (P−TiO_2) nanocomposites. The photocatalytic activities of the P−TiO_2 nanocomposites and Degussa P25 (TiO_2) and their suitability to degrade methylene blue (MB) and generate hydrogen under irradiation by a solar simulator (AM 1.5) were investigated.

1.2. Statement of the Problem

To realize any meaningful development, energy and water problems must be resolved. However, access to clean water for domestic use (Cosgrove & Loucks, 2015) and sustainable energy (Fyfe *et al*., 1993; Perera, 2017) is increasingly becoming a priority due to rapid population growth and industrial activities which are highly polluting and energy intensive (Liu *et al*., 2009).

Water pollution by organic chemicals especially from industrial wastewaters and surface runoffs from agricultural fields is a growing concern (Goel, 2006; Hammer, 1989; Sykes & Skinner, 2015). Lately, conventional techniques frequently used to remove organic pollutants from water channels have become ineffective (Adams *et al*., 2002; Jiang & Adams, 2006; Oller *et al*., 2011; Stackelberg *et al*., 2007; Zhou *et al*., 2014). Recalcitrant organic pollutants have continued to pose a great threat to the environment (Gaya & Abdullah, 2008; Li *et al*., 2008; Miranda-García *et al*., 2011). It is therefore desirable to develop new advanced water treatment technologies which are highly efficient against all common organic pollutants.

On the other hand, a shortfall of clean, secure and sustainable energy supply is now recognized as a global problem (Global Energy Transformation, 2019; Lanterna & Scaiano, 2017; Salameh, 2003) . Steadily increasing growth in global energy consumption from fossil fuels has led to substantial depletion of the most easily exploited carbon-based energy sources and increased the emission of greenhouse gases into the atmosphere (Perera, 2017). Climate change, increasing energy prices due to depletion of energy resources and foreign oil dependency are just but some of the consequences of fossil fuel consumption (Dougherty *et al*., 2009). Therefore, there is a crucial need to allocate clean renewable sources of energy like hydrogen a significant share in the future energy mix in order to effectively mitigate effects of fossil fuel consumption (Hirscher, 2010; Teichmann *et al*., 2011; Winter & Nitsch, 2012).

It is for these reasons that this project developed P-TiO$_2$ photocatalysts that were used to degrade methylene blue (model organic waste) and also generate hydrogen under conditions of solar simulation.

1.3. Objectives of the Study

1.3.1. General Objective

The general objective of this study was to extend the photocatalytic activity of TiO_2 into the visible region by depositing on its surface suitable porphyrin dyes for application in degradation of organic pollutant and hydrogen generation.

1.3.2. Specific Objectives

The specific objectives of this study were to:

i. Synthesize and characterize free base porphyrins and their Zn, In and Ga complexes.
ii. Determine the optical properties of the porphyrin dyes by computational and photophysical studies.
iii. Establish the photocatalytic activity of the porphyrin-TiO_2 composite.

1.4. Justification and Significance of the Study

Development of sustainable twin solution that addresses both organic chemical pollution in water and the global energy problem is relevant. Photocatalysis technology is one such approach. Photocatalytic degradation of organic pollutants and hydrogen generation has been attractive and the most rewarding due to abundance of water and favourable conditions of only sunlight and a semiconductor photocatalyst (Yadav *et al*., 2018).

TiO_2 is a widely known semiconductor for its widespread applications in sunscreens, paints, photovoltaics and environmental remediation (Daghrir *et al*., 2013; Elhage *et al*., 2019; Horng-Huey *et al*., 2012; Yaron, 2010; Zhang *et al*., 2016). These applications are credited to its wide distribution in terms of its commercially exploitable reserves, inertness, good photoconductivity properties, low toxicity as well as high photo-efficiency and activity (Dong *et al*., 2015; Khan & Cao, 2013; Senarathna *et al*., 2017; Taicheng *et al*., 2008). However, TiO_2 is a wide bandgap semiconductor. It predominantly absorbs light in the UV region (< 400 nm) of the solar spectrum taking advantage of only 5% of the solar energy striking the earth's surface (Dong *et al*., 2015). Low sensitivity to photons in the visible spectrum which constitutes about 41% of solar energy pose a significant disadvantage to its practical application (Schultz & Yoon, 2014).

Doping with narrow bandgap semiconductors, decorating TiO_2 surface with nanoparticles and dye sensitization are some of the modification strategies that have been employed in order to shift the optical response of TiO_2 based photocatalysts (Dong *et al*., 2015; Elhage *et al*., 2019). Because of the difficulty in preparing doping materials and the need for lattice exchange at very high temperatures, dye sensitization has drawn much attention(Dong *et al*., 2015). Ruthenium based sensitizers were extensively used initially, but because of their undesirable environmental impact and high cost, they have since been gradually replaced by non-toxic organic dyes like porphyrins (Altobello *et al*., 2004; Polo *et al*., 2004).

Photocatalysis by dye sensitization of a semiconductor has previously posted successful results especially in dye-sensitized solar cells (DSSCs) (Campbell *et al*., 2007; Grätzel, 2003; Polo *et al*., 2004). Over the years, porphyrin dyes have gained application in TiO_2 based DSSCs registering conversion efficiencies of up to over 5% (Campbell *et al*., 2007). However, similar levels of success have not been achieved in degradation of organic pollutants and generation of hydrogen sparking continuous research along these topics (Lanterna & Scaiano, 2017). This research therefore focussed in evaluating the efficiency of the photocatalytic activity of porphyrin-TiO_2 (P-TiO_2) nanocomposites in comparison to TiO_2 alone. Previous research has shown that peripheral substituents influence the efficiency of P-TiO_2 system depending on strength of the polar groups involved and the position of the substituents (Wang *et al*., 2010). However, it is still unclear the critical role played by the central metal in porphyrin complexes in a photocatalytic process involving P-TiO_2 system.

CHAPTER TWO

LITERATURE REVIEW

2.1. Water Crisis - Organic Pollutants

In recent years, demand for the world's most important and precious natural resource, water, has increasingly been on the rise. This has created a global water crisis which is growing at an alarming rate (Rogers, *et al*., 2005; World Water Development Report 2019, 2019). In particular, the world's burgeoning population and the consequent increase in water consumption and sanitation demands has played a crucial role intensifying this problem (Cai & Rosegrant, 2002; Rosegrant *et al*., 2002). Agriculture, from which the growing population depends on for food is competing for this scarce resource with industrial, environmental and household use (Subramaniam *et al*., 2012). In addition, the available water sources are under continuous threat from human, industrial, and agricultural contaminants (Novotny, 1994; Sharma & Sanghi, 2012). Figure 2.1 gives a summary of some of the sources of contaminants in water and their movement into different water reservoirs of the hydrologic cycle.
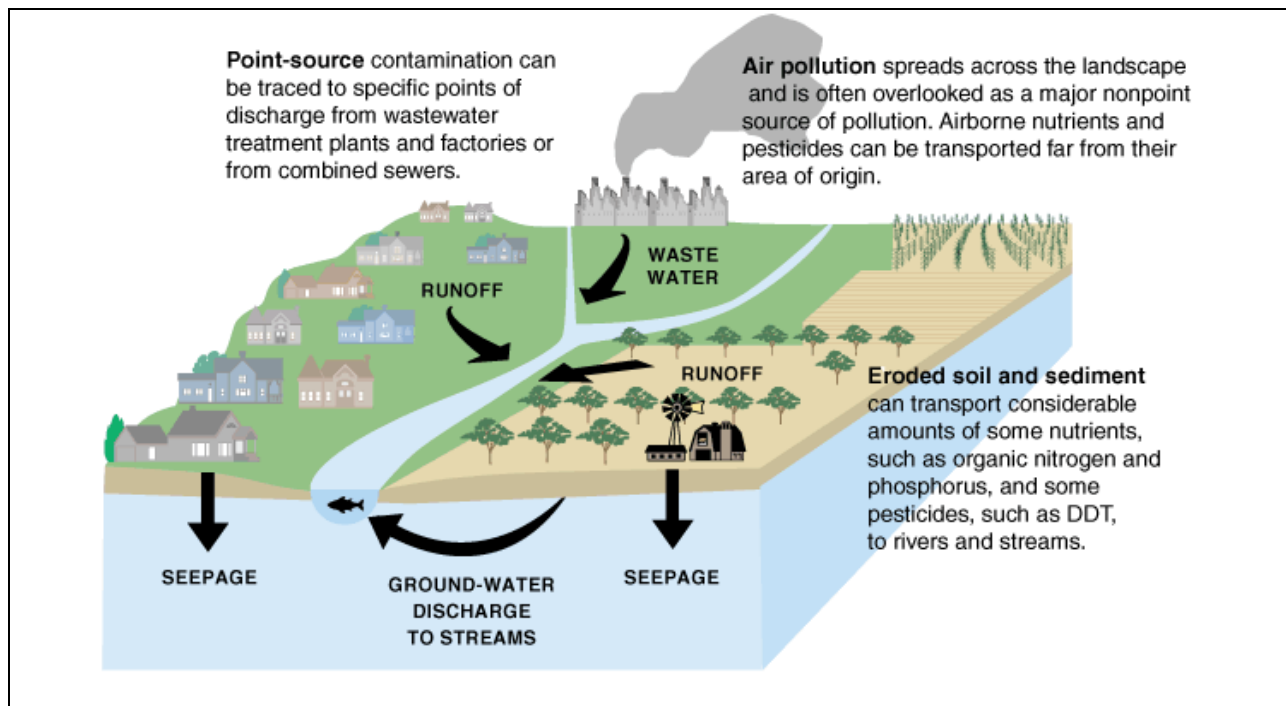
Figure 2.1. Sources of water pollutants (Kamala *et al*., 2018)

Human activities are generating and disposing more waste today than any other time. Toxic contaminants such as phenolics, dyes, pesticides, insecticide, pharmaceuticals and other organic compounds have often found their way into the water system (Cosgrove & Loucks, 2015; Goel, 2006; Novotny, 1994; Sharma & Sanghi, 2012). Organic pollutants are known to be highly persistent in the environment with lifetimes ranging from days to several years (Jones & de Voogt, 1999). The stability of their molecular rings prevent natural decay processes (Graymore *et al*., 2001; Toze, 2006). Most organic chemical pollutants in water arise from surface run offs from agricultural fields and coloured wastewater from industries. Textile, leather, plastic, cosmetic and food industries often release soluble dyes which cause dramatic eutrophication and perturbation in the aquatic life (Vörösmarty *et al*., 2000). One such common dye is methylene blue, which is largely used in the textile industries. Despite conventional methods of water treatment being common, they are slow, non-destructive towards recalcitrant organic matter and are expensive when applied in large scale. Therefore, it is necessary to develop efficient materials for water treatment that can remove toxic pollutants from both the environment and water. Stringent environmental regulations and standards have been set driving development of these new technological systems (Sharma & Sanghi, 2012).

2.2. Hydrogen Energy - Future Fuel

Renewable energy can be derived from sources that are continually replenished by nature. These energy sources like photochemical, photoelectric and thermal energy originate directly from the sun while wind, biomass and hydropower originate indirectly from the sun (Liu *et al*., 2009; Şen, 2004). Others like geothermal arise from other natural mechanisms (Hossain, 2012; Rafiee & Khalilpour, 2019). However, they have some limitations which complicates their substitution. Geothermal and hydropower energy require huge capital investment and would pose possible environmental effects while putting up wind turbines require huge pieces of land. (Lewis & Nocera, 2006). Dependence of sunlight on the geographical location during the day and season makes it an irregular source of energy even though it's capable of meeting the world's annual consumption demand within just one hour of irradiation (Fyfe *et al*., 1993).

Transition to hydrogen fuel is considered an ideal alternative to fossil fuels (Hirscher, 2010; Teichmann *et al*., 2011; Winter & Nitsch, 2012). Hydrogen is an attractive chemical energy carrier

that is abundantly present in nature as it makes up nearly 75% by mass of the universe (Viswanath, 2004). It has potentially higher energy efficiency, high storage capability and low generation of pollutants (Balat, 2008; Bockris, 2002). The world has progressively favoured hydrogen atom over carbon atom (Winter & Nitsch, 2012). The process of decarbonisation has seen a silent transition from solid to liquid to gas fuels over the years. Each successive source has witnessed an increase in the ratio of hydrogen to carbon with coal currently having the lowest ratio at 0.5:1. Figure 2.2. shows the global energy system transition (Dunn, 2002).
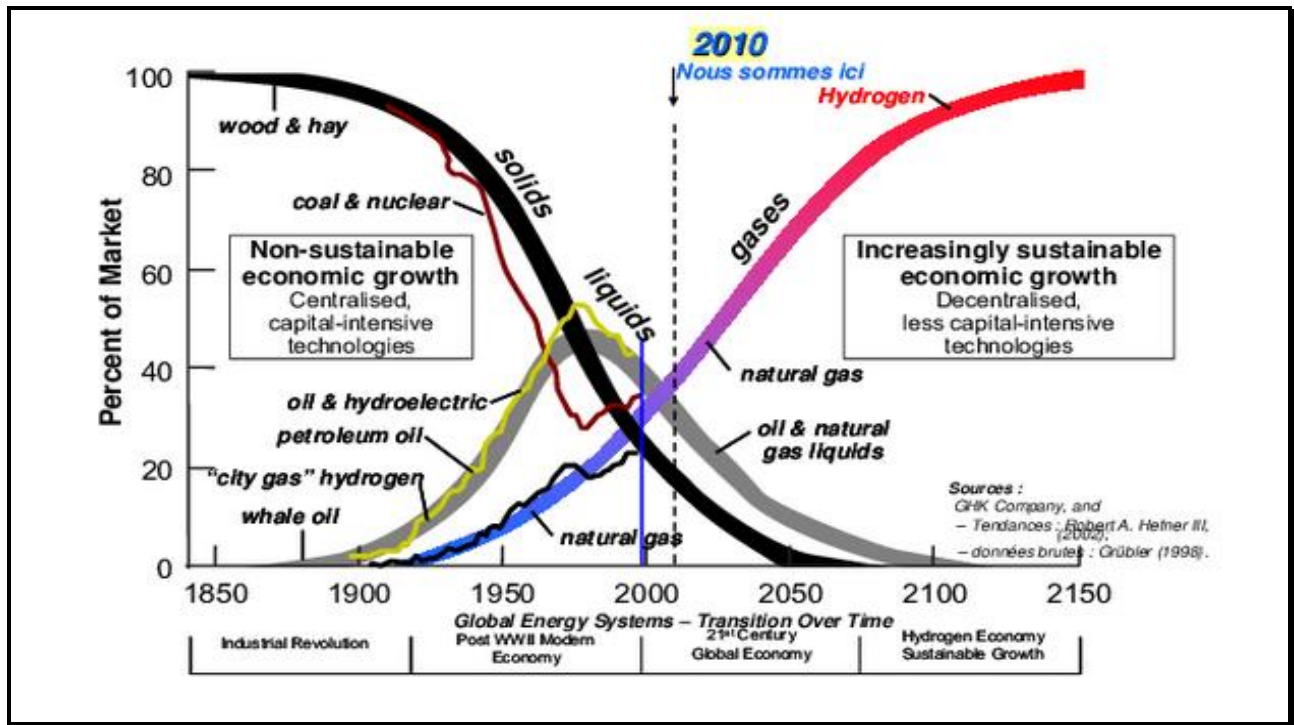
Figure 2.2. Global energy system transition (Dunn, 2002)

Table 2.1. summarizes the different routes that have been used in hydrogen production. Currently, natural gas reforming is the most ideal and cheapest technique used but it's an energy intensive process and also generates huge amounts of greenhouse gases (Balat, 2008; Dunn, 2002; Teichmann *et al.*, 2011). One of the green source of hydrogen is the photocatalytic splitting of water using solar energy in presence of a semiconductor photocatalyst. Chemical energy stored in the H–H bond in hydrogen is easily released on reaction with oxygen to produce only water thus a clean energy carrier (Hirscher, 2010; Winter & Nitsch, 2012).

Table 2.1. Different hydrogen production routes (Bockris, 2002; Dunn, 2002)

Hydrogen production route	Advantages	Disadvantages
Natural gas (methane) reforming	Less expensive (76% of world H_2 is produced this way) Most efficient	Generates greenhouse gases
Coal gasification	Compared to methane reforming, natural gas is expensive	Generates CO_2 Less efficient
Electrolysis	Effective for small quantity of pure hydrogen gas	Expensive in large scale
Renewable Liquid reforming (Gasoline and ethanol)	No information	Require pure oxygen Generates more CO_2
Fermentation (Biomass)	Less expensive raw materials used	Limited contribution (4%) to world H_2 production
Water splitting (High temperature, Photo-biological, **photo-electrochemical**)	Use renewable solar energy	In development stage

2.3. Titanium Dioxide as a Photocatalyst

Transition metal oxide systems like ZnO and TiO_2 have recently been the focus of appreciable research interest for both hydrogen generation and remediation of environmental pollutants under UV-visible absorption light (Dong *et al*., 2015; Elhage *et al*., 2019; Hainer *et al*., 2018; J. Kim *et al*., 2014; Tang *et al*., 2018). Both applications are based on the generation of an electron-hole (e-h) pair (exciton) upon photoexcitation and the subsequent transfer of photoinduced electrons to electron acceptors such as protons and pollutants through the metal oxide conduction band (CB) (Lanterna & Scaiano, 2017; Rahimi *et al*., 2015; Yadav *et al*., 2018). TiO_2, in particular, is widely distributed in terms of its commercially exploitable reserves and is considered the best metal oxide for these applications. This is because of its reduced cost, non-toxicity and favourable photocatalytic activity properties (Dong *et al*., 2015; Teh & Mohamed, 2011). Nanometric TiO_2

has widely been used for photocatalysis, in cosmetics, sensors, paints, and photovoltaics amongst other uses as heterogeneous photocatalyst and rate enhancing supports (Elhage *et al*., 2019).

TiO_2 is a semiconductor which predominantly absorbs light in the ultraviolet B (UVB) region. A significant disadvantage to its use is its low sensitivity to photons in the visible spectrum, which constitutes about 41% of solar energy reaching the earth surface (Schultz & Yoon, 2014). On the other hand, rapid e-h recombination severely hinders the practical efficiencies that can be derived from any mechanism aimed at harvesting electrons or holes (Elhage *et al*., 2019; Schneider & Bahnemann, 2013). With these shortcomings in mind, a lot of research has focused on developing photoactive systems that will not only absorb a wide spectrum of solar radiation but also prolong the life span of charge separated states (Rahimi *et al*., 2015; Tang *et al*., 2018).

In a bid to address these issues, different modification strategies have been used to develop TiO_2 photocatalysts. Most notably, doping of TiO_2 with narrow band gap materials or decoration with organic dyes, metal or metal oxide nanoparticles are common (Dong *et al*., 2015; Teh & Mohamed, 2011). Ruthenium and porphyrin dyes have exhibited the highest efficiencies in power conversion, especially with DSSCs (Altobello *et al*., 2004; Polo *et al*., 2004). However, the use of ruthenium complexes in practical applications has been limited since it is a rare and expensive element with an undesirable environmental impact leaving porphyrins as the most desirable alternative (Karthikeyan and Lee, 2013). Porphyrin-based chromophores have drawn considerable attention due to their nontoxicity, high molar absorption coefficients in the visible region as well as the ease of modification and tuning of the photophysical properties of synthetic porphyrins via their substituents (Duan *et al*., 2010; Huang *et al*., 2009). The photoinduced excitation of the dye prompts surface electron transfer between the dye and TiO_2 interface populating TiO_2 CB (Grätzel, 2003; Jafari et al., 2016; Meng et al., 2007).

2.4. Porphyrins
2.4.1. Introduction to Porphyrins

Porphyrin originated from the Greek word *porphura* which means violet (Fadda *et al*., 2013). This directly reflects on the common knowledge that porphyrins are coloured macrocyclic compounds that possess intense absorption in the visible spectrum. Porphyrins exist in nature.

Vitality of all living things revolve around porphyrins. For animals to live, it is basic to respire. Heme in haemoglobin is the chief agent of respiration and it is an iron metallated porphyrin (Figure 2.3.a). Plants on the other hand play an important role in the life cycle and are classified as homophytes. They make their own food by photosynthesis.
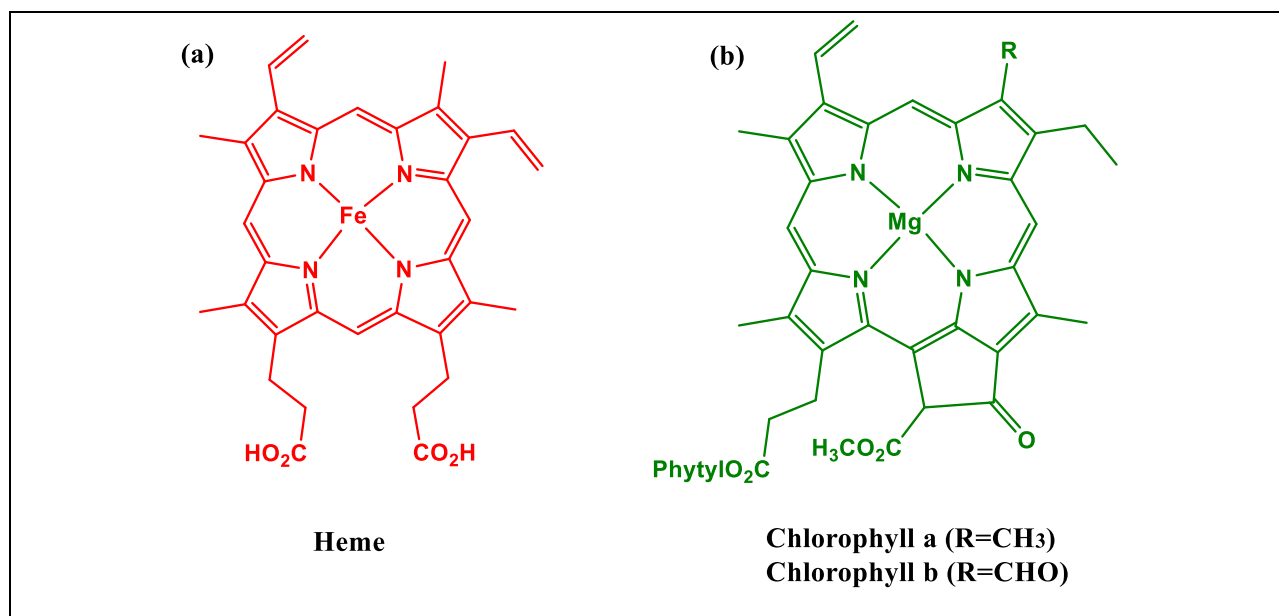
Figure 2.3. Natural porphyrins

Photosynthesis is a process that relies on a green pigment called chlorophyll to harvest solar energy from sunlight. Chlorophyll is a magnesium metallated porphyrin as seen in Figure 2.3.b. For these reasons, porphyrins have earned the tag "pigments of life" among natural compounds because of their role in the life cycle.

2.4.2. Structure of Porphyrins

Nencki in 1884 proposed that the porphyrin structure was based on pyrroles (Moore, 2009; With, 1980). Years later, Kuster specified that only four pyrrole units make up the macrocycle. In 1926, Fischer synthesized an etioporphyrin finally confirming the structure (Fischer & Klarer, 1926; Kadish *et al.*, 2012; Moore, 2009; With, 1980).

Structurally, the porphyrin macrocycle is made up of four pyrrole units joined together by methine bridges (Figure 2.4.a). According to Huckel's aromaticity rule (4n + 2), these compounds are

aromatic; with n = 4 since we have 18 π conjugated electrons. In total, there are 22 π electrons with only 18 being delocalized as presented in Figure 2.4.b (Kadish *et al*., 2012; Moore, 2009). Porphyrins stability and fascinating chemical, photophysical and spectroscopic qualities can be attributed to
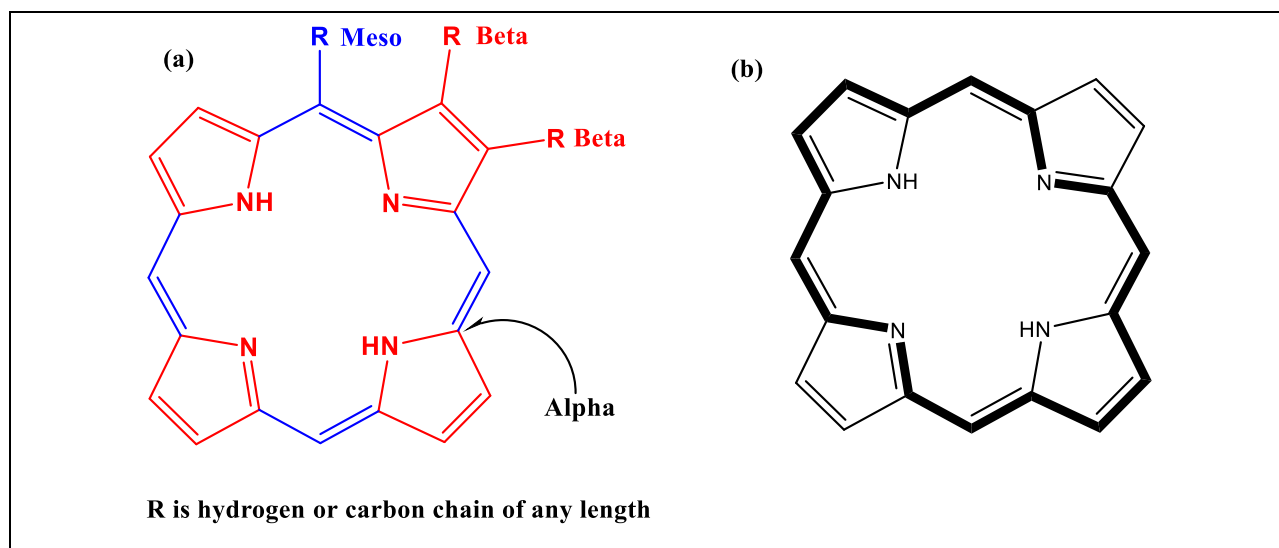
Figure 2.4. Structure of porphyrins

the strong conjugation. For these reasons, they have gained great attention to the science community especially for applications in biochemistry, biology, medicine and chemistry (Biesaga *et al*., 2000; Hu *et al*., 2011; D. Kim, 2012; Sessler & Burrell, 1992). Recently, porphyrins have attracted specific application in Photodynamic Therapy (PDT) studies, Photodynamic Antimicrobial Chemotherapy (PACT) and photosensitization of transition metals for applications in photocatalysis (Alves *et al*., 2015; Dong *et al*., 2015; Kadish *et al*., 2012; Pandey Ravindra *et al*., 2016).

Depending on the expected properties and applications, porphyrin macrocycle can be modified with different metal ions to form complexes. Also, porphyrins can be substituted at either *beta* or *meso* positions with substituents to further enhance their properties (Kadish *et al*., 2012; Moore, 2009; Sessler & Burrell, 1992). Figure 2.5 presents different porphyrin complexes that can be found in nature. These porphyrins possess different photophysical characteristics as their structures have one or more double bonds reduced.
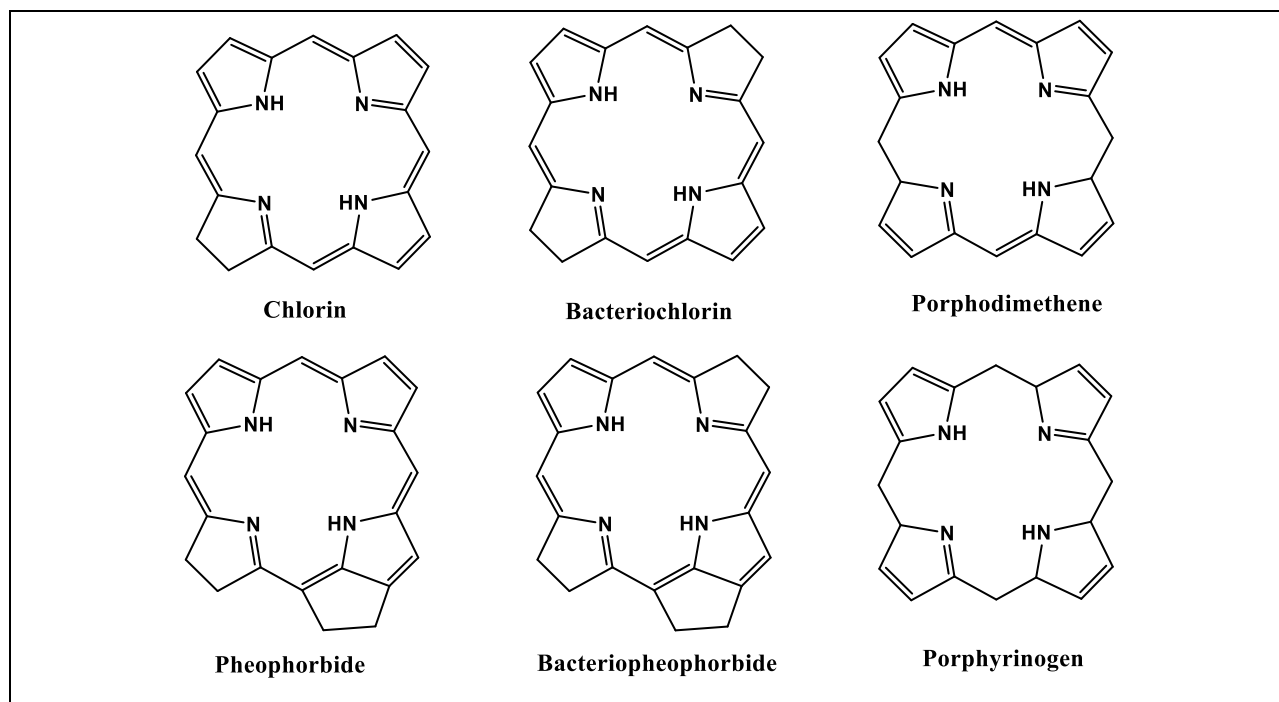
Figure 2.5. Porphyrinoid photosensitizers

2.4.3. Synthesis of Porphyrins

Rothemund in 1936 reported the first synthesis of a symmetrically substituted porphyrin (Rothemund, 1936). Basically, it was a condensation reaction between pyrroles and aldehydes at varied temperatures. A couple of years later, Rothemund was able to optimise the synthesis raising the yields to double digits (10%). The optimized conditions had pyrrole being condensed with benzaldehyde for 48 h in sealed tubes at 220 °C with pyridine as the solvent of choice.

Adler, Longo and his co-workers developed (Adler *et al.*, 1967) another method in 1967 by condensing pyrrole and an aldehyde under acidic conditions (propionic acid) as illustrated in Scheme 2.1.
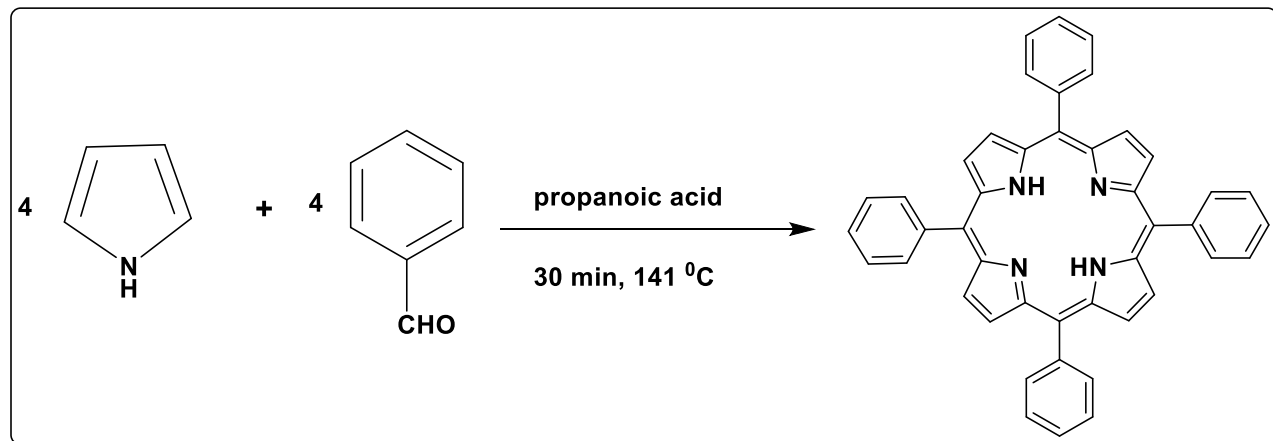
Scheme 2.1. Adler-Longo synthesis method

The most attractive feature of this method was the ability of the porphyrin product to crystallize out of the partially cooled solvent with improved yields ranging between 20 – 40%. However, both Ruthemund and Adler-Longo methods have a major drawback mainly due to the harsh reaction conditions limiting the use of a number of aldehydes with sensitive functional groups (Lindsey *et al.*, 1987). Also, this method was only suitable for symmetrical porphyrins. Accessing asymmetrical porphyrins with two or more distinct *meso* substituents frequently resulted in complex oligomers and low yield for porphyrins with very many permutations making it difficult to separate. This was the method of choice for the synthesis in this research.

The Lindsey method overcame the limitations presented by the Adler-Longo method (Lindsey, 1994; Lindsey *et al.*, 1987). This was a two-step synthesis under very mild conditions. Condensation of an aldehyde and pyrrole was carried out under inert atmosphere in DCM. In the first step, a Lewis acid such as Boron tri-fluoride diethyl etherate (BF$_3$.OEt$_2$) or trifluoroacetic acid (TFA) was used to catalyse the reaction into cyclization. There are competing reactions between the formation of porphyrinogen by cyclization and formation of polypyrromethane as illustrated in Scheme 2.2. The unstable porphyrinogen is then oxidised by adding 2,3-dichloro-5,6-dicyano-1,4-benzoquinone (DDQ) or tetrachloro-1,4-benzoquinone (p-chloranil) to aid oxidative dehydrogenation (6e$^-$/6H$^+$) for the second step.
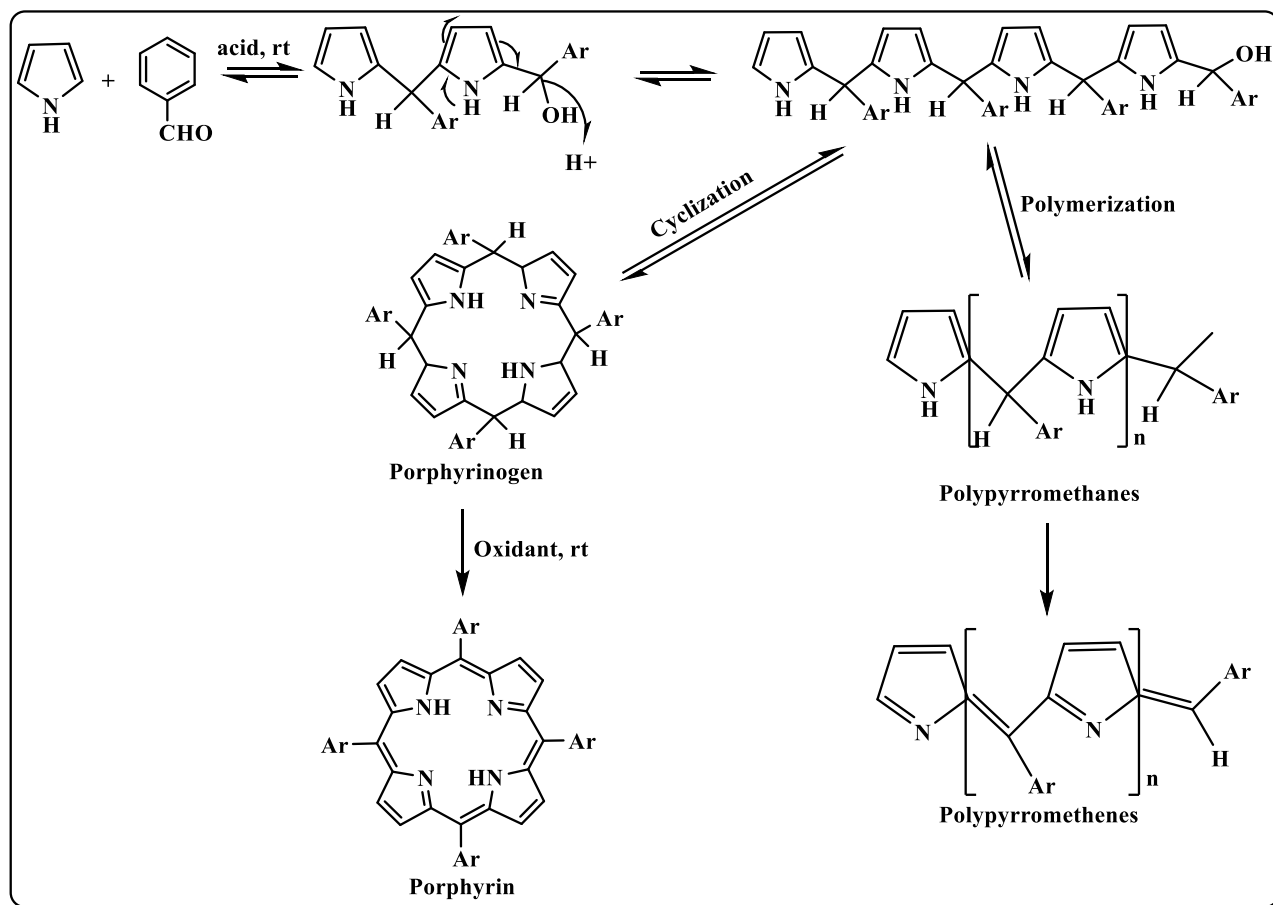
Scheme 2.2. Lindsey synthesis (Lindsey, 1994)

Apart from the generous yield of between 40 – 50% realized with Lindsey method, its other advantage is that it paved way for synthesis of statistical mixtures of porphyrins. The major drawback is the very low concentrations of reactants (less than 10^{-2} M) required to favour cyclization over polymerization.

2.4.4. Characterization of Porphyrins

UV-visible spectrum is one of the most fundamental and informative spectroscopic methods in porphyrin chemistry. These studies help determine if the synthesized compounds absorb in the visible region and therefore their suitability for sensitization. Porphyrins derive their color and intensity from their highly conjugated π electron system (Greco *et al*., 2014; Kadish *et al*., 2012; Kumar *et al*., 2005). The most conspicuous and fascinating feature about porphyrins is their

characteristic spectra of two distinct regions in the near UV and visible spectrum. Two π-π* transitions in the visible spectrum give rise to a strong absorption band at 380 - 450 nm called soret (B) band and weaker bands (Q bands) in the region 500 – 700 nm (Kadish *et al.*, 2012; Kim, 2012; Moore, 2009).

Gouterman's four-orbital model proposed in 1961 (Gouterman, 1961) can be used to rationalize trends in the electronic excitation spectra of porphyrins. The main trends in the optical and redox properties can be rationalized through a consideration of four frontier orbitals that are derived from the HOMO and LUMO of a $C_{18}H_{18}$ parent hydrocarbon perimeter. Michl introduced an **a**, **s**, **-a** and **-s** nomenclature for these orbitals depending on whether there is a nodal plane (**a** and **-a**) or large coefficients (**s** and **-s**) aligned with the *y*-axis (Michl, 1984). For example, the HOMO-1, HOMO, LUMO and LUMO+1 can be assigned as the **a**, **s**, **-a** and **-s** MOs, respectively. The MOs derived from the HOMO and LUMO of the $C_{18}H_{18}$ parent perimeter have M_L values of ± 4 and ± 5, respectively. Four spin allowed one-electron transitions are possible within the four orbital model. From quantum transition rules (selection rules), changes in angular momentum corresponding to $\Delta L = \pm 1$ or 0 represent allowed transitions while any other transition is forbidden. It is on this basis that Gouterman predicted the possibility of allowed B transition ($\Delta M_L = \pm 1$) at high energy and a forbidden Q transition ($\Delta M_L = \pm 9$) at lower energy, Figure 2.6 (Gouterman, 1961; Mack, 2017). Metalloporphyrins usually have D_{4h} symmetry and hence have two Q bands due to the main electronic transition and a vibrational overtone, since the **-a** and **-s** orbitals are degenerate (Gouterman, 1961). However, since free base porphyrins have D_{2h} symmetry, their **-a** and **-s** orbitals are nondegenerate, so there is a splitting of the two Q bands into *x*- and *y*-polarized components (Gouterman, 1961; Mack, 2017).
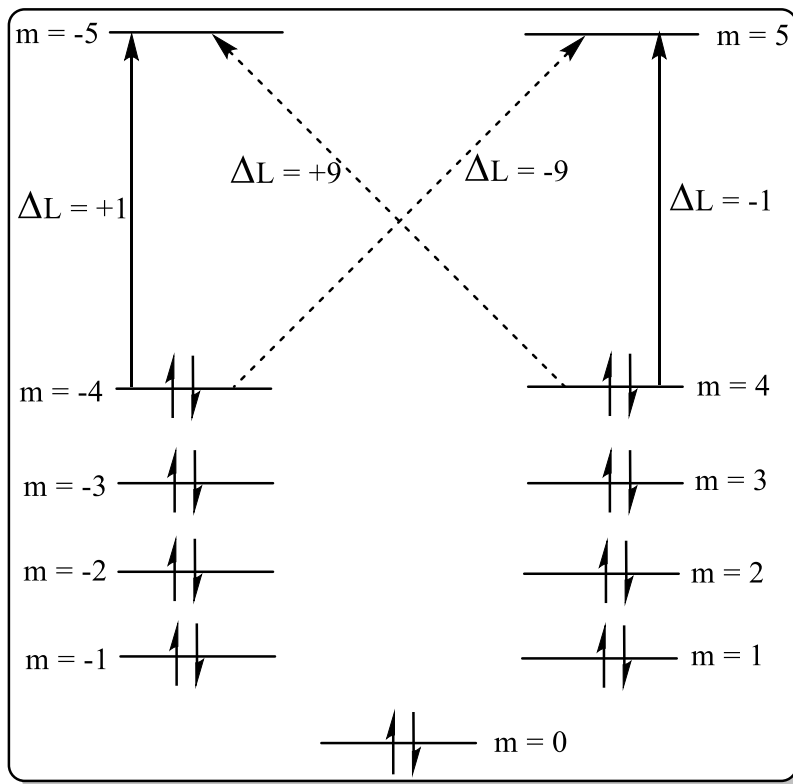
Figure 2.6. Electronic structure of a pophine adapted from an 18- membered cyclic polyene model. The allowed (block lines) and forbidden (broken lines) are shown (Kuhn, 1949; Simpson, 1949)

2.5. Porphyrins in Photodynamic Therapy (PDT) and Photodynamic Antimicrobial Chemotherapy (PACT)

2.5.1. Basic Principle

These concepts are based on an approach comprising the action of photosensitizing agent (PS), light source of appropriate wavelength and oxygen as presented in Figure 2.7. The electrons in the photosensi`tizing agent are first excited from singlet ground state to singlet excited state before undergoing intersystem crossing (ISC) to long lived excited triplet state. The electrons transfer their energy to molecular oxygen yielding aggressive chemical species that immediately react with neighbouring biomolecules as the PS relaxes to ground state (Alves *et al*., 2015; Cassidy *et al*., 2010; Ravindra *et al*., 2016).

Two oxidative mechanisms (Figure 2.7) of photo inactivation (PI) have been proposed in inactivation of target cells (Huang *et al*., 2012; Ravindra *et al*., 2016).

17

I. Triplet PS compound interacts with cell organic substrate molecule producing free radicals and radical ions. The radical compounds then react with endogenous oxygen and reactive oxygen species (ROS) like hydroxides and hydrogen peroxide radicals produced irreversibly damaging the cell membrane. The surrounding structures are preserved thus placement of PS should be as close to the infection as possible.

II. Associated with the transfer of energy from the triplet state molecular oxygen producing singlet state oxygen ($^1O_2$). This is a highly reactive species that on interaction with the biomolecules irreversibly alters the vital components of the cell leading to oxidative lethal damage.
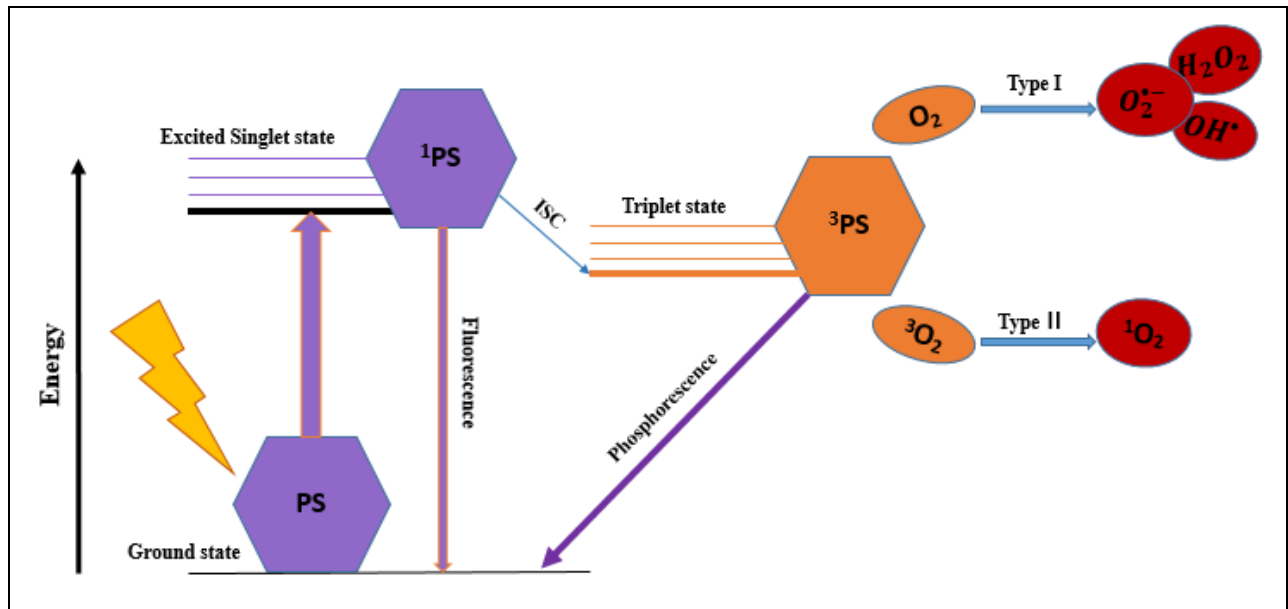
Figure 2.7. Mechanism of ROS generation by PDT (Hamblin & Jori, 2011)

2.5.2. Photodynamic Therapy (PDT) and Photodynamic Antimicrobial Chemotherapy (PACT)

PDT as a cancer therapy approach has employed a combination of visible sunlight, light sensitive drug (photosensitizer) and oxygen to generate toxic species that are able to destroy tumor cells (Kessel, 2004). PACT on the other hand emerged as a potent alternative in water treatment for its effective destruction of bacteria and micro-organisms with no viable recovery or resistance against it (Alves *et al*., 2015; Hamblin & Jori, 2011).

It has been established that photodynamic activities cause damage to the DNA and cytoplasmic membrane of the micro-organisms leaking out cellular content and permanently inactivating membrane transport systems and enzymes (Managa, *et al*., 2017b; Ravindra *et al*., 2016). The extensive damage made on diverse bacterial structure and cancerous cells by the ROS makes it impossible for development of resistance.

In PDT, the PS is administered intravenously or orally and allowed to accumulate in the tumor cells. The cells are then irradiated with light of desired wavelength generating toxic species. PDT has the advantage of non-target specificity and therefore very few side effects. Singlet state oxygen has a short half-life due to its very reactive nature thus its diffusion is limited to within the cell (Ravindra *et al*., 2016; Skovsen *et al*., 2005). Upon photo-activation, only the cells that accumulated the PS are killed ensuring minimal collateral damage.

PACT proved effective against multidrug resistant *Staphylococcus aureus* and other multiple resistant bacteria (Maisch, 2015). Efficiency of PACT in water disinfection has been proved by laboratory tests using faecal pollution indicators (Amos-Tautua *et al*., 2019; Jemli *et al*., 2002). Studies have also shown unlikelihood of excessive accumulation of PS in the environment since they gradually bleach at exposure to sunlight (Rotomskis *et al*., 1997).

2.6. Sensitization of Photocatalysts
2.6.1. Dye Sensitized photocatalysis in Degradation of Environmental Pollutants

Under solar irradiation, the process of dye sensitized photocatalytic degradation can be summarized by Equations (2.1) to (2.7) and illustrated by Figure 2.8 (Elsellami *et al*., 2010; Hancock-Chen and Scaiano, 2000; Sun *et al.*, 2011).

$$TiO_2[Dye] + h\nu \rightarrow TiO_2[Dye]^+ \tag{2.1}$$

$$TiO_2[Dye]^+ \rightarrow TiO_2\,(e^-_{CB})[Dye]^+ \rightarrow TiO_2[Dye]^+ + e^-_{CB} \tag{2.2}$$

$$TiO_2[Dye]^+ + H_2O \rightarrow OH^{\bullet} + H^+ \tag{2.3}$$

$$e^-_{CB} + O_2 \rightarrow O_2^{\bullet-} \tag{2.4}$$

$$O_2^{\bullet-} + H^+ \rightarrow HO_2^{\bullet} \tag{2.5}$$

$$HO_2^{\bullet} + HO_2^{\bullet} \rightarrow H_2O_2 \qquad (2.6)$$

$$H_2O_2 + O_2^{\bullet -} \rightarrow OH^- + OH^{\bullet} + O_2 \qquad (2.7)$$
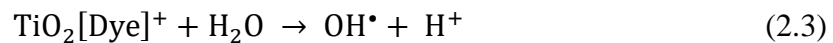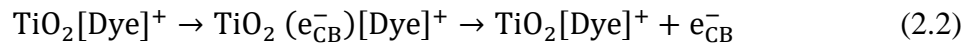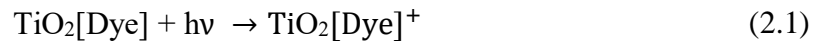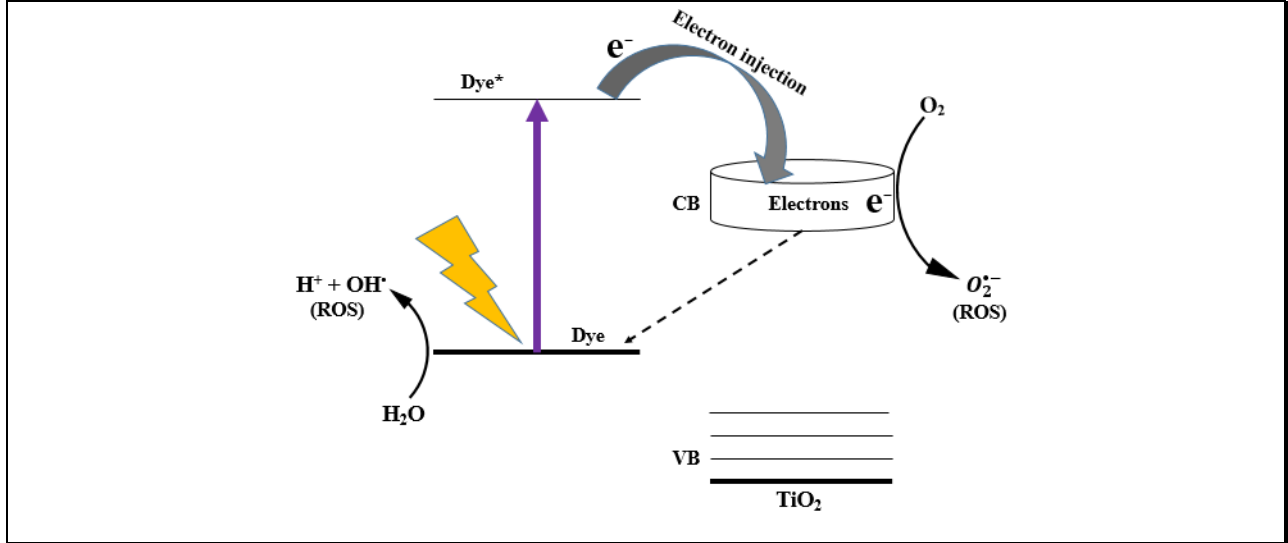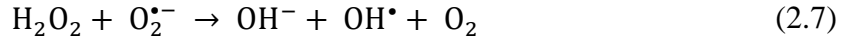
Figure 2.8. Photocatalytic path in degradation of pollutants (Chowdhury *et al.*, 2012)

Hydrogen peroxide, hydroxyl radicals and superoxide are all reactive species capable of reducing organic matter to their simplest forms of NH_3, water and carbon (iv) oxide. Hydrazine, phenols, chlorophenols, trichloroethylene and carbon tetrachloride are just but some of the compounds that have successfully been degraded by dye sensitized transition metals (Cho *et al.*, 2008; Chowdhury *et al.*, 2012; Muszkat *et al.*, 2002).

2.6.2. Dye Sensitized photocatalysis in Sacrificial Hydrogen Generation

Figure 2.9 illustrates the photocatalytic path in hydrogen generation from a dye sensitized semiconductor. The consecutive steps are explained in Equation (2.8) to (2.13) below:

i.   Absorption of light

$$Dye + h\nu \rightarrow Dye^* \qquad (2.8)$$

$$TiO_2 + h\nu \rightarrow h^+ + TiO_2\ (e_{CB}^-) \qquad (2.9)$$
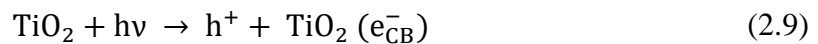
ii.   TiO₂ sensitization

$$Dye^* + TiO_2 \rightarrow Dye^+ + TiO_2 (e_{CB}^-) \qquad (2.10)$$

iii.   Water splitting

$$h^+ + H_2O \rightarrow OH^\bullet + H^+ \qquad (2.11)$$

iv.   Hydrogen generation

$$TiO_2(e_{CB}^-) + H^+ \rightarrow \frac{1}{2}H_2 \qquad (2.12)$$
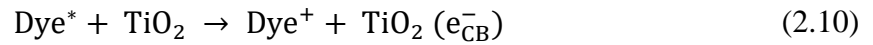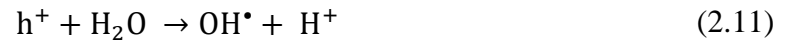
v.   Dye regeneration

$$Dye^+ + ED \rightarrow Dye + D + H^+ \qquad (2.13)$$
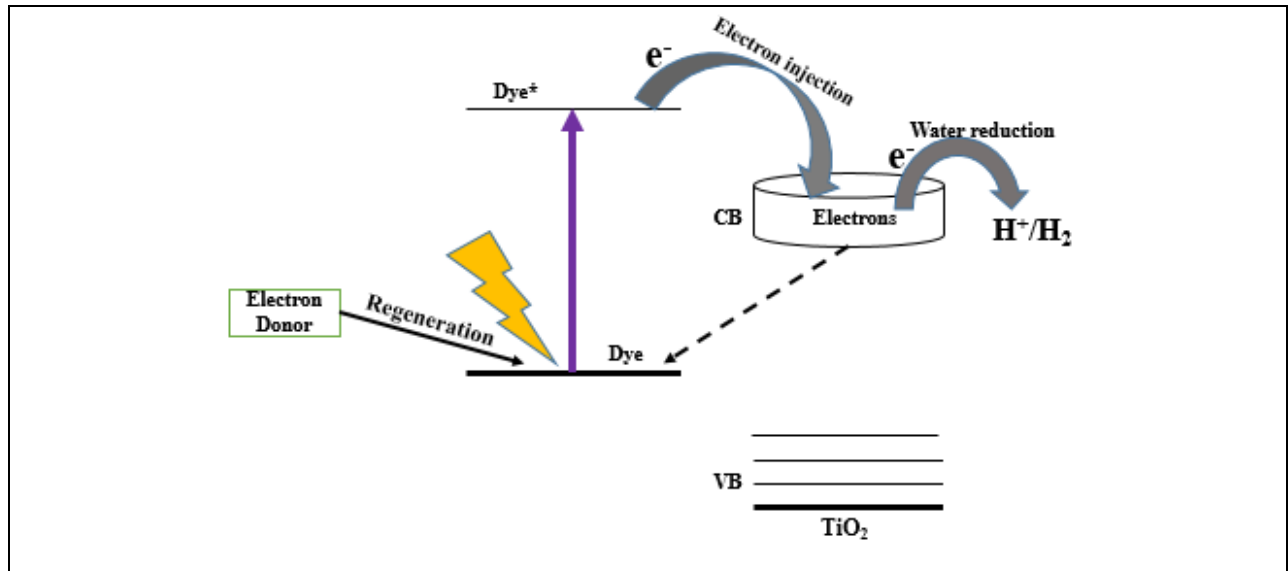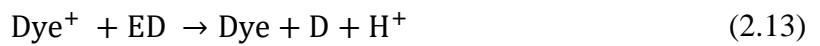
Figure 2.9. Photocatalytic path in hydrogen generation (Chen *et al.*, 2010)

CHAPTER THREE
MATERIALS AND METHODS

3.1. Materials

Pyrrole, 4-bromobenzaldehyde, dichloromethane (DCM), methanol (MeOH), high purity grade silica gel for column chromatography (60Å, 35-60 mesh particle size), thin layer chromatography (TLC) plates, sodium acetate, 5-bromo-2-thiophenecarboxaldehyde, methylene blue (MB), indium(III) chloride ($InCl_3$), tetraphenylporphyrin (H_2TPP), zinc tetraphenylporphyrin (ZnTPP) and gallium (III) chloride, were purchased from Sigma Aldrich. Hexane, propionic acid, sodium hydrogen carbonate, acetic acid and zinc acetate were purchased from Loba Chemie PVT Ltd. Toluene and ethyl acetate were purchased from Fisher Scientific. Distilled water was obtained from an ultrapure filtration system (Millipore, resistivity 18 mΩ cm^{-1}). Degussa P25 TiO_2 nanopowder was purchased from Univar Canada.

3.2. Instrumentation

The ground state electronic absorption spectra were obtained at room temperature from an Agilent Technologies Cary 60 UV-Vis spectrophotometer in 1.0×1.0 cm quartz cuvettes while corrected emission spectra were obtained with a PTI Quanta Master spectro-fluorometer with 0.4×1.0 cm cuvette. Fluorescence lifetime data were recorded on a time-correlated EasyLife X filter fluorescence lifetime fluorimeter. The IR spectra were recorded on a Nicolet 6700 FT-IR spectrometer, and centrifugation was carried out on an Eppendorf centrifuge 5804 R. The instrument response function (IRF) was obtained at the wavelength of excitation (395 nm) using Ludox as the scatterer. Mass spectrometry data were recorded from a Bruker Auto FLEX III Smartbeam MALDI-TOF instrument, and dithranol was used in positive ion mode as the matrix. The elemental analyses were measured on a Vario EL III Microcube CHNS Analyzer. NMR spectra were obtained from a Bruker AVANCE II 400 MHz NMR spectrometer with $CDCl_3$ as the reference standard. The morphologies of TiO_2, and their porphyrin complexes were observed using a JSM-7500FFE SEM Scanning electron microscopy (SEM) operated at 100 kV. Diffuse reflectance spectroscopy (DR) data were collected on a VARIAN Cary 100 UV-Vis spectrophotometer coupled to an integrating sphere accessory. Samples were irradiated using a

Luzchem SolSim CCP providing simulated solar radiation approximately matching in intensity the 1.5 A.M solar spectrum. The hydrogen generated was detected and quantified with a Perkin Elmer, Clarus 480 GC-TCD using Argon as carrier gas and a 5A zeolite molecular sieve column.

3.3. Synthesis of Porphyrins

The aromatic *meso*-substituted porphyrins PP1 and PP2 were synthesized by a single step acid catalyzed condensation reaction of pyrrole with an appropriate aldehyde based on the Adler-Longo method. Their metal complexes were synthesized according to literature methods (Hong *et al*., 1996; Managa *et al*., 2017a). Scheme 3.1 gives a summary of the synthetic pathway used and the reaction conditions.
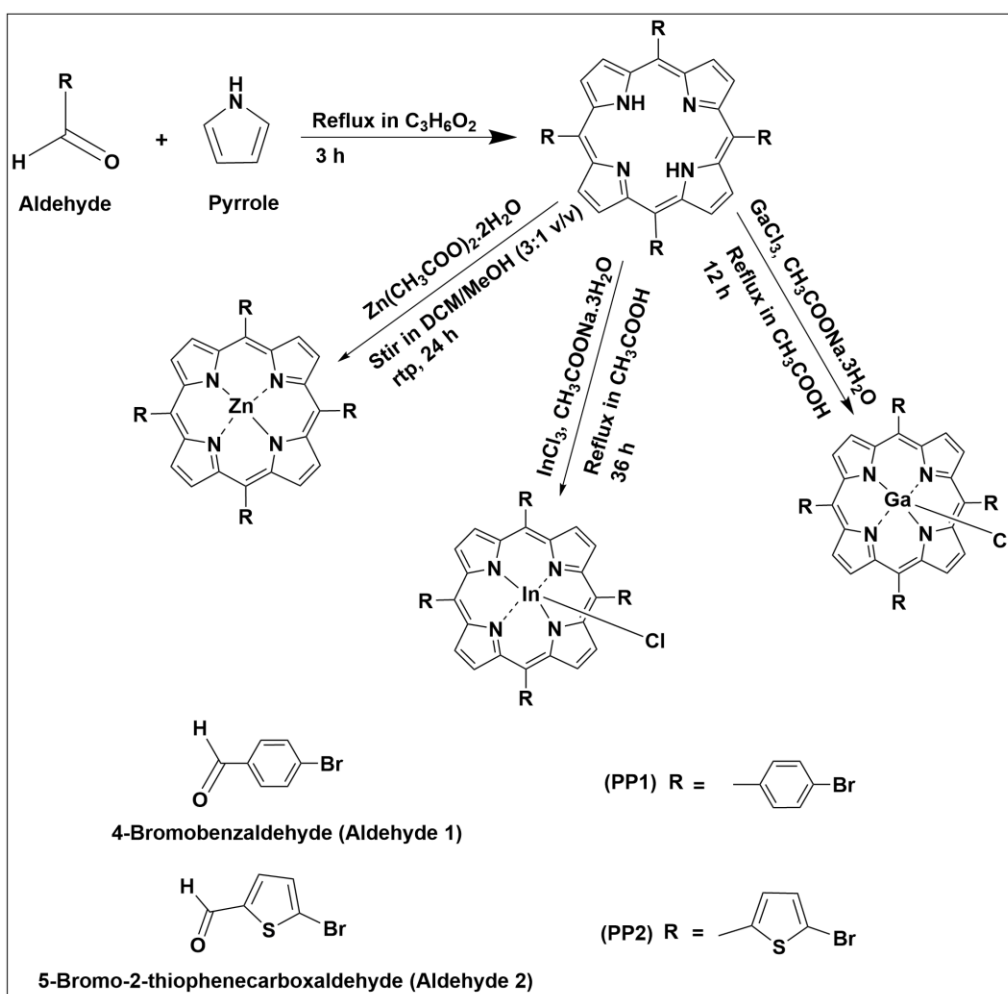
Scheme 3.1. Synthetic pathway for PP1, PP2 and their metal complexes

3.3.1. Synthesis of meso-tetra (4-bromophenyl) porphyrin (PP1)

Freshly distilled pyrrole (1.20 mL, 18 mmol) was added dropwise to a warm solution of 4-bromobenzaldehyde (3.24 g, 18 mmol) in propionic acid (80 mL). The mixture was brought to reflux temperature (125 − 130 °C) with stirring for 3 h. The progress of the reaction was continually monitored by TLC and UV-visible absorption spectroscopy. The reaction vessel was allowed to cool to room temperature and 50 mL methanol was added to further quench the solution and aid crystallization. The product was collected as a purple solid by vacuum filtration, washed with methanol and left to dry in open air. The product was further purified by elution in a column of silica gel with ethyl acetate: hexane (1:9 v/v) mobile phase.

Yield: Purple solid (2.01 g, 12%). UV/Vis (Toluene) λ_{max} nm (ε (L Mol^{-1} cm^{-1})): 421 (2.1×10^5), 517 (9.4×10^3), 550 (4.5×10^3), 593 (2.7×10^3) and 650 (2.1×10^3). ^{1}H NMR (400 MHz, CDCl$_3$) δ 8.84 (*s*, 8H, β Pyrrol), 8.06 (*d, J*= 8.3Hz, 8H), 7.90 (*d, J*= 8.3Hz, 8H). IR ν_{max} cm^{-1} 3320 (N−H), 3000 (=C−H$_{str}$), 1370 (C−N$_{str}$). Calc. for C$_{44}$H$_{26}$Br$_4$N$_4$: C = 56.81, H = 3.03, N = 6.01; found C = 56.54, H = 3.00, N = 6.10. MALDI-TOF-LRMS *m/z*: calcd = 930.34, found = 930.94 [M$^+$].

3.3.2. Synthesis of meso-tetra (5-bromo-2-thiophenyl) porphyrin (PP2)

PP2 was prepared in the same manner as PP1. Freshly distilled pyrrole (1.04 mL, 15 mmol) and 5-bromo-2-thiophenecarboxaldehyde (1.78 mL, 15 mmol) were refluxed for 30 min.

Yield: Purple solid (1.43 g, 10%). UV/Vis (Toluene) λ_{max} nm (ε (L Mol^{-1} cm^{-1})): 431 (2.6×10^5), 524 (13.5×10^3), 561 (7.0×10^3), 600 (4.5×10^3), 665 (3.7×10^3). ^{1}H NMR (400 MHz, CDCl$_3$) δ 9.11 (s, 8H, β Pyrrol), 7.66 (*d, J*= 3.6Hz, 4H), 7.49 (*d, J*= 6.35Hz, 4H). IR ν_{max} cm^{-1} 3310 (N−H), 3100 (=C−Hstr), 1250 (C−Nstr). Calc. for C$_{36}$H$_{18}$Br$_4$N$_4$ S$_4$: C = 45.30, H = 1.90, N = 5.87, S = 13.44; found C = 45.67, H = 1.80, N = 5.61, S = 13.46. MALDI-TOF-LRMS *m/z*: calcd = 954.42, found = 954.78 [M$^+$].

3.3.3. Synthesis of ClIn, ClGa and Zn metal complexes of PP1 and PP2

The indium and gallium metalloporphyrins were synthesized as follows: To warm acetic acid (50 mL), sodium acetate, free base porphyrin (PP1 or PP2) and either gallium or indium chloride was added and the solution brought to reflux temperature (115 − 119 °C). With stirring, either of the solutions were refluxed for 15 h and 36 h for gallium and indium respectively. The progress of the reaction was monitored by TLC and UV-visible absorption spectroscopy. Acetic acid was removed in *vacuo* and sodium hydrogen carbonate was added to neutralize the remaining acid. The product was dissolved in DCM and washed three times in a separatory funnel with distilled water. The product was retrieved from DCM under vacuum and further purified by column chromatography.

Reagents used for GaPP1 were; PP1 (0.60 g, 0.645 mmol), gallium chloride (0.36 g, 2.096 mmol) and sodium acetate (0.44 g, 3.225 mmol). The product was purified over silica gel column using methanol: dichloromethane (2:8 v/v) mobile phase.

Yield: Purple solid (0.43 g, 65%). UV/Vis (Toluene) λ_{max} nm (ε (L Mol^{-1} cm^{-1})): 424 (6.9×10^5), 553 (29×10^3), 592 (6.2×10^3). ^{1}H NMR (400 MHz, CDCl$_3$) δ 8.82 - 9.06 (m, 8H, β Pyrrol), 8.04 (*d, J*= 8.3Hz, 8H), 7.89 (*d, J*= 8.5Hz, 8H). IR ν_{max} cm^{-1} 2900 (=C−H$_{str}$), 1250 (C−N$_{str}$). Calc. for C$_{44}$H$_{24}$Br$_4$ClGaN$_4$: C = 51.14, H = 2.34, N = 5.42; found C = 51.64, H = 2.39, N = 5.33. MALDI-TOF-LRMS *m/z*: calcd = 1033.49, found = 997.97 [M−Cl]$^+$.

Reagents used for GaPP2 were; PP2 (0.40 g, 0.419 mmol), gallium chloride (0.23 g, 1.341 mmol) and sodium acetate (0.29 g, 2.096 mmol). The product was purified over silica gel column using methanol: dichloromethane (2:8 v/v) mobile phase.

Yield: Purple solid (0.27 g, 61%). UV/Vis (Toluene) λ_{max} nm (ε (L Mol^{-1} cm^{-1})): 434 (3.9×10^5), 561 (22.7×10^3), 604 (4.7×10^3). ^{1}H NMR (400 MHz, CDCl$_3$) δ 9.35 (s, 8H, β Pyrrol), 7.68 (*d, J*= 3.7Hz, 4H), 7.48 (*d, J*= 7.2Hz, 4H). IR ν_{max} cm^{-1} 2900 (=C−Hstr), 1380 (C−Nstr). Calc. for C$_{36}$H$_{16}$Br$_4$ClGaN$_4$S$_4$: C = 40.89, H = 1.52, N = 5.30, S = 12.13; found C = 40.72, H = 1.58, N = 5.32, S = 12.02. MALDI-TOF-LRMS *m/z*: calcd = 1057.58, found = 1022.77 [M−Cl]$^+$.

Reagents used for InPP1 were; PP1 (0.60 g, 0.645 mmol), indium chloride (0.29 g, 1.230 mmol) and sodium acetate (0.44 g, 3.225 mmol). The product was purified over silica gel column using ethyl acetate: hexane (1:9 v/v) solvent system.

Yield: Purple solid (0.38 g, 55%). UV/Vis (Toluene) λ_{max} nm (ε (L Mol^{-1} cm^{-1})): 430 (5.4 $\times$ 10^5), 563 (31 $\times$ 10^3), 602 (13.2 $\times$ 10^3). ^{1}H NMR (400 MHz, CDCl$_3$) δ 9.02 (s, 8H, β Pyrrol), 8.23 (d, J=8.5Hz, 4H), 7.88 – 7.89 (m, 12H,). IR ν_{max} cm^{-1} 2900 (=C$-$H$_{str}$), 1250 (C$-$N$_{str}$). Calc. for C$_{44}$H$_{24}$Br$_4$ClInN$_4$: C = 49.00, H = 2.24, N = 5.19; found C = 48.36, H = 2.38, N = 5.47. MALDI-TOF-LRMS m/z: calcd = 1078.59, found = 1043.38 [M$-$Cl]$^+$.

Reagents used for InPP2 were; PP2 (0.40 g, 0.419 mmol), indium chloride (0.19 g, 0.838 mmol) and sodium acetate (0.29 g, 2.096 mmol). The product was purified over silica gel column using ethyl acetate: hexane (1:9 v/v) solvent system.

Yield: Purple solid (0.23 g, 49%). UV/Vis (Toluene) λ_{max} nm (ε (L Mol^{-1} cm^{-1})): 439 (3.0 $\times$ 10^5), 570 (15.7 $\times$ 10^3), 613 (6.6 $\times$ 10^3). ^{1}H NMR (400 MHz, CDCl$_3$) δ 9.33 (s, 8H, β Pyrrol), 7.70 (d, J= 4.6 Hz, 4H), 7.50 (d, J= 6.7 Hz, 4H). IR ν_{max} cm^{-1} 2900 (=C$-$Hstr), 1250 (C$-$Nstr). Calc. for C$_{36}$H$_{16}$Br$_4$ClInN$_4$S$_4$: C = 39.21, H = 1.46, N = 5.08, S = 11.63; found C = 39.50, H = 1.38, N = 5.11, S = 12.01. MALDI-TOF-LRMS m/z: calcd = 1102.68, found = 1067.79 [M$-$Cl]$^+$.

Zinc metalloporphyrins were synthesized as follows: To a solution of free base porphyrin (PP1 or PP2) a saturated solution of zinc acetate in methanol was added and the mixture was stirred at RT for 12 h. The solvent was removed in *vacuo* and the product was purified.

Reagents used for ZnPP1 were; PP1 (0.30 g, 0.323 mmol), zinc acetate (0.24 g, 1.093 mmol), methanol (15 mL) and DCM (45 mL). The product was purified over silica gel column using ethyl acetate: hexane (1:9 v/v) mobile phase.

Yield: Purple solid (0.27 g, 83%). UV/Vis (Toluene) λ_{max} nm (ε (L Mol^{-1} cm^{-1})): 425 (9.6 $\times$ 10^5), 550 (52.8 $\times$ 10^3), 589 (10.6 $\times$ 10^3). ^{1}H NMR (400 MHz, CDCl$_3$) δ 8.94 (s, 8H, β Pyrrol), 8.07 (d, J= 8.4Hz, 8H), 7.90 (d, J= 8.4Hz, 8H). IR ν_{max} cm^{-1} 2900 (=C$-$H$_{str}$), 1270 (C$-$N$_{str}$). Calc. for C$_{44}$H$_{24}$Br$_4$ZnN$_4$: C = 53.18, H 2.43, N 5.64; found C = 53.55, H 2.75, N 5.52.

Reagents used for ZnPP2 were; PP2 (0.25 g, 0.262 mmol), zinc acetate (0.17 g, 0.786 mmol), methanol (15 mL) and DCM (45 mL). The product was purified over silica gel column using ethyl acetate: hexane (1:9 v/v) solvent system.

Yield: Purple solid (0.21 g, 78%). UV/Vis (Toluene) λ_{max} nm (ε (L Mol^{-1} cm^{-1})): 433 (8.0×10^5), 559 (51.9×10^3), 602 (8.5×10^3). ^{1}H NMR (400 MHz, CDCl$_3$) δ 9.19 (s, 8H, β Pyrrol), 7.63 (*d, J*= 6.2Hz, 4H), 7.46 (*d, J*= 3.6Hz, 4H). IR ν_{max} cm^{-1} 2900 (=C−Hstr), 1250 (C−Nstr). Calc. for C$_{36}$H$_{16}$Br$_4$ZnN$_4$S$_4$: C = 42.48, H = 1.58, N = 5.50, S = 12.60; found C = 42.37, H 1.61, N 5.43, S 12.52.

3.4. Steady state Fluorescence Spectroscopy

As illustrated in Equation (3.1), comparative methods were used to determine fluorescence quantum yields (Φ_F) (Φ_F) and Tetraphenylporphyrin (H$_2$TPP) in toluene was used a standard ($\Phi_F^{Std} = 0.11$) for the free bases while Zinc Tetraphenylporphyrin (ZnTPP) in toluene as a standard ($\Phi_F^{Std} = 0.033$) for the metallated porphyrins (Hu *et al.*, 2011).

$$\Phi_F = \frac{F \; A^{Std} \; n^2}{F^{Std} A \; (n^{Std})^2} \; \Phi_F^{Std} \tag{3.1}$$

In the equation, A and A^{Std} are the optical densities for the sample and standard solutions respectively, while, F and F^{Std} are the integrated areas under the emission curves for sample and standard, n and n^{Std} are the refractive indices of the solvents (Fery-Forgues & Lavabre, 1999). The radiative (k_r) and non-radiative (k_{nr}) rate constant data were obtained by calculation according to Equation (3.1) to (3.4) (Maiti & Ravikanth, 1996).

$$\Sigma \, k = \frac{1}{\tau F} \tag{3.2}$$

$$k_r = \Phi_F \times \Sigma \, k \tag{3.3}$$

$$k_{nr} = \Sigma \, k - k_r \tag{3.4}$$

3.5. Fluorescence Lifetimes

Fluorescence lifetime (τ_F) values were determined using a time correlated EasyLife X filter fluorescence lifetime fluorimeter. Time resolved fluorescence decay curves were analyzed by deconvoluting the observed decay with the IRF to obtain the intensity decay function. Reduced chi squared values were evaluated and considered to determine the best fit for experimental data.

3.6. Theoretical Calculations

Quantum calculations were performed using the Gaussian 09 program (Frisch *et al*., 2015) and the theoretical model of choice was density functional theory (DFT). DFT is useful in providing direct information on electronic structure and strikes a favorable balance between computational cost and accuracy (Lundqvist *et al.*, 2006). The gas phase geometries of the porphyrin monomer structures were optimized by Becke's 3-parameter Lee Yang Parr (B3LYP) exchange-correlation functional (Becke, 1993; Lee *et al*., 1988). Linear time-dependent DFT (TD−DFT) calculations were performed with the Coulomb Attenuating Method B3LYP (CAM−B3LYP) functional. Mixed basis sets were used for these calculations; 6-31G(d,p) and Stuttgart-Dresden (SDD), the latter being preferred for porphyrin monomers with In(III) or Ga(III) metal ions. For TD−DFT calculations, solvation effect was included. Simulation in the solvent environment were performed by employing PCM (polarizable continuum model) using self-consistent reaction field (SCRF) on the already optimized Single Point (SP) geometries of the monomers.

3.7. Supporting Synthesized Porphyrins on TiO_2 Degussa P25

The deposition of porphyrins on the surface of TiO_2 was conducted. Porphyrins (10mg) were dissolved in DCM (8 mL) in eight separate vessels and to each of the solutions, TiO_2 (0.4 g) was added and sealed. The resulting suspension was sonicated for 30 min, then stirred magnetically at ambient temperature for 12 h. The photocatalyst was collected by centrifugation after washing three times with DCM and left to dry at 60 °C for 12 h. This procedure was according to the work of Duan and his co-workers (Duan *et al*., 2010).

3.8. Photocatalytic Degradation of Methylene Blue

The efficiency of the photocatalysts were investigated by monitoring the degradation of MB under simulated sunlight (SolSim). In a pyrex conical flask, 20 mL of the MB solution (5.023×10^{-3} mM) and 0.004 g of the photocatalyst was irradiated (Figure 3.1). Before irradiation, the solution was allowed to equilibrate in darkness for 2 h. The experiment was performed at ambient temperature with no pH adjustments, and a magnetic stirrer homogenized the solution throughout the experiment. Aliquots (3 mL) of the solution were collected at an interval of 10 min and filtered through with a Millipore Millex® syringe filter (0.45 µm) to get rid of the catalyst before analysis. UV-visible absorption spectroscopy was used to monitor the MB degradation through measurements at 664 nm (the longest wavelength band for MB). The concentrations of MB were deduced from a calibration curve obtained in the range $1.59 - 5.02 \times 10^{-3}$ mM, with Abs (a.u.) = 115260[L mol^{-1} cm^{-1}] – 0.0031, R=0.997. The experiments were carried out in triplicate.

Figure 3.1. Photocatalytic degradation of Methylene blue setup

3.9. Photocatalytic Hydrogen Generation activity

Photocatalytic production of hydrogen studies was carried out in a 10 mL glass vial sealed with crimp seals and rubber septa. In each experiment, 10 mg of the photocatalyst and 4 mL aqueous

solution of methanol (1%) was added to the glass vial. The system was degassed under argon gas for 30 min and sealed in the vacuum degassing chamber. The catalyst suspension was dispersed for 5 min in an ultrasonic bath then irradiated from the top for 4 h under solar simulator while magnetically stirring the system. Headspace gas (4 mL) was sampled from each vial by a sample lock syringe through the septum and immediately injected in the GC−TCD. The H_2 signal was detected at ~ 4.0 min. A calibration curve of the H_2 gas detected in the GC−TCD instrument was used in quantification. The experiments were carried out in triplicate.

CHAPTER FOUR
RESULTS AND DISCUSSION

In this study, the photocatalytic efficiency of a series of different metal porphyrin complexes and the corresponding free base porphyrins after adsorption on TiO_2 were investigated. *Meso*-tetra(4-bromophenyl)porphyrin (PP1) and *meso*-tetra(5-bromo-2-thienyl)porphyrin (PP2) and their In(III), Zn(II) and Ga(III) metal complexes were synthesized and characterized. In order to understand the intrinsic optical properties of the porphyrins where electron injection into the TiO_2 conduction band (CB) is concerned, theoretical calculations were carried out using DFT methods. The porphyrins were adsorbed on nanometric TiO_2 to yield porphyrin-TiO_2 (P–TiO_2) nanocomposites. The photocatalytic activities of the P–TiO_2 nanocomposites and Degussa P25 (TiO_2) were investigated via methylene blue (MB) degradation and hydrogen generation under irradiation by a solar simulator (AM 1.5).

4.1. Synthesis and Characterization of PP1, PP2 and their metal complexes

Free base porphyrins namely 5,10,15,20-tetra(4-bromophenyl)porphyrin (PP1) and 5,10,15,20-tetra(5-bromothiophen-2-yl)porphyrin (PP2) and their gallium (GaPP1, GaPP2), indium (InPP1, InPP2) and zinc (ZnPP1, ZnPP2) metal complexes were synthesised. In the following sections the synthesis and characterization of these compounds is discussed.

4.1.1. Synthesis and Characterization of 5,10,15,20-tetra(4-bromophenyl)porphyrin (PP1)

5,10,15,20-Tetra(4-bromophenyl)porphyrin (PP1) was synthesized by reaction of pyrrole with 4-bromobenzaldehyde using the Adler-Longo method (Adler *et al.*, 1967) as shown in Scheme 4.1.

The UV-visible spectrum of PP1 showed an intense B band centred at 421nm and four less intense Q bands (517, 550, 593 and 650 nm) which is a characteristic UV-Vis spectra for porphyrins (Gouterman, 1961; Nemykin & Hadt, 2010), Figure 4.1. The MALDI-TOF MS spectra of this compound gave a molecular ion peak at *m/z* value of 930.94 against a calculated *m/z* value of 930.34 for $C_{44}H_{26}Br_4N_4$ consistent with the molecular formula of the synthesized compound, Appendix A1. The elemental analysis results for this compound gave C 56.54, H 3.00, N 6.10 against a calculated value of C 56.81, H 3.03, N 6.01. Elemental analysis of the results to determine

the ratio of elements in the sample satisfied the assigned chemical formula $C_{44}H_{26}Br_4N_4$ of the target compound. These results were consistent with those obtained in a similar synthesis by Shi and his co-workers (Shi *et al.*, 2019).
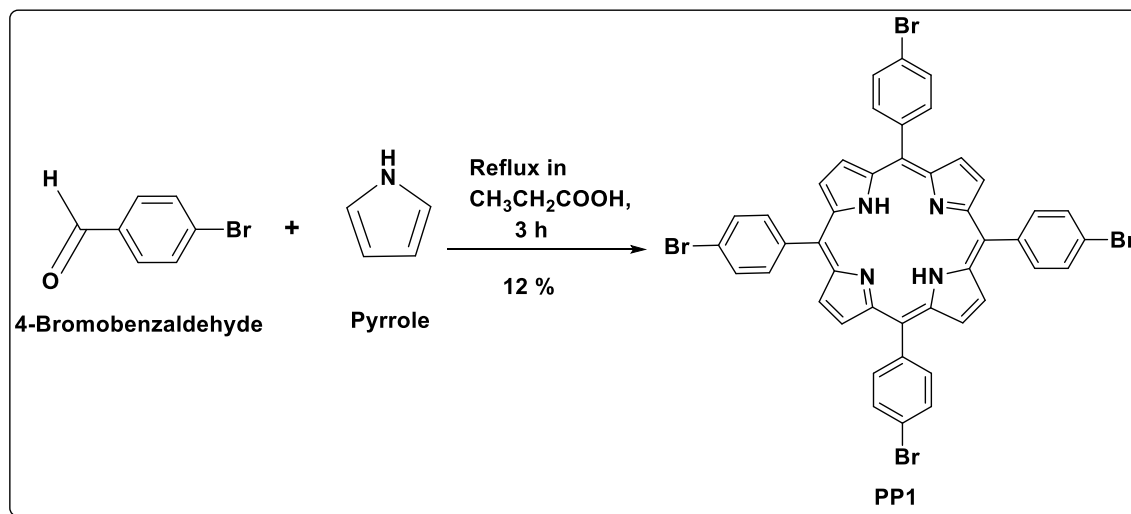
Scheme 4.1. Synthesis of 5,10,15,20-Tetra(4-bromophenyl)porphyrin

The ^1H NMR for this compound is also consistent with the structure of the target molecule, Appendix A2. The NMR showed a singlet at δ_H 8.84 integrating for eight protons and is assigned for the β-protons of the four pyrrole rings. These protons at the β position lie outside the macrocyclic ring current thus experience a deshielding effect increasing the chemical shift to higher values (Huang *et al.*, 2000; Marsh *et al.*, 1999). The NMR further showed signals for an AA'BB' spin system centred at δ_H 8.07 and 7.90 (*d*, *J* = 8.3 Hz) integrating for sixteen protons representing the four *beta* substituted aromatic rings (Jiménez *et al.*, 2002).

The FTIR of PP1 in Figure 4.3, showed signals at 3300 cm^{-1} for N–H str vibrations and are assigned to the pyrrole N–H bond (Fuhrhop *et al.*, 1992; Sen *et al.*, 2010). Bands of weak to median intensities appeared in the region 3100 – 2800 cm^{-1} and were assigned to C–H stretching modes (Wei *et al.*, 2006). The vibrations at 1370 cm^{-1} were assigned to C–N str vibrations (Fuhrhop *et al.*, 1992; Sen *et al.*, 2010; Wei *et al.*, 2006). All these data confirmed that indeed PP1 was synthesized.

4.1.2. Chloro 5,10,15,20-tetra(4-bromophenyl)porphinato galium (III) (GaPP1)

Chloro 5,10,15,20-tetra(4-bromophenyl)porphinato galium (III) (GaPP1) was synthesized by refluxing gallium chloride with PP1 in acetic acid as shown in Scheme 4.2 (Managa, *et al*., 2017b).
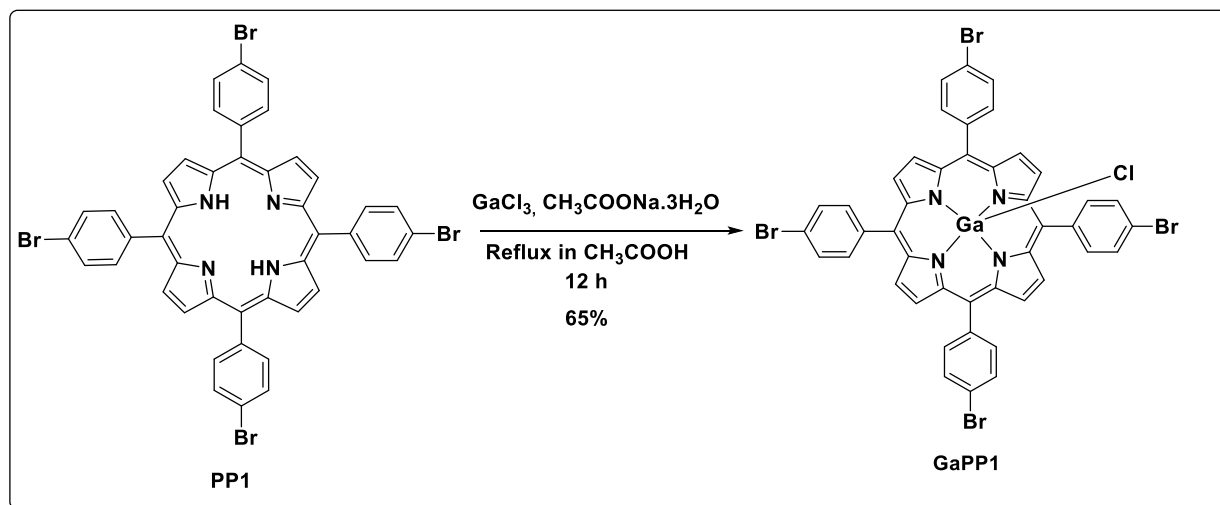
Scheme 4.2. Synthesis of Chloro 5,10,15,20-tetra(4-bromophenyl)porphinato galium (III)

The UV-visible spectrum of GaPP1, showed an intense band at 424 nm and two weaker bands at 553 and 592 nm which is a characteristic UV-Vis feature of metalloporphyrins (Huang *et al*., 2000; Kadish *et al*., 2012), Figure 4.1. The MS analysis for the axially ligated porphyrin showed a peak for $[M–Cl]^+$ at *m/z* 997.97 which corresponds to $C_{44}H_{24}Br_4GaN_4$, Appendix B1. The ion corresponds to the loss of axially ligated Cl group, a result that was also initially observed by Crossley and his workmates in the context of $(OH)_2Sn(IV)$ porphyrins (Crossley *et al*., 2001). Elemental analysis results found C 51.64, H 2.39, N 5.33 against calculated values of C 51.14, H 2.34, N 5.42 further confirming the synthesis of the title compound.

The ^{1}H NMR shows a peak at δ_H 8.82 – 9.06integrating for eight protons for the β-protons of the pyrrole ring and an AA'BB' spin system at δ_H 8.04 (*d, J*= 8.3Hz) and 7.89 (*d, J* = 8.5 Hz) integrating for sixteen protons for the *para* substituted aromatic rings, Appendix B2. Generally, metalation induces slightly downfield shift compared to the freebase PP1, with greater effect seen on the tetra pyrrole protons than the ones on the phenyl (Huang *et al*., 2000; Jiménez *et al*., 2002; Marsh *et al*., 1999).

The IR spectrum for GaPP1 was similar to the spectrum of PP1 apart from the notable absence of N–H str vibrations at 3300 cm^{-1} (Figure 4.3). This was an expected result due to nitrogen deprotonation during metal insertion. This therefore confirms the metal gallium was successfully inserted into the porphyrin core.

4.1.3. Chloro 5,10,15,20-tetra(4-bromophenyl)porphinato indium (III) (InPP1)

Chloro 5,10,15,20-tetra(4-bromophenyl)porphinato indium (III) (InPP1) was synthesized by refluxing indium chloride with PP1 in acetic acid as shown in Scheme 4.3 (Saenz *et al*., 2011; Soy *et al*., 2019).
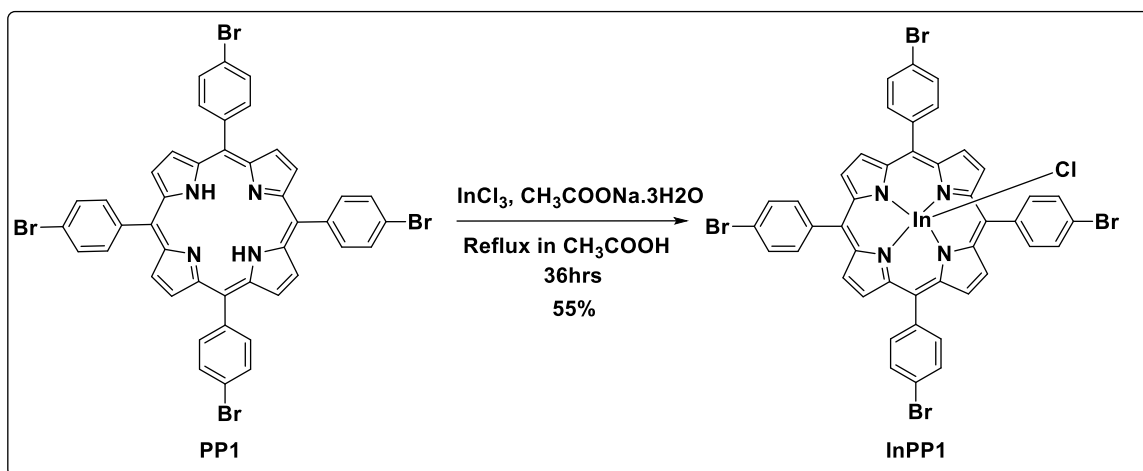
Scheme 4.3. Synthesis of Chloro 5,10,15,20-tetra(4-bromophenyl)porphinato indium (III)

An intense absorption band appearing at 430 nm and two weaker bands observed at 563 and 602 nm in the UV-Vis spectrum are consistent with a metalloporphyrin (Figure 4.1), (Gouterman, 1961; Kadish *et al*., 2012). The MS spectra for InPP1 provided a molecular ion peak [M– Cl]$^+$ at 1043.38 whereas the value calculated for $C_{44}H_{24}Br_4ClInN_4$ was 1078.59 indicating loss of the axial ligand Cl, Appendix C1. Elemental analysis found C 48.36, H 2.38, N 5.47 against calculated values of C 49, H 2.24, N 5.19. ^{1}H NMR (Appendix C2) showed a singlet at δ_H 9.02 (for β-protons) and further signals seen at δ_H 8.23 (*d*, 4H) and 7.88 – 7.89 (*m*, 12H,) for phenyl protons. As was in the case of GaPP1, the FTIR spectrum of InPP1 did not show any N–H str vibrations due to deprotonation confirming successful metalation (Figure 4.3). All the other absorption peaks observed for PP1 were present.

4.1.4. Zinc 5,10,15,20-tetra(4-bromophenyl)porphyrin (ZnPP1)

Zinc 5,10,15,20-tetra(4-bromophenyl)porphyrin (ZnPP1) was synthesized by a reaction of PP1 and zinc acetate at room temperature as shown in Scheme 4.4 (Karthikeyan & Lee, 2013).
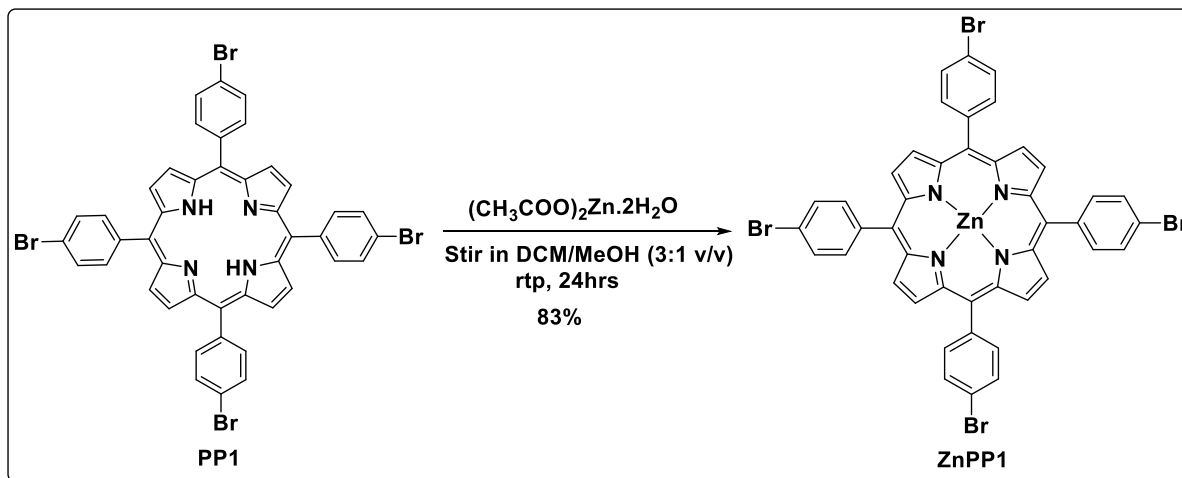
Scheme 4.4. Synthesis of Zinc 5,10,15,20-tetra(4-bromophenyl)porphyrin

The absorption spectrum of ZnPP1 showed soret band peak at 425 nm and two Q bands at 550 and 589 nm (Figure 4.1). Elemental analysis further confirmed the target compound when it recorded C 53.55, H 2.75, N 5.52 against calculated values of C 53.18, H 2.43, N 5.64. Just like the other compounds, tetra pyrrole β hydrogen appeared as a singlet on the ^{1}H NMR spectrum at δ_H 8.94 and tetra phenyl signals seen at δ_H 8.07 and 7.90 (d, J = 8.4 Hz), Appendix D1. The FTIR spectrum obtained for ZnPP1 confirmed successful metalation by the absence of the N–H str absorption bands (Figure 4.3).

4.1.5. Synthesis and Characterization of 5,10,15,20-Tetra(5-bromothiophen-2-yl)porphyrin (PP2)

5,10,15,20-Tetra(5-bromothiophen-2-yl)porphyrin (PP2) was synthesized by reaction of pyrrole with 5-bromo-2-thiophenecarboxaldehyde using Adler-Longo method (Adler *et al*., 1967; Greco *et al*., 2014; Kumar *et al*., 2019) as shown in Scheme 4.5.
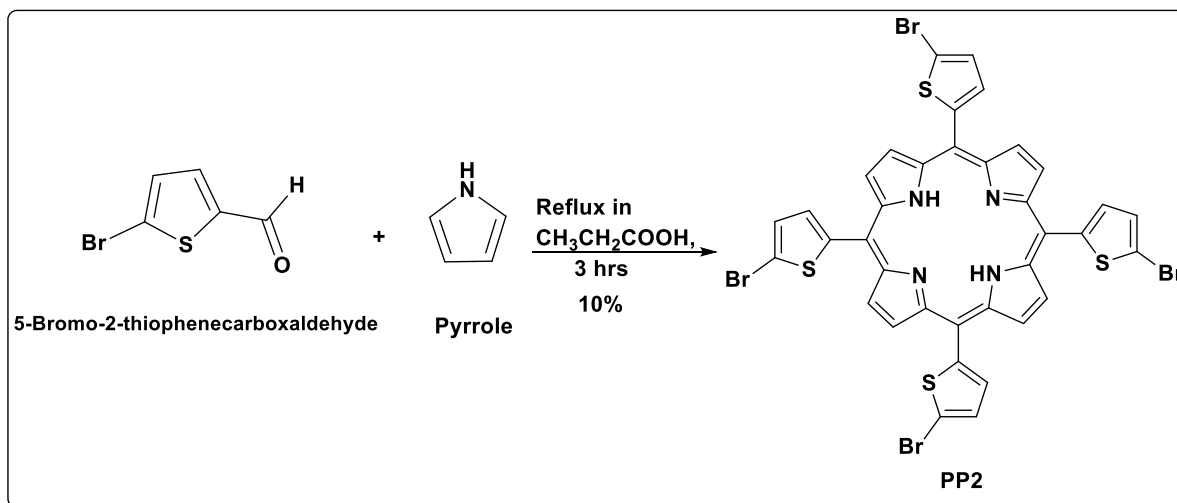
Scheme 4.5. Synthesis of 5,10,15,20-tetra(5-bromothiophen-2-yl)porphyrin

The UV-visible spectrum of PP2 was characterized by an intense B band centred at 431nm and four less intense Q bands (524, 561, 600 and 665 nm), Figure 4.2. Mass spectroscopic analysis provided an *m/z* value of 954.78 against a calculated *m/z* value of 954.42 followed by a degree of fragmentation Appendix E1. The difference between the peaks are 80 corresponding to loss of the Br group at the thienyl substituent. Elemental analysis results found C 45.67, H 1.80, N 5.61, S 13.46 against a calculated value of C 45.3, H 1.90, N 5.87, S 13.44. Analysis of the elemental results determined the ratio of elements in the sample satisfied the assigned chemical formula $C_{36}H_{16}Br_4S_4N_4$ of the target compound. The ^{1}H NMR showed a singlet at δ_H 9.11 integrating for eight protons and is assigned for the β-protons of the four pyrrole rings, Appendix E2. Just like in PP1, these protons at the β position in PP2 lie outside the macrocyclic ring current. However, thienyl ring improves resonance with the porphyrin core yielding greater ring current. These β-protons therefore, will experience greater deshielding effect compared to those in PP1 thus appear downfield shifted (Huang *et al.*, 2000; Marsh *et al.*, 1999) . Further, the signals for the thienyl group appear at δ_H 7.66 and 7.49 (*d*, *J* = 3.6, 6.4 Hz) integrating for eight protons. FTIR spectra recorded for PP2 in Figure 4.3 showed N–H str vibrations at 3310 cm^{-1}. As was the case in PP1, bands of weak to median intensities appeared in the region 3100 – 2800 cm^{-1} and were assigned to C–H str modes. C–N str vibrations of the porphyrin macrocycle gave a series of weak absorption peaks at the 1250 cm^{-1} region (Fuhrhop *et al.*, 1992; Sen *et al.*, 2010). Elghamry *et al.* (2018) achieved similar results.

4.1.6. Chloro 5,10,15,20-tetra(5-bromothiophen-2-yl)porphinato indium (InPP2)

Chloro 5,10,15,20-tetra(5-bromothiophen-2-yl)porphinato indium (InPP2) was synthesized using the same procedure used for InPP1 but PP2 was used instead of PP1 as illustrated in Scheme 4.6.
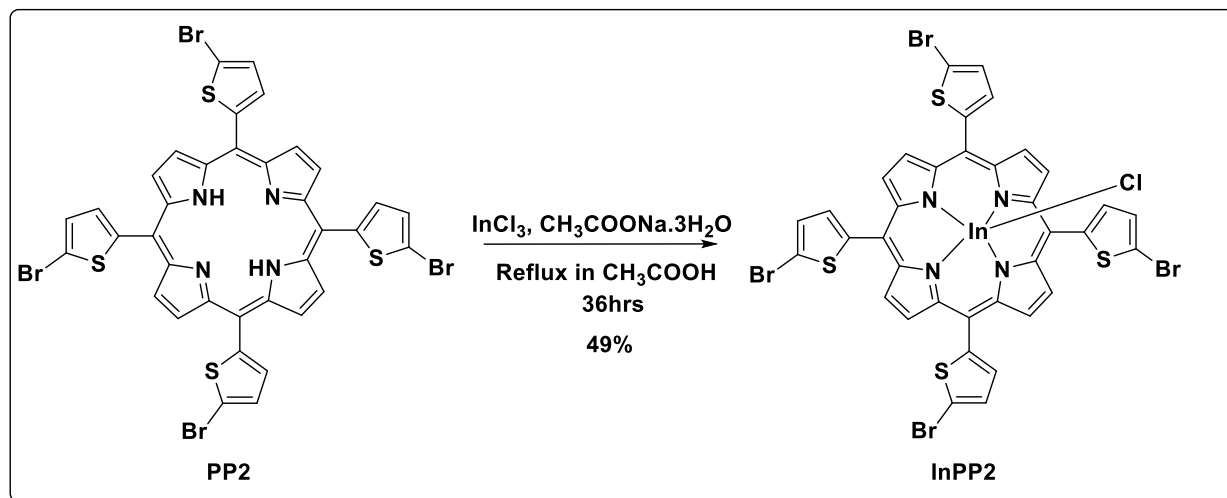
Scheme 4.6. Synthesis of Chloro 5,10,15,20-tetra(5-bromothiophen-2-yl)porphinato indium

UV-visible spectrum showed a characteristic intense band at 439 nm and two less intense bands at 570 and 613 nm (Figure 4.2). Just like the other axially ligated porphyrins, MS analysis of InPP2 provided a molecular ion $[M–Cl]^+$ at m/z 1067.79 against a calculated value of 1102.68 for $C_{36}H_{16}Br_4ClGaN_4S_4$. Fragmentation peaks with a difference of 80 corresponding to loss of Br group were seen like in PP2, Appendix F1. Similarly, like in the other compounds, elemental analysis ratio from experimental values of C 39.50, H 1.38, N 5.11, S 12.01 satisfied the assigned chemical formula. The ^{1}H NMR gave a singlet at δ_H 9.33 integrating for eight protons for the β-protons of the pyrrole ring, Appendix F2. Just like in PP2, these protons experience a higher deshielding effect hence appear at higher values than their PP1 metalloporphyrin counterparts. Thienyl group signals appear at δ_H 7.70 and 7.50 (*d*, *J* = 4.6, 6.7 Hz). Again, as was stated previously for the other metallated compounds, metalation induced a slight downfield shift compared to the freebase PP2. The FTIR spectrum recorded for InPP2 confirmed successful metalation by the absence of the N–H str vibrations seen in PP2 (Figure 4.3). All the other vibration modes observed for PP2 were present.

4.1.7. Chloro 5,10,15,20-tetra(5-bromothiophen-2-yl)porphinato gallium (GaPP2)

Like in GaPP1, chloro 5,10,15,20-tetra(5-bromothiophen-2-yl)porphinato gallium (GaPP2) was synthesized using a similar procedure with PP2 used instead of PP1 as illustrated in Scheme 4.7.
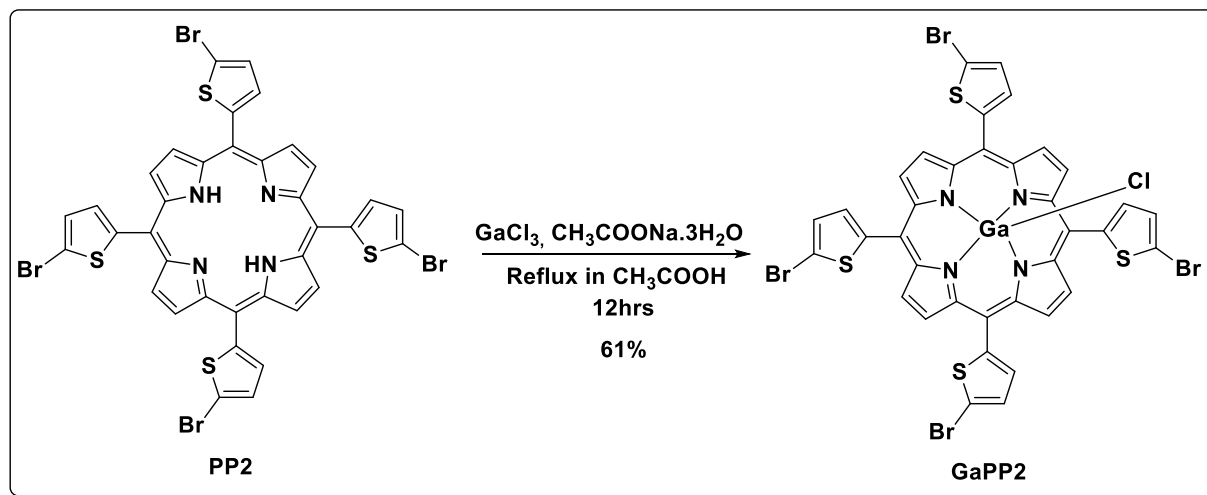
Scheme 4.7. Synthesis of Chloro 5,10,15,20-tetra(5-bromothiophen-2-yl)porphinato gallium

An intense absorption band was observed at 434 nm together with weak Q bands at 561 and 604 nm (Figure 4.2). Analysis of the MS data provided a molecular ion [M–Cl]$^+$ at m/z 1022.77 whereas the calculated value of $C_{36}H_{16}Br_4ClGaN_4S_4$ found 1057.58, Appendix G1. Similar fragmentation pattern in PP2 corresponding to loss of Br group was also seen in GaPP2. Elemental analysis further confirmed the target compound as it found C 40.72, H 1.58, N 5.32, S 12.02 against a calculated value of C 40.89, H 1.52, N 5.30, S 12.13. Similar to InPP2 ^{1}H NMR, β-protons of the pyrrole ring gave a singlet at δ_H 9.35 and signals of the thienyl group at δ_H 7.68 and 7.48 (*d, J* = 3.7, 7.2 Hz), Appendix G2. The FTIR spectrum for GaPP2 confirmed successful metalation by the absence of N–H str vibrations seen in PP2 (Figure 4.3).

4.1.8. Zinc 5,10,15,20-tetra(5-bromothiophen-2-yl)porphyrin (ZnPP2)

Zinc 5,10,15,20-tetra(5-bromothiophen-2-yl)porphyrin (ZnPP2) was synthesized by a reaction of PP2 and zinc acetate at room temperature as illustrated Scheme 4.8.
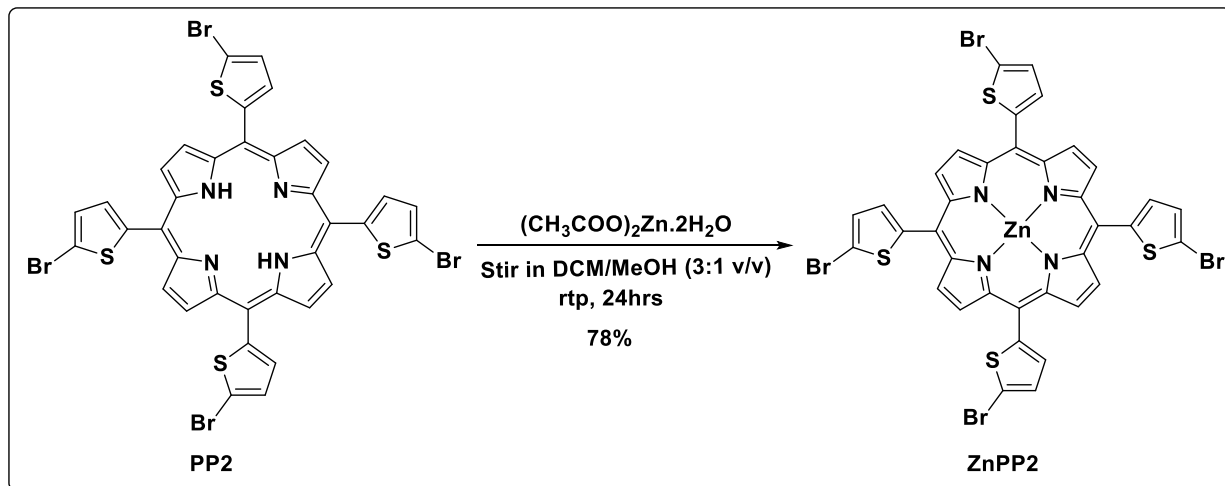
Scheme 4.8. Synthesis of Zinc 5,10,15,20-tetra(5-bromothiophen-2-yl)porphyrin

ZnPP2 showed a UV-visible spectrum with a B band at 433 nm and two Q bands at 559 and 602 nm (Figure 4.2). Elemental analysis further confirmed the target compound as it found C 42.37, H 1.61, N 5.43, S 12.52 against calculated values of C 42.48, H 1.58, N 5.50, S 12.60. Like in the other PP2 complexes, tetra pyrrole β protons appeared as a singlet further downfield on the ^{1}H NMR spectrum at δ_H 9.19 and the tetra thienyl group signal at δ_H 7.63 and 7.46 (*d, J* = 6.2, 3.6 Hz), Appendix H1. ZnPP2 also exhibited an FTIR spectrum seen in Figure 4.3 that matched the one seen for PP2. However, due to deprotonation by insertion of Zn metal at the porphyrin core, the N–H str vibration was absent.
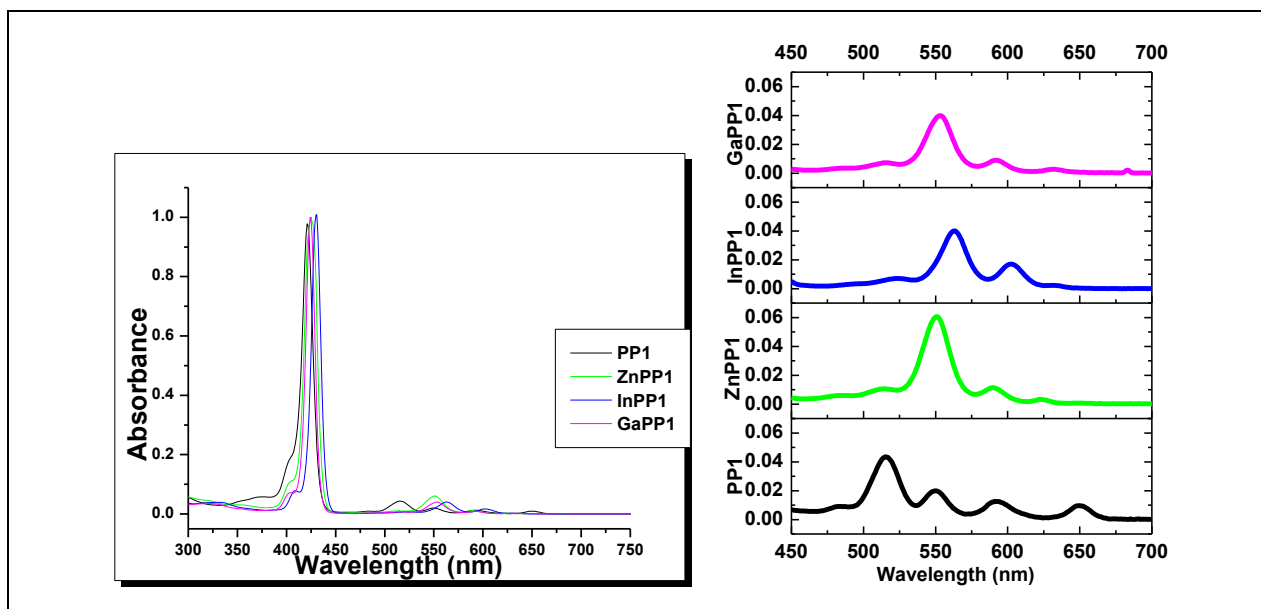
Figure 4.1. Normalized absorption spectra of PP1 and their metal complexes in toluene
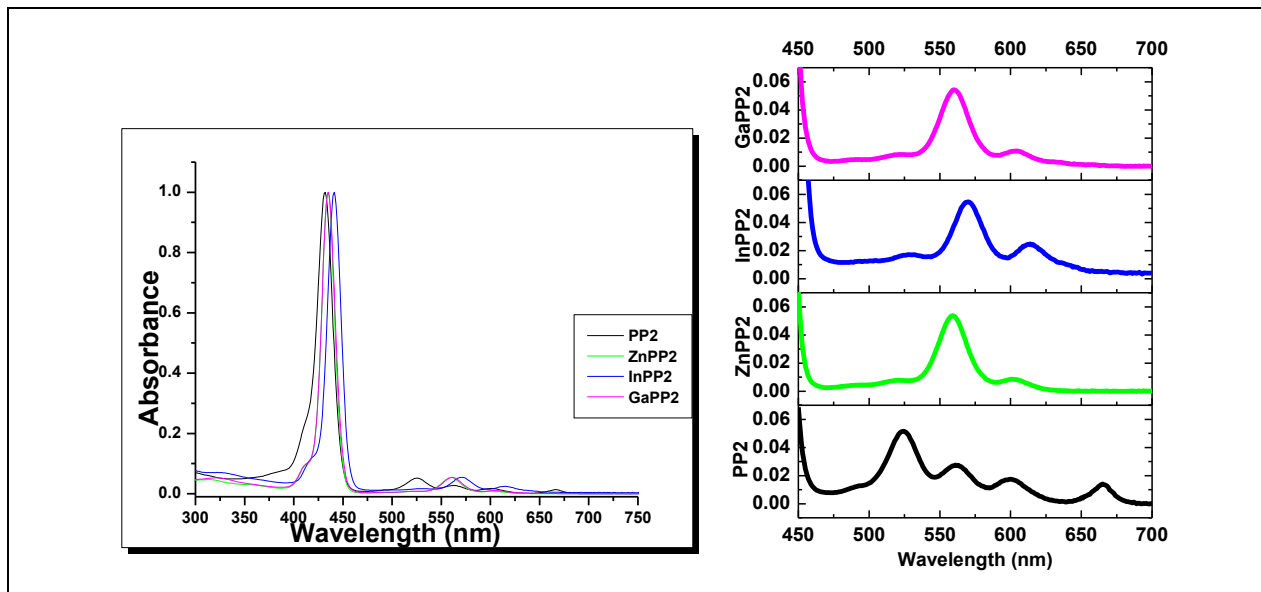
Figure 4.2. Normalized absorption spectra of PP2 and their metal complexes in toluene
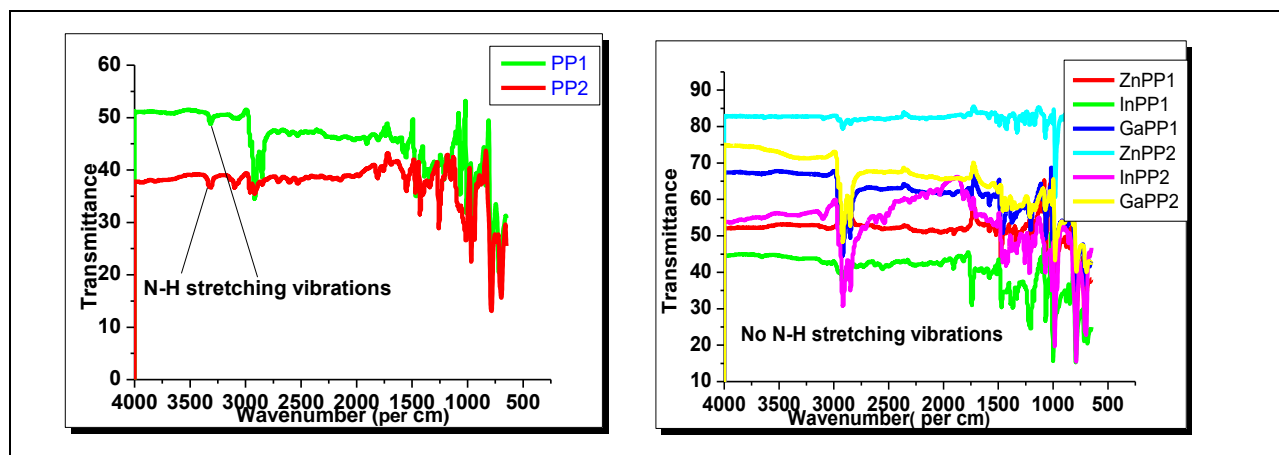
Figure 4.3. FTIR spectra of PP1 and PP2 in comparison to the FTIR spectra of their metal complexes

4.2. Photophysical Studies

The photophysical properties of the synthesized compounds were studied using UV-visible spectroscopy and steady state fluorescence studies. UV-visible spectroscopy was used to ascertain that indeed the molecules absorb in the visible region. The studies also monitored the change in optical properties upon modification. Steady state fluorescence studies were used to assess the extent of fluorescence quenching on metalation. As expected the fluorescence quantum yields for porphyrins reduce on metalation due to enhanced intersystem crossing (Figueiredo *et al*., 1999; Zakavi & Hoseini, 2015).

4.2.1. UV-Visible Spectroscopy

The synthesized porphyrins PP1, PP2 and their metal complexes all showed characteristic absorption spectrum for *etio* type porphyrins with an intense Soret (B band) band between 418−434 nm and four low-intensity bands (Q bands) in the 500-700 nm region (Figure 4.1).

From the experimental data in Table 4.1, there is zero shift in the absorption λ_{max} for PP1 compared to tetraphenylporphyrin (H_2TPP), the reference freebase porphyrin. Both monomers have phenyl groups for substituents at the *meso* position. Phenyl moieties have very minimal influence on the electronic structure of the porphyrins. This is mainly due to the unfavorable steric interaction between β hydrogens of the pyrrole ring and *ortho* hydrogens of the phenyl group essentially

positioning the phenyl substituent orthogonal to the porphyrin core thus increased rotational barrier (Greco *et al*., 2014; Kumar *et al*., 2019).

Table 4.1 The UV-visible absorption data for PP1, PP2 and their metal complexes

	Soret band (nm) $(\varepsilon \times 10^5)$ (L Mol^{-1} cm^{-1})	Q bands (nm) $(\varepsilon \times 10^3)$ (L Mol^{-1} cm^{-1})			
		Q_{y01}	Q_{y00}	Q_{x01}	Q_{x00}
H$_2$TPP	421	515	549	591	649
PP1	421 (2.1)	517 (9.4)	550 (4.5)	593 (2.7)	650 (2.1)
ZnPP1	425 (9.6)	550 (52.8)	589 (10.6)		
InPP1	430 (5.4)	563 (31.0)	602 (13.2)		
GaPP1	424 (6.9)	553 (29.0)	592 (6.2)		
PP2	431 (2.6)	524 (13.5)	561 (7.0)	600 (4.5)	665 (3.7)
ZnPP2	433 (8.0)	559 (51.9)	602 (8.5)		
InPP2	439 (3.0)	570 (15.7)	613 (6.6)		
GaPP2	434 (3.9)	561 (22.7)	604 (4.7)		

However, PP2 which has a thienyl substituent group has its absorption λ_{max} red shifted by 10nm compared to PP1 (Table 4.1). Smaller *meso* substituents like the thienyl groups do not have *ortho* hydrogens thus have a significant effect on the conformation and electronic spectra of porphyrins (Ojadi *et al*., 1993). The thienyl groups of PP2 are smaller than the phenyl groups of PP1 making it easier for the *meso*-aryl rings to adopt a coplanar orientation with the porphyrin core. This enhances the resonance interactions with the tetrapyrrole ring thus improving the π conjugation, which is manifested in the red shift of the Q and B bands of PP2 (Fonda *et al*., 1993; Hayashi *et al*., 2010; Babu, 2019). This trend is also observed for the metal complexes of PP2 in comparison with those of PP1 (Table 4.1).

The absorption λ_{max} for the metal complexes of PP1 and PP2 were red shifted by 2 – 9 nm compared to those of their respective free base monomers (Table 4.1). Metal insertion has the ability to slightly alter the π electron delocalization of the porphyrin ring. Co-ordination of metals at the porphyrin core improves their structural symmetry since the presence of the extra H protons

tilts the pyrrole ring out of plane (Gouterman, 1961; Ojadi *et al*., 1993). Greater resonance interaction with the *meso* substituents is therefore observed due to the reduced steric hindrance and extended conjugation reflected in bathochromic shift (Huang *et al*., 2000; Kumar *et al*., 2019; Polo *et al*., 2004; Smith, 1975). Among the metallated porphyrins, Indium complexes exhibited the largest shift between 8−9 nm, a scenario that was also observed in other published works (Hong *et al*., 1996; Saenz *et al*., 2011; Soy *et al*., 2019).

Similar observations have been observed in previous research all which concluded that changes in the conjugation pathway and symmetry of a porphyrin can affect its electronic properties (Huang *et al*., 2000; Kim, 2012; Kumar *et al*., 2005; Managa, *et al*., 2017b; Sessler & Burrell, 1992).

Upon metalation, the four Q bands in PP1 and PP2 collapse to just two bands in the metal complexes. Increase in molecular symmetry from D_{2h} to D_{4h} produces a simplification of the Q band patterns upon metalation as would normally be anticipated (Gouterman, 1961; Nemykin & Hadt, 2010). Reduction of the Q bands is a characteristic feature in metalloporphyrins further confirming the successful insertion of metal ions into the porphyrin core.

4.2.2. Steady state Fluorescence Spectroscopy

All the synthesized porphyrins exhibited two emission bands as shown in Figure 4.4, characteristic for porphyrins corresponding to Q_{00} and Q_{01} transitions (Fery-Forgues & Lavabre, 1999; Figueiredo *et al*., 1999; Sen *et al*., 2010). From the fluorescence spectra (Figure 4.4), emission
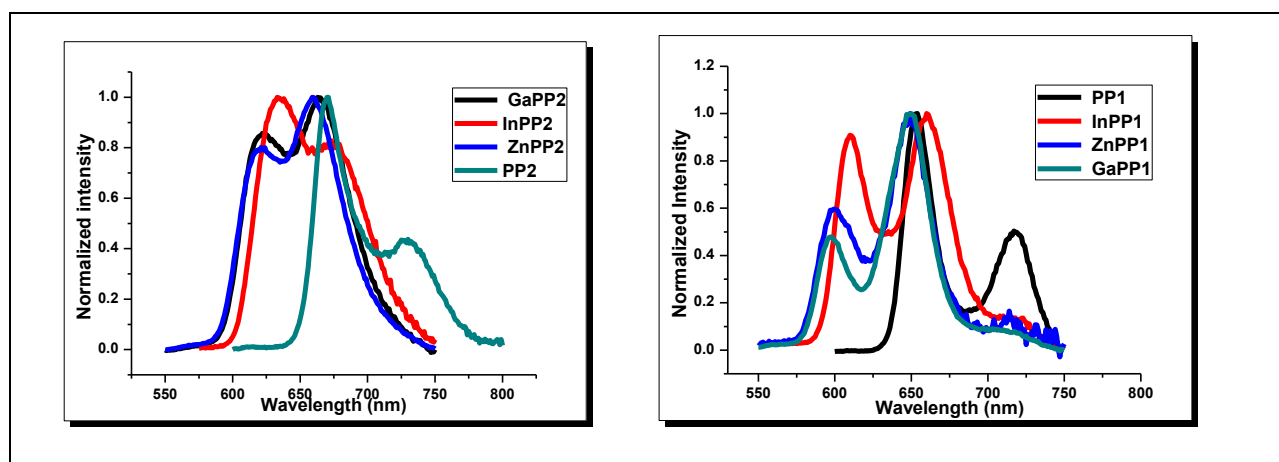
Figure 4.4. Fluorescence spectra of PP1, PP2 and their metal complexes in toluene

43

bands of PP1, PP2 and their metal complexes are similar except for different maxima emission peaks. Metalloporphyrins exhibited low intensity and blue shifted emission bands compared to the freebases.

As shown in Table 4.2, fluorescence quantum yields (Φ_F) for the metallated porphyrins were lower compared to those of PP1 and PP2. This is associated with the heavy atom effect of the metal ensuring strong spin orbit coupling which encourages intersystem crossing (Gupta & Ravikanth, 2005; Nyarko *et al*., 2004; Zakavi & Hoseini, 2015). Improved ISC populates the triplet states lowering fluorescence quantum yield (Figueiredo *et al*., 1999; Managa *et al*., 2017). The Φ_F for indium metallated porphyrins were the lowest with both InPP1 and InPP2 less than 0.01. The τ_F values for metallo-porphyrins were shorter than those of free base porphyrins due to the heavy atom effect thus more excited electrons presumed to have crossed into the triplet state.

Table 4.2. Photophysical parameters of PP1, PP2 and their metal complexes in toluene

	λ_{em} (nm)		Stoke shift cm^{-1}	Φ_F	τ_F (ns)	k_r(10^8 s^{-1})	k_{nr}(10^8 s^{-1})
	Q_{00}^*	Q_{01}^*					
PP1	654	717(sh)	8460	0.0190	1.55 ± 0.02	0.123	6.33
ZnPP1	600 (sh)	649	8120	0.0097	0.38 ± 0.01	0.255	26.1
InPP1	610(sh)	660	8100	0.0056	0.24 ± 0.02	0.233	41.4
GaPP1	597(sh)	650	8200	0.0129	0.48 ± 0.01	0.269	20.6
PP2	670	730(sh)	8280	0.0170	1.37 ± 0.02	0.124	7.18
ZnPP2	621(sh)	659	7920	0.0118	0.54 ± 0.01	0.219	18.3
InPP2	633	673(sh)	6980	0.0096	0.29 ± 0.02	0.331	34.2
GaPP2	624(sh)	663	7960	0.0127	0.53 ± 0.01	0.240	18.6

In conclusion, these photophysical studies found the synthesized compounds suitable for application in extending the usability of TiO_2 as a photocatalyst into the visible spectrum.

4.3. Density Function Theory Calculations

Density functional theory (DFT) computations were performed to help model suitable compounds for photosensitization as well as compute the photophysical properties of the synthesized porphyrins for comparison with experimental values. The calculations can be used as a modelling tool to facilitate selection and synthesis of suitable compounds for photosensitization in future. The Computed optimized geometries are shown in Appendix I1. The DFT calculated absorption spectral data for all the synthesized porphyrins along with the experimental λ_{max} values are listed in Table 4.3 and simulated spectra in Appendix I2.

Table 4.3. Computed electronic excitation spectral bands of the synthesized porphyrins at TD-DFT level of theory using CAM-B3LYP functions with mixed SDD and 6-31G(d,p) basis sets

	Band[a]	#[b]	Calc[c]			Exp[d]		Wave function[e]
	-	1	-	-	-	-	-	Ground state
PP1	Q	2	16839	594	0.013	15384	650	**59% s→-a ; 40% a →-s ; …**
	Q	3	18509	540	0.032	17064	586	**58% s→-s ; 42% a →-a ; …**
	B	4	25772	388	1.840	23735	421	**58% a→-s ; 37% s →-a ; …**
	B	5	26224	381	2.131	-	-	**58% a→-a ; 42% s →-s ; …**
	-	1	-	-	-	-	-	Ground state
PP2	Q	2	16416	609	0.016	15037	665	**57% s→-a ; 41% a →-s ; …**
	Q	3	17914	558	0.078	16611	602	**61% s→-s ; 38% a →-a ; …**
	B	4	24820	402	1.885	23202	431	**57% a→-s ; 39% s →-a ; …**
	B	5	25305	395	2.081	-	-	**61% a→-a ; 39% s →-s ; …**

	Band[a]	#[b]	Calc[c]			Exp[d]		Wave function[e]
	-	**1**	-	-	-	-	-	Ground state
ZnPP2	**Q**	**2,3**	17884	559	0.012	16619	602	**51% s→-a/-s ; 42% a →-a/-s**
	B	**4,5**	25327	394	1.950	23095	433	**49% a→-a/-s ; 44% s →-a/-s**
	-	**1**	-	-	-	-	-	Ground state
InPP2	**Q**	**2,3**	17405	574	0.033	16234	616	**57% s→-a/-s ; 42% a →-a/-s**
	B	**4,5**	25072	398	2.015	22779	439	**55% a→-a/-s ; 44% s →-a/-s**
	-	**1**	-	-	-	-	-	Ground state
GaPP2	**Q**	**2,3**	18137	551	0.024	16584	603	**56% s→-a/-s ; 43% a →-a/-s**
	B	**4,5**	25852	386	1.961	23042	434	**54% a→-a/-s ; 45% s →-a/-s**
	-	**1**	-	-	-	-	-	Ground state
ZnPP1	**Q**	**2,3**	18377	544	0.008	17036	587	**52% s→-a/-s ; 46% a →-a/-s**
	B	**4,5**	26268	380	2.057	23530	425	**53% a→-a/-s ; 46% s →-a/-s**
	-	**1**	-	-	-	-	-	Ground state
InPP1	**Q**	**2,3**	17318	577	0.092	16638	601	**67% s→-a/-s ; 31% a →-a/-s**
	B	**6,7**	24955	400	1.496	23255	430	**62% a→-a/-s ; 29% s →-a/-s**
	-	**1**	-	-	-	-	-	Ground state
GaPP1	**Q**	**2,3**	17790	562	0.105	16977	589	**68% s→-a/-s ; 30% a →-a/-s**
	B	**4,5**	25467	392	1.619	23584	424	**63% a→-a/-s ; 29% s →-a/-s**

[a] Band assignment referred to in this work. [b] Energy states assigned in ascending order [c] Calculated band energies (cm^{-1}), wavelengths (nm) and oscillator strengths in brackets (f). [d] Observed energies (cm^{-1}) and wavelengths (nm), [e] The wave functions based on the eigenvectors predicted by TD-DFT. Transitions for one electron between the **a**, **s**, **-a** and **–s** MOs are highlighted in bold.

In reasonable agreement with the experimental data, the DFT simulated spectra of the compounds exhibited an intense soret band in the range 380 – 402 nm which corresponds to those seen in the experimental data of 420 – 439nm. Simulated absorption λ_{max} for PP2 (402nm) was more red shifted compared to PP1(388nm), a scenario that was similar to those seen in experimental values.

This shift is due to the effect of the thienyl substituent group in PP2. Simulated spectral data for the metal complexes of the porphyrins showed a general red shift compared with the free base monomers, a similar trend observed in the experimental data. Indium metalloporphyrins were more red shifted than those of zinc and gallium consistent with the trend seen experimentally (Table 4.3).

The corresponding oscillator strength for the soret band was in the range of 2.131 to 1.496. The electron transition responsible for the appearance of this band was a vertical excitation from $S_0 \rightarrow S_3$ or $S_0 \rightarrow S_4$ (apart from InPP1 where it was due to $S_0 \rightarrow S_6$ or $S_0 \rightarrow S_7$). DFT showed the Soret band originated from a majority contribution of transitions from HOMO-1 to LUMO/ LUMO+1 which accounts for 49% to 63% (Table 4.3). From the computational optimized structures Appendix I1, the LUMO/ LUMO+1 are degenerate.

Only two bands are seen from the simulated spectral data instead of the four Q bands in the case of PP1 and PP2 while for the metallated porphyrins, only one Q band is seen instead of the two in the experimental data. Their oscillator strengths are weaker compared to those of the soret band agreeing with the less intense Q bands obtained experimentally. The Q bands mainly are a result of contributions from HOMO to LUMO/ LUMO+1 transitions.

4.3.1. Suitability for Electron Injection
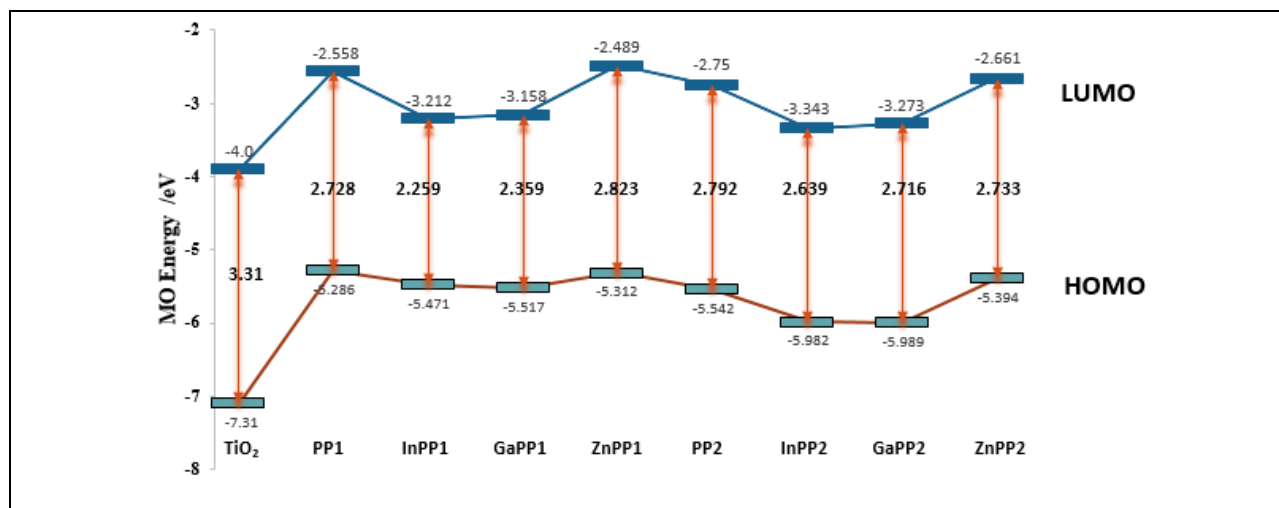
Figure 4.5. Calculated energy levels and HOMO−LUMO gaps for TiO$_2$, PP1, PP2 and the metal porphyrin complexes

47

Figure 4.5 illustrates that both the HOMO and LUMO levels of these sensitizers fit the requirements needed for an efficient photosensitizer (Santhanamoorthi *et al*., 2013). The LUMO levels of the photosensitizers lie between −2.49 and −3.34 eV well above the lower bound level of the TiO_2 CB (ca. −4.0 eV) implying that the efficiency of electron injection from the photoexcited sensitizer to the TiO_2 CB as viable (Paredes-Gil *et al*., 2017). Kubelka Munk function plot was used to calculate TiO_2 band gap using DRS data.

4.4. Characterization of the P-TiO₂ photocatalysts
4.4.1. Diffuse Reflectance Spectroscopy

UV-visible diffuse reflectance was used to study the optical properties of the porphyrin-TiO_2 (P−TiO_2) nanocomposite. The P-TiO_2 composites exhibited absorption peaks characteristic of the B bands and Q bands seen in porphyrins, Figure 4.6. Usually, TiO_2 does not exhibit any absorption above 400 nm. The spectral data suggest that the porphyrins were indeed successfully deposited onto the surface of TiO_2 and the P-TiO_2 composite formed. This is of considerable importance as the P-TiO_2 photocatalyst therefore has potential to extend the optical properties of TiO_2 into the visible spectrum.
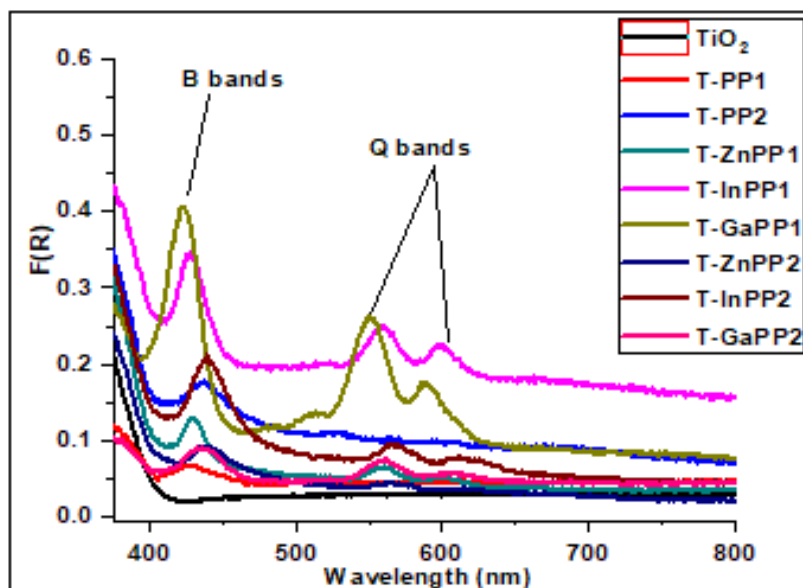
Figure 4.6. Diffuse Reflectance spectra of the photocatalysts

4.4.2. FT-IR Spectroscopy

To identify the bonding characteristics of the functional groups in TiO_2 and the P-TiO_2 photocatalysts, FTIR analysis was performed. The broad absorption band at 3600–2900 cm^{-1} was assigned to O-H str vibrations that arise from the interaction of hydroxyl groups of water molecules on the TiO_2 surface (Figure 4.7). The vibrational peaks of the hydroxyl group on the P-TiO_2 surface became weaker compared to those of TiO_2 due to interactions with the porphyrin in the P-TiO_2 photocatalysts. The peak at 1650 cm^{-1} arises from the characteristic bending vibration of the –OH group (Sen *et al*., 2010). Additionally, weak C=C and C=N porphyrin vibration modes lie between 1500–1700 cm^{-1} and this provides evidence for the successful deposition on TiO_2 (Fuhrhop *et al*., 1992).
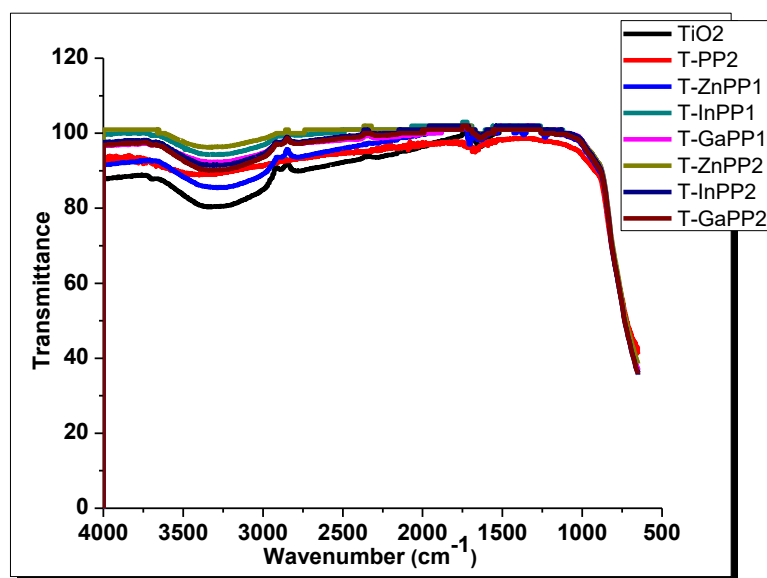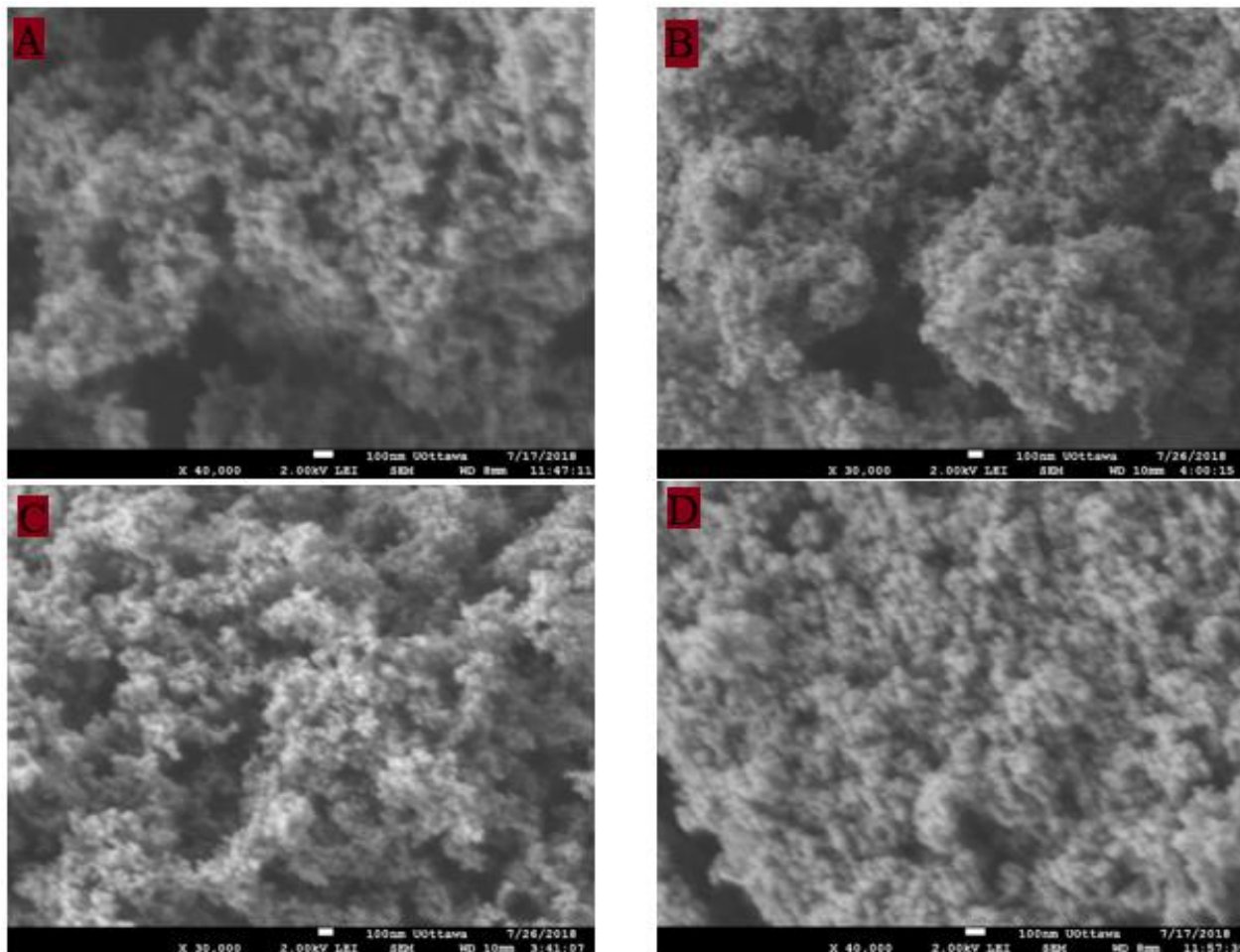

Figure 4.7. FTIR spectra of the photocatalysts

4.4.3. Scanning Electron Microscopy

The morphologies of the photocatalysts were observed by SEM. The images (Figure 4.8) showed large aggregate particles in the nanometre range (ca. 30 nm) that are not individually discernible. The P-TiO_2 photocatalysts had textures that were similar to those of TiO_2.

49

Figure 4.8. SEM micrographs of TiO_2 (A), ZnPP1-TiO_2 (B), InPP1-TiO_2 (C) and GaPP2-TiO_2 (D)

4.5. Photocatalytic Activity of the Photocatalysts

4.5.1. Methylene Blue Degradation

Degradation of organic compounds can be utilized as an excellent way to assess the activity of photocatalysts. The photocatalytic degradation activity of the P-TiO_2 composites were determined using methylene blue (MB), a model organic compound. Seven of the composites namely: ZnPP1-TiO_2, GaPP1-TiO_2, GaPP2-TiO_2, InPP2-TiO_2, PP1-TiO_2, PP2-TiO_2 and ZnPP2-TiO_2, were assessed for their ability to photocatalytically degrade MB.

The degradation profile of methylene blue (MB) in the presence of ZnPP1-TiO_2 under solar simulator (SolSim) irradiation is shown in Figure 4.9. Similarly, the degradation pattern of the

other composites was determined and are given in Appendix J. The concentration of MB (initial concentration 5.023×10^{-3} Mm/L, 20 ml) gradually decreases with time and the solution turns colourless from its initial blue colour indicating the total degradation of MB.
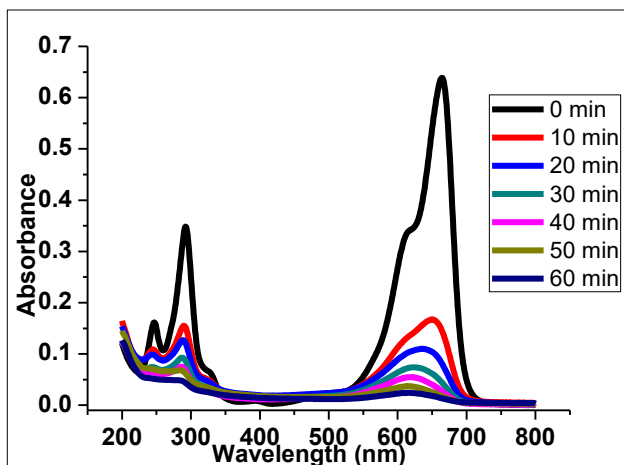
Figure 4.9. Spectral changes for the MB solution under SolSim irradiation in the presence of ZnPP1-TiO$_2$

Table 4.4 shows only ZnPP1-TiO$_2$, GaPP1-TiO$_2$ and ZnPP2-TiO$_2$ showed better photocatalytic activity than bare nanometric TiO$_2$. This could be ascribed to the fact that the porphyrins had additional absorption of photons in the visible spectrum thus more ROS produced aiding degradation as previously suggested. After 10 min of irradiation, only 72.4 % of MB had been degraded by TiO$_2$ catalyst whereas ZnPP1-TiO$_2$, GaPP1-TiO$_2$ and ZnPP2-TiO$_2$ catalysts registered 77.7%, 74.8% and 78.0% degradation respectively. Although PP1-TiO$_2$, GaPP2-TiO$_2$, PP2-TiO$_2$ and InPP2-TiO$_2$ exhibited lower degradation activities than TiO$_2$, all of the catalysts reached 95% efficiency after 40 min. Degradation efficiency was calculated by Equation (4.1).

Table 4.4. Calculated degradation efficiency of MB for different catalysts

Irradiation time (Min)	Catalysts efficiency in %							
	TiO$_2$	PP1- TiO$_2$	ZnPP1- TiO$_2$	GaPP1- TiO$_2$	PP2- TiO$_2$	ZnPP2- TiO$_2$	InPP2- TiO$_2$	GaPP2- TiO$_2$
10	72.38	68.81	77.71	74.78	62.60	78.01	68.48	65.69
20	85.92	83.46	88.79	86.44	79.95	86.88	82.08	80.17
30	92.48	90.08	93.64	92.62	90.91	93.47	91.28	89.52
40	96.18	94.99	96.46	96.19	95.73	96.25	95.81	94.23

$$\left[\frac{C_o - C_t}{C_o}\right] \times 100\ \% \tag{4.1}$$

where C_o is the initial concentration of MB and C_t is the residual concentration of MB after t minutes of irradiation at 664nm.

To characterize the reaction kinetics of the MB degradation reaction quantitatively, the Langmuir-Hinshelwood model was used, which is expressed by Equation (4.2).

$$-\ln\left[\frac{C_t}{C_O}\right] = \ kt \tag{4.2}$$

where k is the first order rate constant. The reaction rate constant, k, was determined with a first order regression linear fit (Appendix K).

Table 4.5. Kinetic parameters of MB degradation with different photo-catalysts

Photo-catalyst	k/min $\times\ 10^{-2}$	R
TiO_2	6.867	0.9725
PP1-TiO_2	6.643	0.9711
ZnPP1-TiO_2	6.942	0.9867
GaPP1-TiO_2	6.991	0.9728
PP2-TiO_2	6.788	0.9835
ZnPP2-TiO_2	6.947	0.9828
InPP2-TiO_2	6.908	0.9893
GaPP2-TiO_2	6.522	0.9887

Efficient photocatalysts usually exhibit high values of k. The typical values of k under SolSim irradiation are compiled in Table 4.5. The magnitude of the k values follows the order GaPP1-TiO_2 > ZnPP2-TiO_2 > ZnPP1-TiO_2 > TiO_2 > InPP2-TiO_2 > PP2-TiO_2 > PP1-TiO_2 > GaPP2-TiO_2.

The composites with metalloporphyrins deposited on their surface showed better degradation than their counterparts with freebase porphyrins on them. This could be a result of fluorescence quenching on metalation thus more ROS produced (Figueiredo *et al.*, 1999).

According to the proposed MB degradation pathway and identification of metabolites of degradation by Houas, the final products were identified as CO_2, NH_4^+, NO_3^- and SO_4^{2-} (Houas, 2001).

4.5.2. Hydrogen Generation

The The activity of the P-TiO$_2$ photocatalysts in generation of hydrogen from sacrificial electron donor (SED) in aqueous solution was evaluated for each of the photocatalysts. Eight photocatalysts namely: ZnPP1-TiO$_2$, GaPP1-TiO$_2$, GaPP2-TiO$_2$, InPP2-TiO$_2$ ZnPP2-TiO$_2$, InPP1-TiO$_2$, PP1-TiO$_2$, and PP2-TiO$_2$ were assessed in 1% methanol solution. Previous studies reported that true water splitting without SED assistance was largely inefficient (Guzman *et al.*, 2013; Hainer *et al.*, 2018; Rahman *et al.*, 2020). The simultaneous oxidation and reduction of water is energetically unfavourable ($\Delta H_0 = 286$ kJ Mol^{-1}) resulting from a complicated reaction involving four electrons (Kumaravel *et al.*, 2019). Sacrificial agents like methanol scavenges the holes created at the valence band greatly reducing chances of charge carrier recombination. This is manifested in enhanced H$_2$ production yield. (Lanterna & Scaiano, 2017; Schneider & Bahnemann, 2013).
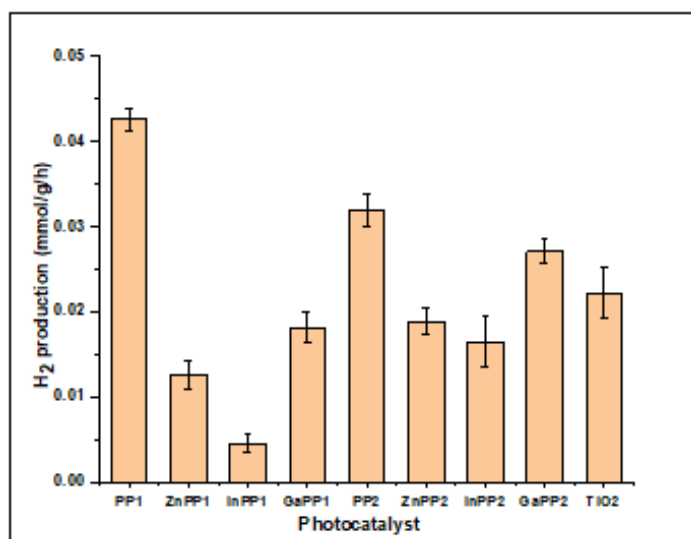

Figure 4.10. Hydrogen generation rates in 1% methanol solution under SolSim.

All the photocatalysts showed potential to generate H_2 (Fig 4.10). PP1-TiO$_2$, PP2-TiO$_2$ and GaPP2-TiO$_2$ showed superior photocatalytic activity rate in terms of H_2 generation than bare TiO$_2$.

4.5.3. Mechanism of photocatalysis

Based on the results, a possible photocatalytic mechanism for the degradation of MB by the porphyrin sensitized TiO$_2$ relies on electron injection and subsequent generation of ROS as summarized in Scheme 4.9. Photoinduced electrons generated by the porphyrins upon excitation by visible light are injected to the TiO$_2$ conduction band(CB). The presence of UV light enables more electrons to move to the TiO$_2$ CB leaving holes, which have exceptional electrophilic properties in the valency band(VB) (Hainer *et al.*, 2018). Electrons in the CB subsequently transfer their energy to dissolved oxygen generating peroxyl radicals. A series of oxidation reactions follow producing more hydroxyl radicals, which in turn results in the degradation of MB (Hancock-Chen and Scaiano, 2000; Houas, 2001).
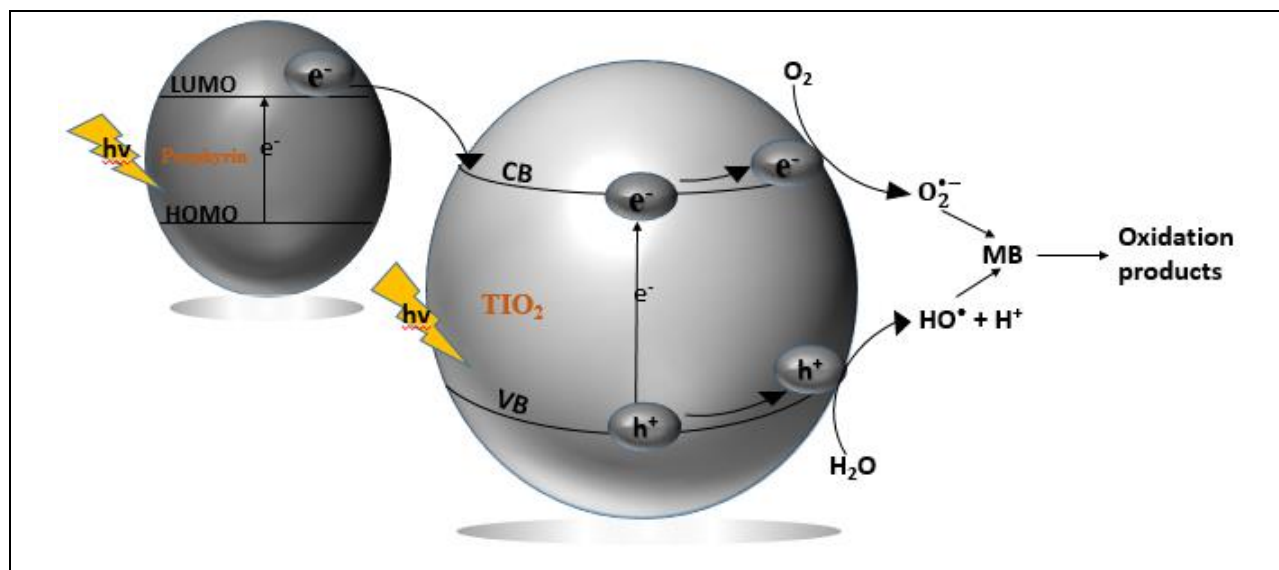
Scheme 4.9. A proposed scheme for MB degradation over TiO$_2$ after photosensitization with porphyrin

A summarized illustration of the proposed hydrogen generation mechanism is shown in Scheme 4.10. Under simulated irradiation, charge carriers (e^- and h^+) are photo-generated on the TiO_2. Excited electrons generated by the visible light on the porphyrin LUMO will subsequently be injected into the TiO_2 CB. This is followed by methanol oxidation to yield formaldehyde through e^- injection into the TiO_2 conduction band exhibited by a doubling effect in hydrogen production.
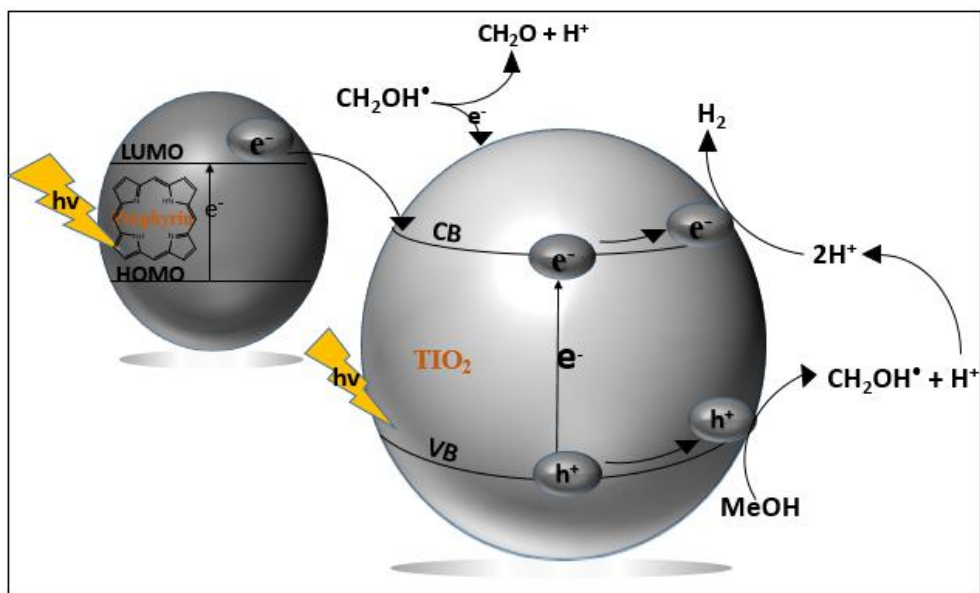
Scheme 4.10. Proposed scheme for hydrogen generation over TiO_2

CHAPTER FIVE

CONCLUSIONS AND RECOMMENDATIONS

5.1. Conclusions

The conclusions drawn from this study are:

1. *Meso*-tetra(4-bromophenyl)porphyrin (PP1) and *meso*-tetra(5-bromo-2-thienyl)porphyrin (PP2) and their Zn, In and Ga complexes were successfully synthesized and characterized.
2. The optical properties of the synthesized porphyrins were investigated and found suitable for photoexcitation applications on TiO_2 photocatalyst.
3. The P-TiO_2 composites showed enhanced photocatalytic activity over bare P-25 TiO_2 hence has potential application in degradation of organic pollutants in water as well as generation of hydrogen energy.

5.2. Recommendations

For further studies, the following recommendations can be considered:

1. Since the photocatalytic study of the system was investigated under complete solar spectra only, the use of visible light only should be explored in future to selectively account for the effect of electron injection from the dye to the TiO_2 conduction band.

2. Future studies should consider adding anchoring groups to the porphyrins to enhance a stronger interaction with the semiconductor thus improve the efficiency of electron injection.

3. Bulkier substituent groups with extended conjugation can be considered to further enhance the absorption of the porphyrin photosensitizer in the visible spectrum.

REFERENCES

Adams C., Wang Y., Loftin K. & Meyer M. (2002) Removal of Antibiotics from Surface and Distilled Water in Conventional Water Treatment Processes. *Journal of Environmental Engineering* **128**(3), 253–260.

Adler, A. D., Longo, F. R., Finarelli, J. D., Goldmacher, J., Assour, J. & Korsakoff, L. (1967) A simplified synthesis for meso-tetraphenylporphine. *The Journal of Organic Chemistry* **32**(2), 476–476.

Altobello, S., Bignozzi, C. A., Caramori, S., Larramona, G., Quici, S., Marzanni, G. & Lakhmiri, R. (2004) Sensitization of TiO_2 with ruthenium complexes containing boronic acid functions. *Journal of Photochemistry and Photobiology A: Chemistry* **166**(1), 91–98.

Alves, E., Faustino, M. A. F., Neves, M. G. P. M. S., Cunha, Â., Nadais, H. & Almeida, A. (2015) Potential applications of porphyrins in photodynamic inactivation beyond the medical scope. *Journal of Photochemistry and Photobiology C: Photochemistry Reviews* **22**, 34–57.

Amos-Tautua, B., Songca, S. & Oluwafemi, O. (2019) Application of Porphyrins in Antibacterial Photodynamic Therapy. *Molecules* **24**(13), 2456.

Babu, B., Amuhaya, E., Oluwole, D., Prinsloo, E., Mack, J. & Nyokong, T. (2019) Preparation of NIR absorbing axial substituted tin(IV) porphyrins and their photocytotoxic properties. *Medicinal Chemistry Communications* **10**, 41–48.

Balat, M. (2008) Potential importance of hydrogen as a future solution to environmental and transportation problems. *International Journal of Hydrogen Energy* **33**(15), 4013–4029.

Becke, A. D. (1993) Density-functional thermochemistry. III. The role of exact exchange. *The Journal of Chemical Physics* **98**(7), 5648–5652.

Biesaga, M., Pyrzyńska, K. & Trojanowicz, M. (2000) Porphyrins in analytical chemistry. A review. *Talanta* **51**(2), 209–224.

Bockris, J. (2002) The origin of ideas on a Hydrogen Economy and its solution to the decay of the environment. *International Journal of Hydrogen Energy* **27**(7–8), 731–740.

BP Statistical Review of World Energy (2019). https://www.bp.com/content/dam/bp/business-sites/en/global/corporate/pdfs/energy-economics/statistical-review/bp-stats-review-2019-full-report.pdf *Accessed on 24th January, 2019*

Cai, X. & Rosegrant, M. W. (2002) Global Water Demand and Supply Projections. *Water International* **27**(2), 159–169.

Campbell, W. M., Jolley, K. W., Wagner, P., Wagner, K., Walsh, P. J., Gordon, K. C., Schmidt-Mende, L., Nazeeruddin, M. K., Wang, Q., Grätzel, M. & Officer, D. L. (2007) Highly Efficient Porphyrin Sensitizers for Dye-Sensitized Solar Cells. *The Journal of Physical Chemistry C* **111**(32), 11760–11762.

Cassidy, C.M., Donnelly, R.F. & Tunney, M. (2010) Effect of sub lethal challenge with photodynamic antimicrobial chemotherapy on the antibiotic susceptibility of clinical bacterial isolates. *Journal of Photochemistry Photobiology* **99**, 62-66.

Chang, M.Y., Hasieh, Y.H., Cheng, T.C., Yao, K.S., Wei, M.C. & Chang, C.Y. (2009) Photocatalytic degradation of 2,4-dichlorophenol wastewater using porphyrin/TiO2 complexes activated by visible light. *Thin Solid Films* **517**(14), 3888–3891.

Chen, X., Shen, S., Guo, L. & Mao, S. S. (2010) Semiconductor-based Photocatalytic Hydrogen Generation. *Chemical Reviews* **110**(11), 6503–6570.

Cho, Y., Park, Y. & Choi, W. (2008) Ruthenium bipyridyl complex-sensitized dechlorination of CCl_4 in aqueous micellar solutions under visible light. *Journal of Industrial and Engineering Chemistry* **14**(3), 315–321.

Chow, J. (2003) Energy Resources and Global Development. *Science*,**302**(5650), 1528–1531.

Chowdhury, P., Moreira, J., Gomaa, H. & Ray, A. K. (2012) Visible-Solar-Light-Driven Photocatalytic Degradation of Phenol with Dye-Sensitized TiO_2: Parametric and Kinetic Study. *Industrial & Engineering Chemistry Research* **51**(12), 4523–4532.

Cosgrove, W. J. & Loucks, D. P. (2015) Water management: Current and future challenges and research directions: Water management research challenges. *Water Resources Research* **51**(6), 4823–4839.

Crossley, M. J., Thordarson, P. & Wu, R. (2001) Efficient formation of lipophilic dihydroxotin(IV) porphyrins and bis-porphyrins. *Journal of the Chemical Society, Perkin Transactions 1* **18**, 2294–2302.

Daghrir, R., Drogui, P. & Robert, D. (2013) Modified TiO_2 for Environmental Photocatalytic Applications: A Review. *Industrial & Engineering Chemistry Research* **52**, 3581–3599.

Dong, H., Zeng, G., Tang, L., Fan, C., Zhang, C., He, X. & He, Y. (2015) An overview on limitations of TiO$_2$ based particles for photocatalytic degradation of organic pollutants and the corresponding countermeasures. *Water Research* **79**, 128–146.

Dougherty, W., Kartha, S., Rajan, C., Lazarus, M., Bailie, A., Runkle, B. & Fencl, A. (2009) Greenhouse gas reduction benefits and costs of a large-scale transition to hydrogen in the USA. *Energy Policy* **37**(1), 56–67.

Duan, M., Li, J., Mele, G., Wang, C., Lü, X., Vasapollo, G. & Zhang, F. (2010) Photocatalytic Activity of Novel Tin Porphyrin/TiO$_2$ Based Composites. *The Journal of Physical Chemistry C* **114**(17), 7857–7862.

Dunn, S. (2002) Hydrogen futures: Toward a sustainable energy system. *International Journal of Hydrogen Energy* **27**(3), 235–264.

Elghamry, I., Ibrahim, S., Abdelsalam, M., AL-Faiyz, Y. & Al-Qadri, M. (2018) Synthesis, Thermal Stability and Electrocatalytic Activities of meso-tetrakis (5-bromothiophen-2-yl) Porphyrin and Its Cobalt and Copper Complexes. *International Journal of Electrochemical Science* 10233–10246.

Elhage, A. A., Scaiano, J. C. & Lanterna, A. E. (2019) Dressing up for the occasion: The many faces of decorated titanium dioxide in photocatalysis. In: *Photoactive Inorganic Nanoparticles*, Elsevier Inc, 73–108.

Elsellami, L., Pigeot-Rémy, S., Dappozze, F., Vocanson, F., Houas, A. & Guillard, C. (2010) Comparison of initial photocatalytic degradation pathway of aromatic and linear amino acids. *Environmental Technology* **31**(13), 1417–1422.

Fadda, A. A., El-Mekawy, R. E., El-Shafei, A. I. & Freeman, H. (2013) Synthesis and Pharmacological Screening of Novel meso-Substituted Porphyrin Analogs. *Archiv Der Pharmazie* **346**(1), 53–61.

Fery-Forgues, S. & Lavabre, D. (1999) Are Fluorescence Quantum Yields So Tricky to Measure? A Demonstration Using Familiar Stationery Products. *Journal of Chemical Education* **76**(9), 1260.

Figueiredo, T. L. C., Johnstone, R. A. W., Sørensen, A. M. P. S., Burget, D. & Jacques, P. (1999) Determination of Fluorescence Yields, Singlet Lifetimes and Singlet Oxygen Yields of

Water-Insoluble Porphyrins and Metalloporphyrins in Organic Solvents and in Aqueous Media. *Photochemistry and Photobiology* **69**(5), 517–528.

Fischer, H. & Klarer, J. (1926) Synthese des Ätioporphyrins, Ätiohämins und Ätiophyllins. *Justus Liebig's Annalen der Chemie* **448**(1), 178–193.

Fonda, H. N., Gilbert, J. V., Cormier, R. A., Sprague, J. R., Kamioka, K. & Connolly, J. S. (1993) Spectroscopic, photophysical, and redox properties of some meso-substituted free-base porphyrins. *The Journal of Physical Chemistry* **97**(27), 7024–7033.

Frisch, M. J., Trucks, G. W., Schlegel, H. B., Scuseria, G. E., Robb, M. A., Cheeseman, J. R., Scalmani, G., Barone, V., Mennucci, B. & Petersson, G. A. (2015) Gaussian 09, Revision A. 02; Gaussian, Inc: Wallingford, CT, 2009.

Fuhrhop, J. H., Demoulin, C., Boettcher, C., Koening, J. & Siggel, U. (1992) Chiral micellar porphyrin fibers with 2-aminoglycosamide head groups. *Journal of the American Chemical Society* **114**(11), 4159–4165.

Fyfe, W. S., Powell, M. A., Hart, B. R. & Ratanasthien, B. (1993) A global crisis: Energy in the future. *Nonrenewable Resources* **2**(3), 187–196.

Gaya, U. I. & Abdullah, A. H. (2008) Heterogeneous photocatalytic degradation of organic contaminants over titanium dioxide: A review of fundamentals, progress and problems. *Journal of Photochemistry and Photobiology C: Photochemistry Reviews* **9**(1), 1–12.

Global Energy Transformation*: A Roadmap to 2050 (*2019*)*. https://www.irena.org/publications/2019/Apr/Global-energy-transformation-A-roadmap-to-2050-2019Edition. *Accessed on 7th July, 2019*.

Goel, P. K. (2006) *Water Pollution: Causes, Effects and Control*. New Age International, New Delhi, 22.

Gouterman, M. (1961) Spectra of porphyrins. *Journal of Molecular Spectroscopy* **6**, 138–163.

Grätzel, M. (2003) Dye-sensitized solar cells. *Journal of Photochemistry and Photobiology C: Photochemistry Reviews* **4**(2), 145–153.

Graymore, M., Stagnitti, F. & Allinson, G. (2001) Impacts of atrazine in aquatic ecosystems. *Environment International* **26**(7–8), 483–495.

Greco, J. A., Rossi, A., Birge, R. R. & Brückner, C. (2014) A Spectroscopic and Theoretical Investigation of a Free-Base *meso-* Trithienylcorrole. *Photochemistry and Photobiology* **90**(2), 402–414.

Gupta, I. & Ravikanth, M. (2005) Fluorescence properties of meso-tetrafurylporphyrins. *Journal of Chemical Sciences* **117**(2), 161–166.

Guzman, F., Chuang, S.S.C. & Yang, C. (2013) Role of Methanol Sacrificing Reagent in the Photocatalytic Evolution of Hydrogen. *Industrial & Engineering Chemistry Research* **52**, 61–65.

Hainer, A. S., Hodgins, J. S., Sandre, V., Vallieres, M., Lanterna, A. E. & Scaiano, J. C. (2018) Photocatalytic Hydrogen Generation Using Metal-Decorated TiO_2: Sacrificial Donors vs True Water Splitting. *ACS Energy Letters* **3**(3), 542–545.

Hamblin, A. M. R. & Jori, G. (2011) Photodynamic Inactivation of Microbial Pathogens Medical and Environmental Applications: Light Strikes Back Microorganisms in the New Millennium. *Photochemistry and Photobiology 87*(6), 1479–1479.

Hammer, D. A. (1989) *Constructed Wetlands for Wastewater Treatment: Municipal, Industrial and Agricultural*. Lewis Publishers, New York, 145.

Hancock-Chen, T. & Scaiano, J. C. (2000) Enzyme inactivation by TiO_2 photosensitization. *Journal of Photochemistry and Photobiology B: Biology* **57**(2–3), 193–196.

Hayashi, S., Inokuma, Y. & Osuka, A. (2010) *Meso* -Tris(oligo-2,5-thienylene)-Substituted Subporphyrins. *Organic Letters* **12**(18), 4148–4151.

Hirscher, M. (2010) *Handbook of Hydrogen Storage: New Materials for Future Energy Storage*. John Wiley & Sons, Weinheim, 1-35.

Hong, T.N., Sheu, Y.H., Jang, K.W., Chen, J.H., Wang, S.S., Wang, J.C. & Wang, S.L. (1996) A new synthesis of acetato porphyrinato indium(III) from indium(III) oxide and X-ray crystal structures of In (tpyp)(OAc) and In (tmpp)(OAc). *Polyhedron* **15**(15), 2647–2654.

Horng-Huey, K., Chen, H.T., Yen, F.L., Lu, W.C., Kuo, C.W. Wang, M.C. (2012) Preparation of TiO_2 Nanocrystallite Powders Coated with ZnO for Cosmetic Applications in Sunscreens. *International Journal of Molecular Sciences* **13**, 1658–1669.

Hossain, K. A. (2012) Global energy consumption pattern and GDP. *International Journal of Renewable Energy Technology Research* **1**, 23–29.

Houas, A. (2001) Photocatalytic degradation pathway of methylene blue in water. *Applied Catalysis B: Environmental* **31**(2), 145–157.

Hu, Y., Geissinger, P. & Woehl, J. C. (2011) Potential of protoporphyrin IX and metal complexes for single molecule fluorescence studies. *Journal of Luminescence* **131**(3), 477–481.

Huang, H., Gu, X., Zhou, J., Ji, K., Liu, H. & Feng, Y. (2009) Photocatalytic degradation of Rhodamine B on TiO_2 nanoparticles modified with porphyrin and iron-porphyrin. *Catalysis Communications***11**(1), 58–61.

Huang, L., Xuan, Y., Koide, Y., Zhiyenlayev, T., Tanak, M. & Hamblin, M.R. (2012) Type I and Type II mechanisms of antimicrobial photodynamic therapy: An in vitro study of gram negative and gram positive bacteria. *Lasers in Surgery and Medicine* **44**, 490-499.

Huang, X., Nakanishi, K. & Berova, N. (2000) Porphyrins and metalloporphyrins: Versatile circular dichroic reporter groups for structural studies. *Chirality* **12**(4), 237–255.

Jafari, T., Moharreri, E., Amin, A. S., Miao, R., Song, W. & Suib, S. L. (2016) Photocatalytic Water Splitting-The Untamed Dream: A Review of Recent Advances. *Molecules (Basel, Switzerland)*, **21**(7), 900.

Jemli, M., Alouini, Z., Sabbahi, S. & Gueddari, M. (2002) Destruction of fecal bacteria in wastewater by three photosensitizers. *Journal of Environmental Monitoring* **4**(4), 511–516.

Jiang, H. & Adams, C. (2006) Treatability of chloro-s-triazines by conventional drinking water treatment technologies. *Water Research* **40**(8), 1657–1667.

Jiménez, H. R., Moratal, J. M. & Loock, B. (2002) ^{1}H-NMR spectroscopic studies of paramagnetic superstructured iron(III) porphyrinsThis article is dedicated to the memory of Professor Michel Momenteau of Institut Curie.Abbreviations. 1D and 2D: One-dimensional and two-dimensional; COSY: correlated spectroscopy; NOESY: nuclear Overhauser effect spectroscopy; TPP: 5,10,15,20-tetraphenylporphyrinate dianion. *New Journal of Chemistry* **26**(3), 323–329.

Jones, K. C. & de Voogt, P. (1999) Persistent organic pollutants (POPs): State of the science. *Environmental Pollution* **100**(1–3), 209–221.

Kadish, K., Guilard, R. & Smith, K. M. (2012) *The Porphyrin Handbook: Phthalocyanines: Properties and Materials*. Academic Press, New York, 4-284.

Kamala, D., Geddes, A., Theis, T., Tomkin, J. & OpenStax. (2018) Environmental Biology. In: Fisher, M. R. Eds. *Environmental Biology* (1st), Open Oregon Educational Resources, Oklahoma, 217-225.

Karthikeyan, S. & Lee, J. Y. (2013) Zinc-Porphyrin Based Dyes for Dye-Sensitized Solar Cells. *The Journal of Physical Chemistry A* **117**(42), 10973–10979.

Kessel, D. (2004) Photodynamic therapy: From the beginning. *Photodiagnosis and Photodynamic Therapy* **1**(1), 3–7.

Khan, M. & Cao, W. (2013) Preparation of Y-doped TiO_2 by hydrothermal method and investigation of its visible light photocatalytic activity by the degradation of methylene blue. *Journal of Molecular Catalysis A: Chemical* **376**, 71–77.

Kim, D. (2012) *Multiporphyrin Arrays: Fundamentals and Applications*. CRC Press, USA, 55-83.

Kim, J., Park, Y. & Park, H. (2014) Solar Hydrogen Production Coupled with the Degradation of a Dye Pollutant Using TiO_2 Modified with Platinum and Nafion. *International Journal of Photoenergy* **14**, 1–9.

Kuhn, H. (1949) A Quantum-Mechanical Theory of Light Absorption of Organic Dyes and Similar Compounds. *Journal of Chemical Physics* **17**, 1198–1212.

Kumar, P. P., Premaladha, G. & Maiya, B. G. (2005) Porphyrin-anthraquinone dyads: Synthesis, spectroscopy and photochemistry. *Journal of Chemical Sciences* **117**(2), 193–201.

Kumar, P. R., Britto, N. J., Kathiravan, A., Neels, A., Jaccob, M. & Mothi, E. M. (2019) Synthesis and electronic properties of A_3 B-thienyl porphyrins: Experimental and computational investigations. *New Journal of Chemistry* **43**(3), 1569–1580.

Kumaravel, V., Imam, M., Badreldin, A., Chava, R., Do, J., Kang, M. & Abdel-Wahab, A. (2019) Photocatalytic Hydrogen Production: Role of Sacrificial Reagents on the Activity of Oxide, Carbon, and Sulfide Catalysts. *Catalysts* **9**, 276.

Lanterna, A. E. & Scaiano, J. C. (2017) Photoinduced Hydrogen Fuel Production and Water Decontamination Technologies. Orthogonal Strategies with a Parallel Future? *ACS Energy Letters* **2**(8), 1909–1910.

Lee, C., Yang, W. & Parr, R. G. (1988) Development of the Colle-Salvetti correlation-energy formula into a functional of the electron density. *Physical Review B* **37**(2), 785–789.

Leung, D. Y. C., Fu, X., Wang, C., Ni, M., Leung, M. K. H., Wang, X. & Fu, X. (2010) Hydrogen Production over Titania-Based Photocatalysts. *ChemSusChem* **3**(6), 681–694.

Lewis, N. S. & Nocera, D. G. (2006) Powering the planet: Chemical challenges in solar energy utilization. *Proceedings of the National Academy of Sciences* **103**(43), 15729–15735.

Li, D., Dong, W., Sun, S., Shi, Z. & Feng, S. (2008) Photocatalytic Degradation of Acid Chrome Blue K with Porphyrin-Sensitized TiO_2 under Visible Light. *The Journal of Physical Chemistry C* **112**(38), 14878–14882.

Lindsey, J. S. (1994) The Synthesis of Meso-Substituted Porphyrins. In: Montanari F & Casella, L. Eds. *Metalloporphyrins Catalyzed Oxidations*, Springer Netherlands, 49–86

Lindsey, J. S., Schreiman, I. C., Hsu, H. C., Kearney, P. C. & Marguerettaz, A. M. (1987) Rothemund and Adler-Longo reactions revisited: Synthesis of tetraphenylporphyrins under equilibrium conditions. *The Journal of Organic Chemistry* **52**(5), 827–836.

Liu, Q., Yu, G. & Liu, J. J. (2009) Solar Radiation as Large-Scale Resource for Energy-Short World. *Energy & Environment* **20**(3), 319–329.

Lundqvist, M. J., Nilsing, M., Person, P. & Lunell, S. (2006) DFT study of bare and dye-sensitized TiO_2 clusters and nanocrystals. *International Journal of Quantum Chemistry* **106**(15), 3214–3234.

Mack, J. (2017) Expanded, Contracted, and Isomeric Porphyrins: Theoretical Aspects. *Chemical Reviews* **117**(4), 3444–3478.

Maisch, T. (2015) Resistance in antimicrobial photodynamic inactivation of bacteria. *Photochemical & Photobiological Sciences* **14**(8), 1518–1526.

Maiti, N. C. & Ravikanth, M. (1996) Effects of non-planarity and β-substitution on the singlet-excited-state properties of basket-handle porphyrins. *Journal of the Chemical Society, Faraday Transactions* **92**(7), 1095–1100.

Managa, M., Britton, J., Amuhaya, E. K. & Nyokong, T. (2017a) Photophysical properties of GaCl 5,10,15,20-tetra(1-pyrenyl)porphyrinato incorporated into Pluronic F127 micelle. *Journal of Luminescence* **185**, 34–41.

Managa, M., Ngoy, B. P., Mafukidze, D., Britton, J. & Nyokong, T. (2017b) Photophysical studies of meso-tetrakis(4-nitrophenyl) and meso-tetrakis(4-sulfophenyl) gallium porphyrins loaded into Pluronic F127 polymeric micelles. *Journal of Photochemistry and Photobiology A: Chemistry* **348**, 179–187.

Marsh, D. F., Falvo, R. E. & Mink, L. M. (1999) Microscale Synthesis and 1H NMR Analysis of Tetraphenylporphyrins. *Journal of Chemical Education* **76**(2), 237.

Michl, J. (1984) Tetrahedron **40**(19), 3845-3934.

Miranda-García, N., Suárez, S., Sánchez, B., Coronado, J. M., Malato, S. & Maldonado, M. I. (2011) Photocatalytic degradation of emerging contaminants in municipal wastewater treatment plant effluents using immobilized TiO_2 in a solar pilot plant. *Applied Catalysis B: Environmental* **103**(3), 294–301.

Moore, M. R. (2009) An Historical Introduction to Porphyrin and Chlorophyll Synthesis. In: Warren, M. J. & Smith, A. G. Eds. *Tetrapyrroles: Birth, Life and Death*. Springer New York, 1–28.

Muszkat, L., Feigelson, L., Bir, L. & Muszkat, K. A. (2002) Photocatalytic degradation of pesticides and bio-molecules in water. *Pest Management Science* **58**(11), 1143–1148.

Nemykin, V. N. & Hadt, R. G. (2010) Interpretation of the UV−vis Spectra of the *meso* (Ferrocenyl)-Containing Porphyrins using a TDDFT Approach: Is Gouterman's Classic Four-Orbital Model Still in Play? *The Journal of PhysicaNilsingl Chemistry A* **114**(45), 12062–12066.

Ni, M., Leung, M. K. H., Leung, D. Y. C. & Sumathy, K. (2007) A review and recent developments in photocatalytic water-splitting using TiO2 for hydrogen production. *Renewable and Sustainable Energy Reviews* **11**(3), 401–425.

Novotny, V. (1994) *Water Quality: Prevention, Identification and Management of Diffuse Pollution*. Van Nostrand-Reinhold Publishers, California, 236-342.

Nyarko, E., Hanada, N., Habib, A. & Tabata, M. (2004) Fluorescence and phosphorescence spectra of Au(III), Pt(II) and Pd(II) porphyrins with DNA at room temperature. *Inorganica Chimica Acta* **357**(3), 739–745.

Ojadi, E. C. A., Linschitz, H., Gouterman, M., Walter, R. I., Lindsey, J. S., Wagner, R. W., Droupadi, P. R. & Wang, W. (1993) Sequential protonation of meso-[p-(dimethylamino)phenyl]porphyrins: Charge-transfer excited states producing hyperporphyrins. *The Journal of Physical Chemistry* **97**(50), 13192–13197.

Oller, I., Malato, S. & Sánchez-Pérez, J. A. (2011) Combination of Advanced Oxidation Processes and biological treatments for wastewater decontamination–A review. *Science of The Total Environment* **409**(20), 4141–4166.

Paredes-Gil, K., Mendizabal, F., Páez-Hernández, D. & Arratia-Pérez, R. (2017) Electronic structure and optical properties calculation of Zn-porphyrin with N-annulated perylene adsorbed on TiO$_2$ model for dye-sensitized solar cell applications: A DFT/TD-DFT study. *Computational Materials Science* **126**, 514–527.

Perera, F. (2017) Pollution from Fossil-Fuel Combustion is the Leading Environmental Threat to Global Pediatric Health and Equity: Solutions Exist. *International Journal of Environmental Research and Public Health* **15**(1), 16.

Polo, A. S., Itokazu, M. K. & Murakami Iha, N. Y. (2004) Metal complex sensitizers in dye-sensitized solar cells. *Coordination Chemistry Reviews* **248**(13), 1343–1361.

Rafiee, A. & Khalilpour, K. R. (2019) *Renewable Hybridization of Oil and Gas Supply Chains*. Elsevier Scientific Publishing Company, Washington, 331–372.

Rahimi, R., Zargari, S., Yousefi, A., Berijani, M., Ghaffarinejad, A. & Morsali, A. (2015) Visible light photocatalytic disinfection of E. coli with TiO_2–graphene nanocomposite sensitized with tetrakis(4-carboxyphenyl)porphyrin. *Applied Surface Science* **355**, 1098–1106.

Rahman, M., Tian, H. & Edvinsson, T., (2020) Revisiting the Limiting Factors for Overall Water-Splitting on Organic Photocatalysts. *Angewandte Chemie* **59**, 2-18.

Ravindra, P. K., Dougherty, T. & Kessel, D. (2016) *Handbook of Photodynamic Therapy: Updates On Recent Applications of Porphyrin-based Compounds*. World Scientific, London, 45-95.

Rogers, P. P., Llamas, M. R., Cortina, L. M., Llamas, M. R. & Cortina, L. M. (2005) *Water Crisis: Myth or Reality?* Taylor& Francis, Leiden, 3-37.

Rosegrant, M. W., Cai, X. & Cline, S. A. (2002) *World Water and Food to 2025: Dealing with Scarcity*. International Food Policy Research Institute, Washington, 17-22.

Rothemund, P. (1936) A New Porphyrin Synthesis:The Synthesis of Porphine. *Journal of the American Chemical Society* **58**(4), 625–627.

Rotomskis, R., Streckyte, G. & Bagdonas, S. (1997) Phototransformations of sensitizers to Photoproducts formed in aqueous solutions of porphyrins. *Journal of Photochemistry and Photobiology B: Biology* **39**(2), 172–175.

Saenz, C., Ethirajan, M., Iacobucci, G., Pandey, A., Missert, J. R., Dobhal, M. P. & Pandey, R. K. (2011) Indium as a central metal enhances the photosensitizing efficacy of benzoporphyrin complexes. *Journal of Porphyrins and Phthalocyanines* **15**(11–12), 1310–1316.

Salameh, M. G. (2003) Can renewable and unconventional energy sources bridge the global energy gap in the 21st century? *Applied Energy* **75**(1–2), 33–42.

Santhanamoorthi, N., Lo, C.M. & Jiang, J.C. (2013) Molecular Design of Porphyrins for Dye-Sensitized Solar Cells: A DFT/TDDFT Study. *The Journal of Physical Chemistry Letters* **4**(3), 524–530.

Schneider, J. & Bahnemann, D. W. (2013) Undesired Role of Sacrificial Reagents in Photocatalysis. *The Journal of Physical Chemistry Letters* **4**(20), 3479–3483.

Schultz, D.M. & Yoon, T.P. (2014) Solar Synthesis: Prospects in Visible Light Photocatalysis. *Science* **343**, 1239176–1239176.

Sen, P., Hirel, C., Andraud, C., Aronica, C., Bretonniere, Y., Mohammed, A., Ågren, H., Minaev, B., Minaeva, V., Baryshnikov, G., Lee, H.-H., Duboisset, J. & Lindgren, M. (2010) Fluorescence and FTIR Spectra Analysis of Trans-A(2) B(2)-Substituted Di- and Tetra-Phenyl Porphyrins. *Materials* **3**(8), 4446–4475.

Şen, Z. (2004) Solar energy in progress and future research trends. *Progress in Energy and Combustion Science* **30**(4), 367–416.

Senarathna, L., Fernando, N., Gunasekara, D., Weerasekera, M., Hewageegana, P., Arachchi, N., Siriwardena, D. & Jayaweera, M. (2017) Enhanced antibacterial activity of TiO_2 nanoparticle surface modified with Garcinia zeylanica extract. *Chemistry Central Journal* **11,** 7.

Sessler, J. L. & Burrell, A. K. (1992) Expanded porphyrins. In: *Macrocycles*. Springer, Berlin Heidelberg, 177–273.

Sharma, S. K. & Sanghi, R. (Eds.). (2012) *Advances in water treatment and pollution prevention*. Springer, Berlin Heidelberg, 201-213.

Shi, K., Song, N., Zou, Y., Zhu, S., Tan, H., Tian, Y., Zhang, B., Yao, H. & Guan, S. (2019) Porphyrin-based porous polyimides: Synthesis, porous structure, carbon dioxide adsorption. *Polymer* **169**, 160–166.

Simpson, W. T. (1949) On the Theory of the π-Electron System in Porphines. *The Journal of Chemical Physics* **17**(12), 1218–1221.

Skovsen, E., Snyder, J. W., Lambert, J. D. C. & Ogilby, P. R. (2005) Lifetime and Diffusion of Singlet Oxygen in a Cell. *The Journal of Physical Chemistry B* **109**(18), 8570–8573.

Smith, K. M. (Eds.). (1975) *Porphyrins and metalloporphyrins*. Elsevier Scientific Publishing Company, Washington, 271-324.

Soy, R. C., Babu, B., Oluwole, D. O., Nwaji, N., Oyim, J., Amuhaya, E., Prinsloo, E., Mack, J. & Nyokong, T. (2019) Photophysicochemical properties and photodynamic therapy activity of chloroindium(III) tetraarylporphyrins and their gold nanoparticle complexes. *Journal of Porphyrins and Phthalocyanines* **23**(12), 34–45.

Stackelberg, P. E., Gibs, J., Furlong, T., Meyer, T., Zaugg, S. & Lippincott, R. (2007) Efficiency of conventional drinking-water-treatment processes in removal of pharmaceuticals and other organic compounds. *Science of The Total Environment* **377**(2), 255–272.

Subramaniam, M., Whitlock, D. & Williford, B. (2012) Water crisis. In: *The Wiley-Blackwell Encyclopedia of Globalization*. Wiley, London, 2403-2456.

Sun, W., Li, J., Yao, G., Jiang, M. & Zhang, F. (2011) Efficient photo-degradation of 4-nitrophenol by using new CuPp-TiO$_2$ photocatalyst under visible light irradiation. *Catalysis Communications* **16**(1), 90–93.

Sykes, G. & Skinner, A. (2015) *Microbial Aspects of Pollution*. Academic Press, London, 11-56.

Taicheng, A., Chen, J., Li, G., Ding, X., Sheng, G., Fu, J., Mai, B. & O'Shea, K. E. (2008) Characterization and the photocatalytic activity of TiO$_2$ immobilized hydrophobic montmorillonite photocatalysts. *Catalysis Today* **139**(1–2), 69–76.

Tang, G., Abas, A. & Wang, S. (2018) Photocatalytic Degradation and Hydrogen Production of TiO$_2$ /Carbon Fiber Composite Using Bast as a Carbon Fiber Source. *International Journal of Photoenergy* **20**, 1–8.

Teh, C. M. & Mohamed, A. R. (2011) Roles of titanium dioxide and ion-doped titanium dioxide on photocatalytic degradation of organic pollutants (phenolic compounds and dyes) in aqueous solutions: A review. *Journal of Alloys and Compounds* **509**(5), 1648–1660.

Teichmann, D., Arlt, W., Wasserscheid, P. & Freymann, R. (2011) A future energy supply based on Liquid Organic Hydrogen Carriers (LOHC). *Energy & Environmental Science* **4**(8), 2767.

Toze, S. (2006) Reuse of effluent water–Benefits and risks. *Agricultural Water Management* **80**(1–3), 147–159.

Viswanath, R. P. (2004) A patent for generation of electrolytic hydrogen by a cost effective and cheaper route. *International Journal of Hydrogen Energy* **29**, 1191–1194.

Vörösmarty, C. J., Green, P., Salisbury, J. & Lammers, R. B. (2000) Global Water Resources: Vulnerability from Climate Change and Population Growth. *Science* **289**(5477), 284–288.

Wang, C., Li, J., Mele, G., Duan, M., Lü, X., Palmisano, L., Vasapollo, G. & Zhang, F. (2010) The photocatalytic activity of novel, substituted porphyrin/TiO$_2$-based composites. *Dyes and Pigments* **84**(2), 183–189.

Wei, X., Du, X., Chen, D. & Chen, Z. (2006) Thermal analysis study of 5,10,15,20-tetrakis (methoxyphenyl) porphyrins and their nickel complexes. *Thermochimica Acta* **440**(2), 181–187.

Winter, C.J. & Nitsch, J. (2012) *Hydrogen as an Energy Carrier: Technologies, Systems, Economy*. Springer Science & Business Media, Berlin, 13-48.

With, T. K. (1980) A short history of porphyrins and the porphyrias. *International Journal of Biochemistry* **11**(3), 189–200.

World Water Development Report (2019) *UN-Water*. https://www.unwater.org/publications/world-water-development-report-2019/ *Accessed on 9th September, 2019*

Wright, J., Gundry, S. & Conroy, R. (2004) Household drinking water in developing countries: A systematic review of microbiological contamination between source and point-of-use. *Tropical Medicine and International Health* **9**(1), 106–117.

Xu, A.W., Gao, Y. & Liu, H.Q. (2002) The Preparation, Characterization, and their Photocatalytic Activities of Rare-Earth-Doped TiO_2 Nanoparticles. *Journal of Catalysis* **207**(2), 151–157.

Yadav, L. S. R., Manjunath, K., Kavitha, C. & Nagaraju, G. (2018) An investigation of hydrogen generation and antibacterial activity of TiO_2 nanoparticles synthesized by the ionic liquid aided ionothermal method. *Journal of Science: Advanced Materials and Devices* **3**(2), 181–187.

Yaron, P. (2010) Application of TiO_2 photocatalysis for air treatment: Patents' overview. *Applied Catalysis B: Environmental* **99**, 448–460.

Zakavi, S. & Hoseini, S. (2015) The absorption and fluorescence emission spectra of meso-tetra(aryl)porphyrin dications with weak and strong carboxylic acids: A comparative study. *RSC Advances* **5**(129), 106774–106786.

Zhang, J., Pan, M., Luo, C., Chen, X., Kong, J. & Zhou, T. (2016) A novel composite paint (TiO_2/fluorinated acrylic nanocomposite) for antifouling application in marine environments. *Journal of Environmental Chemical Engineering* **4**, 2545–2555.

Zhou, Y., Tang, L., Zeng, G., Chen, J., Cai, Y., Zhang, Y., Yang, G., Liu, Y., Zhang, C. & Tang, W. (2014) Mesoporous carbon nitride based biosensor for highly sensitive and selective analysis of phenol and catechol in compost bioremediation. *Biosensors and Bioelectronics* **61**, 519–525.

APPENDIX A: CHARACTERIZATION OF PP1
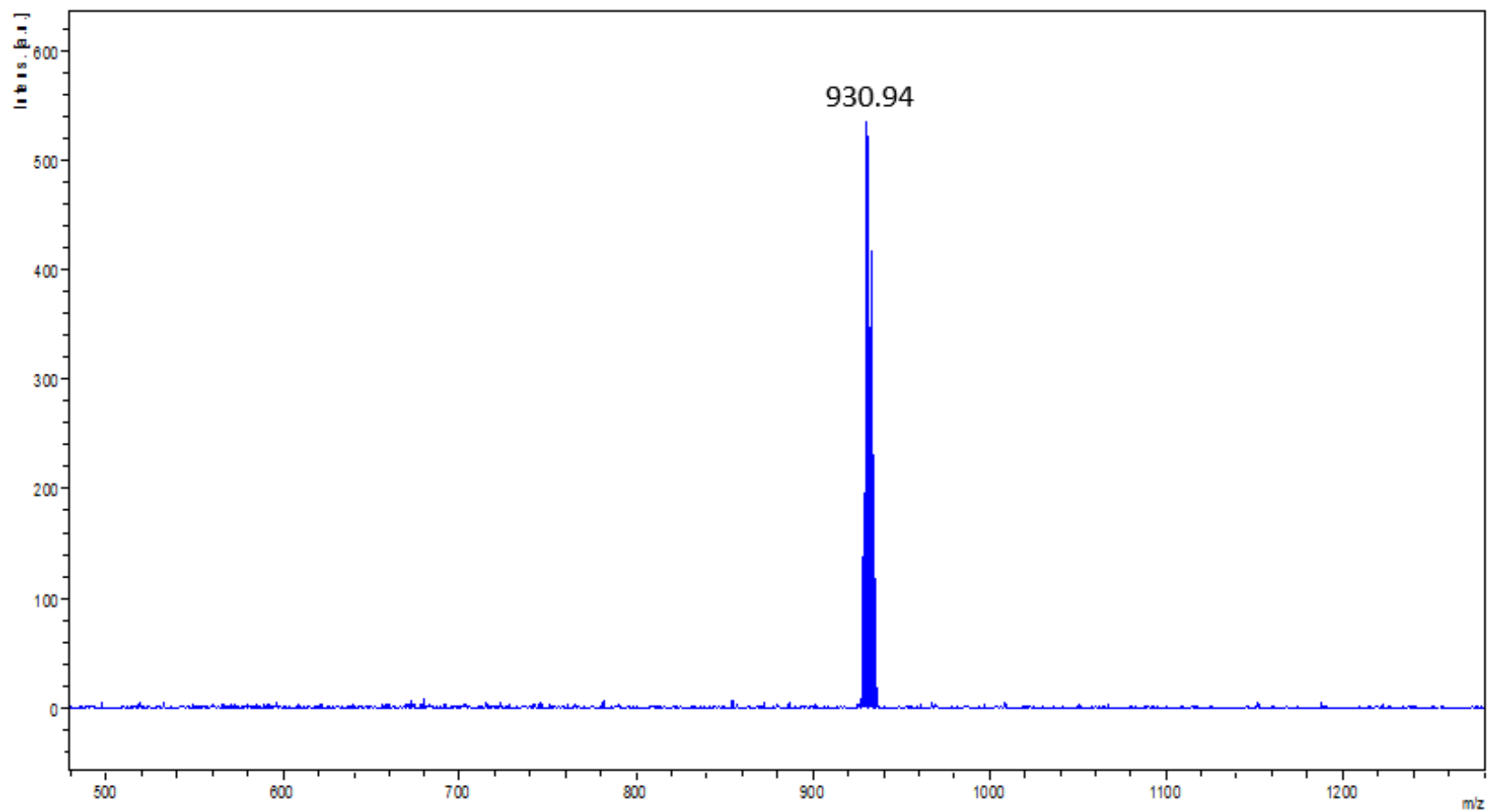
Figure A1: Mass spectrum for PP1. The *m/z* peak lies at 930.94
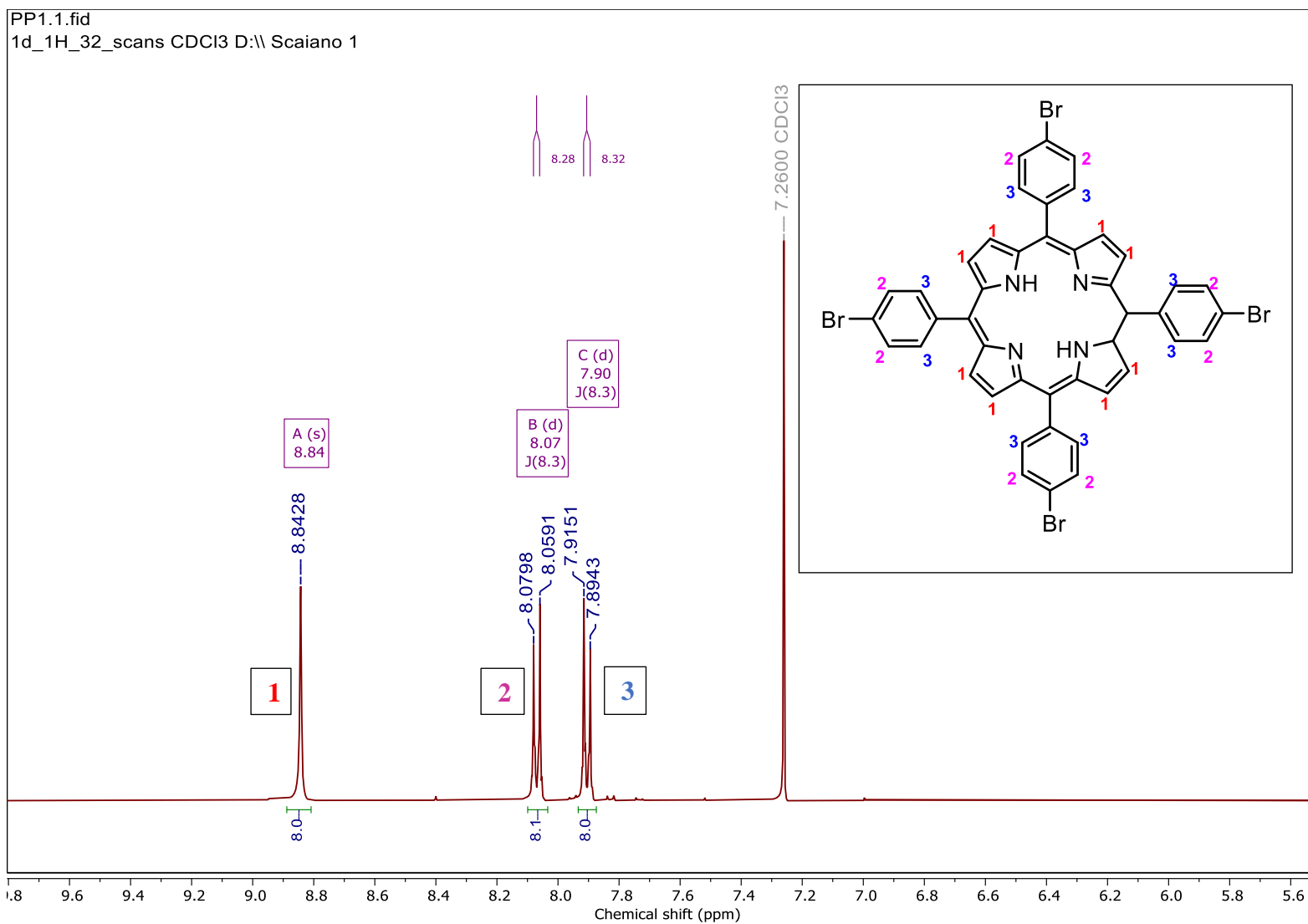
Figure A2: NMR spectrum for PP1
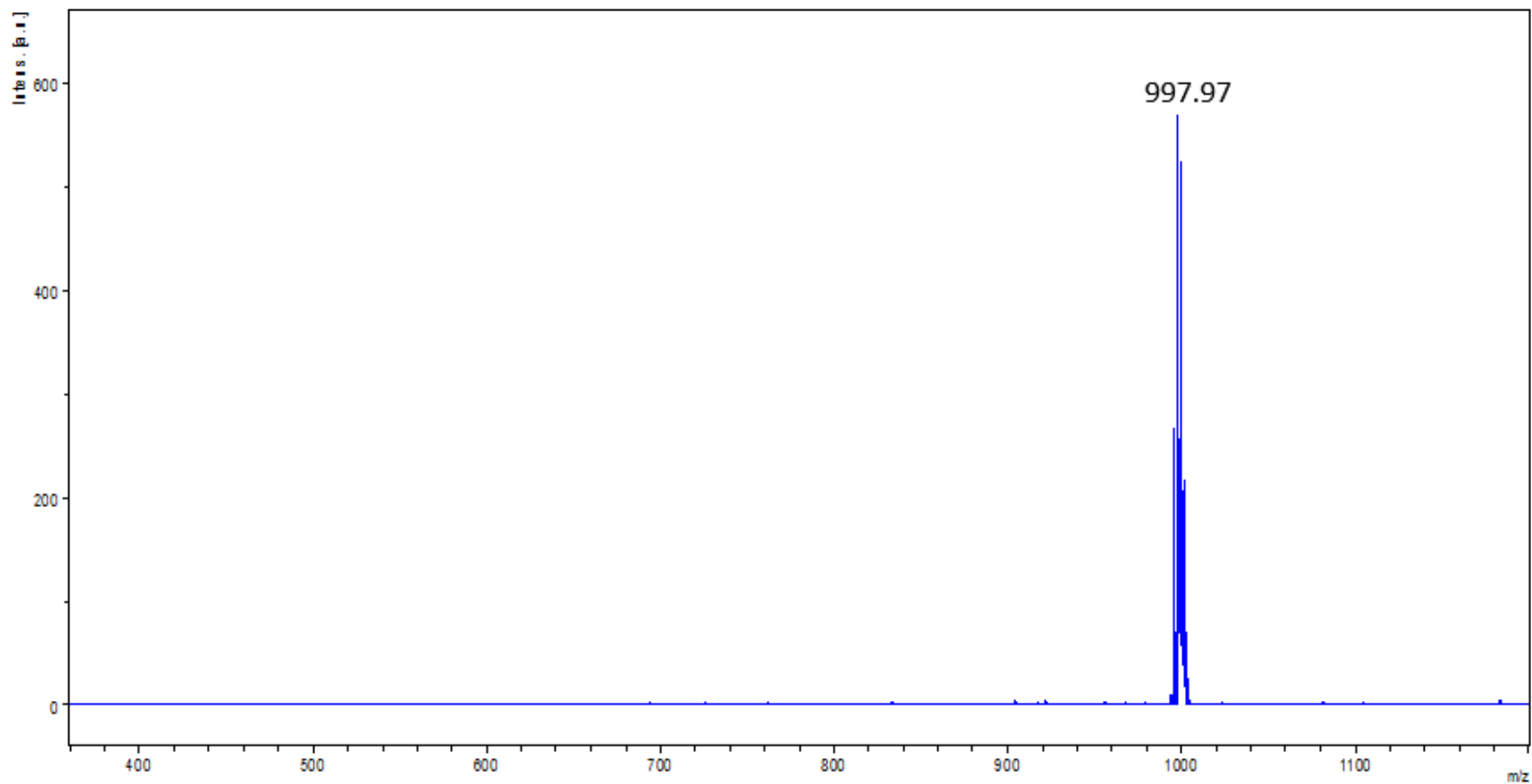
Figure B1: Mass spectrum for GaPP1. The *m/z* peak lies at 997.97
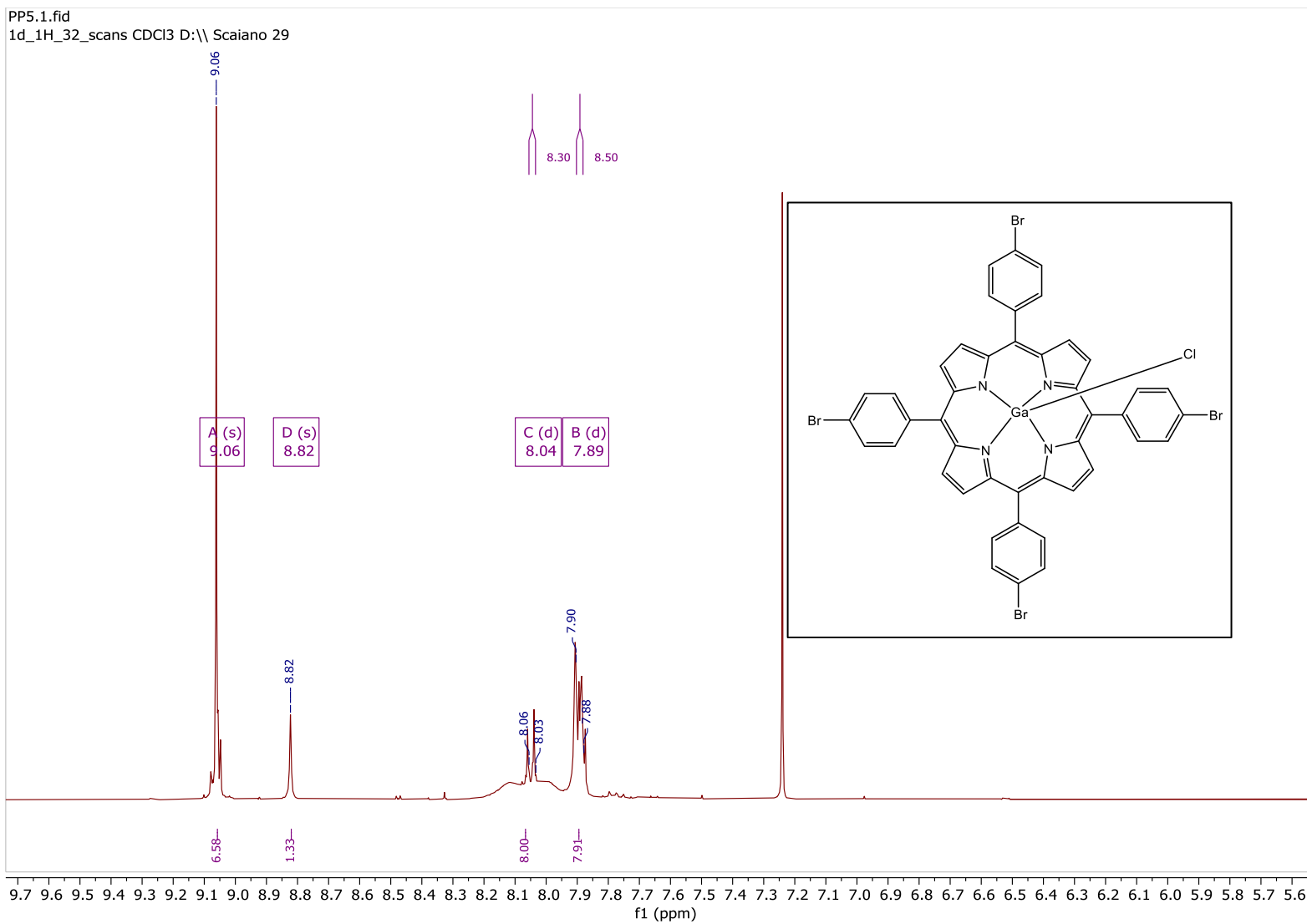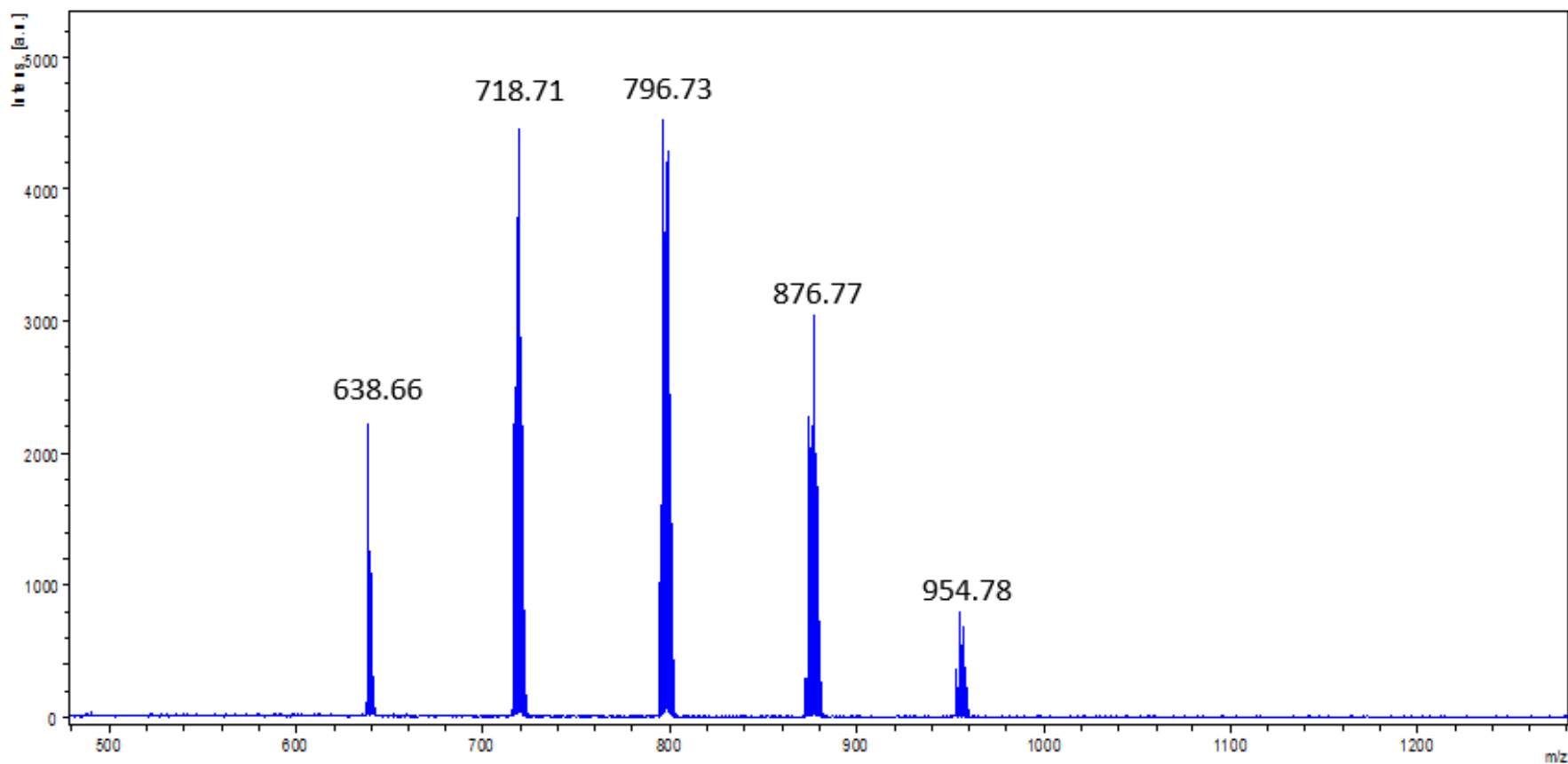
Figure B2: NMR spectrum for GaPP1
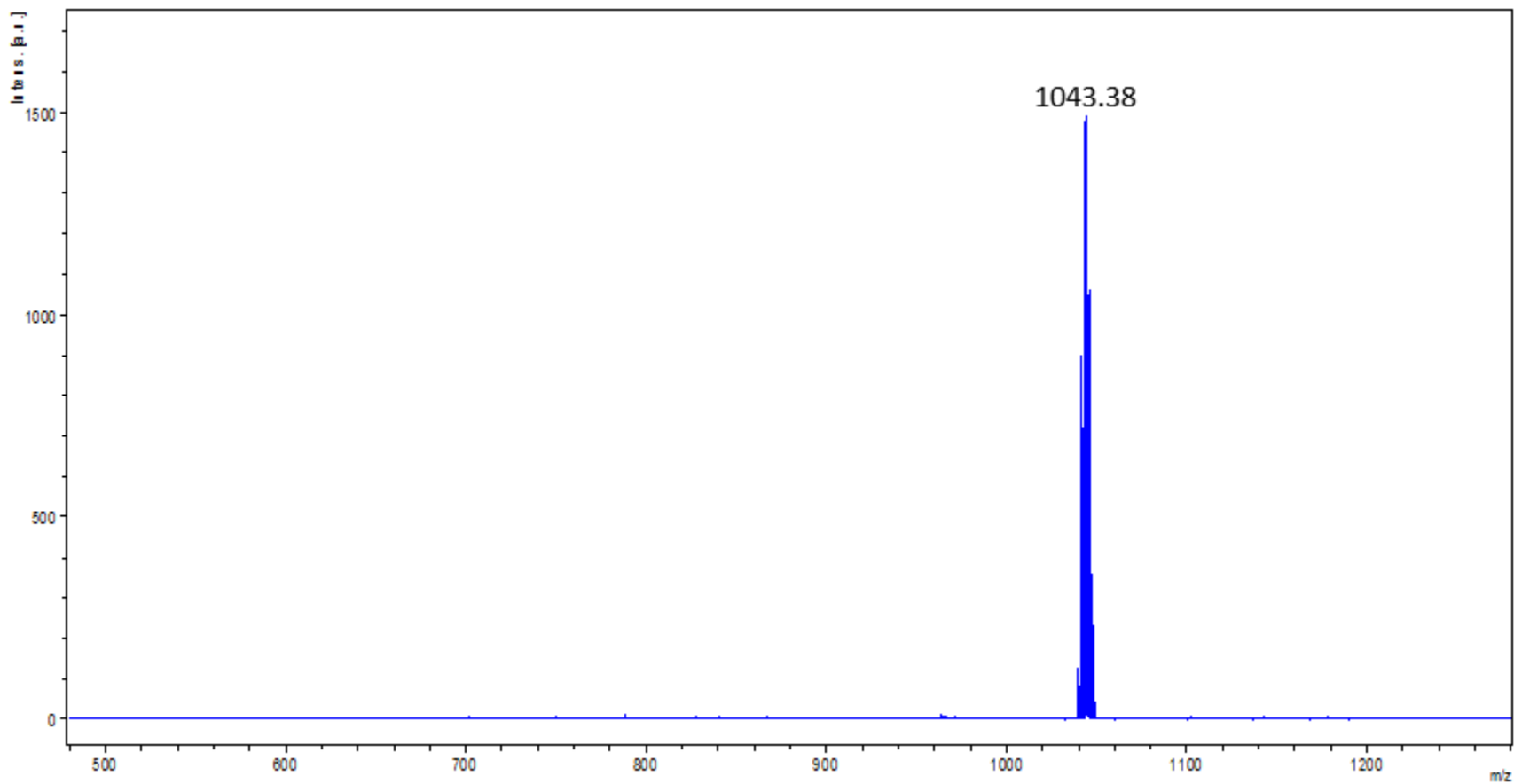
Figure C1: Mass spectrum for InPP1. The *m/z* peaks lie at 1043.38
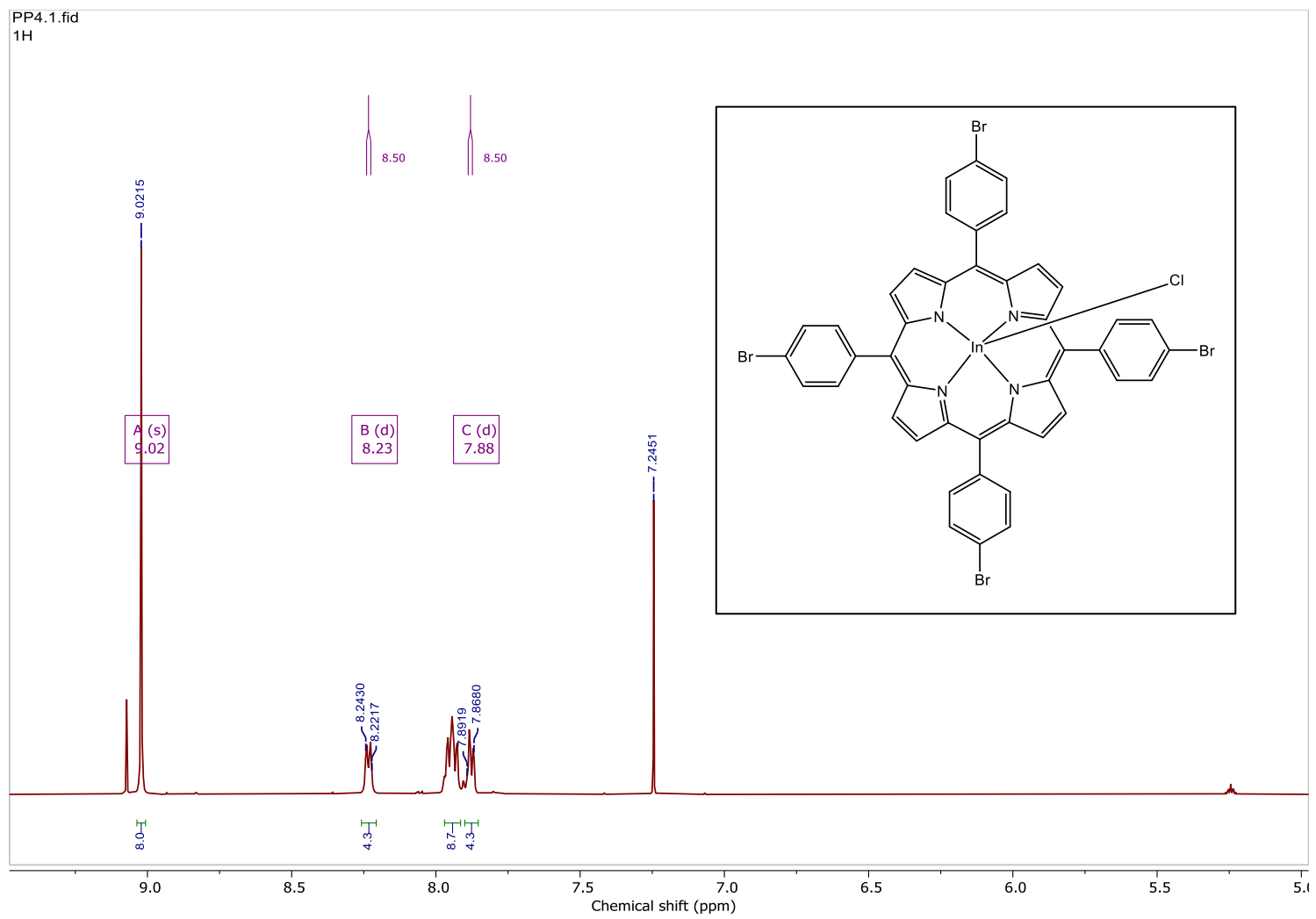
Figure C2: NMR spectrum for InPP1
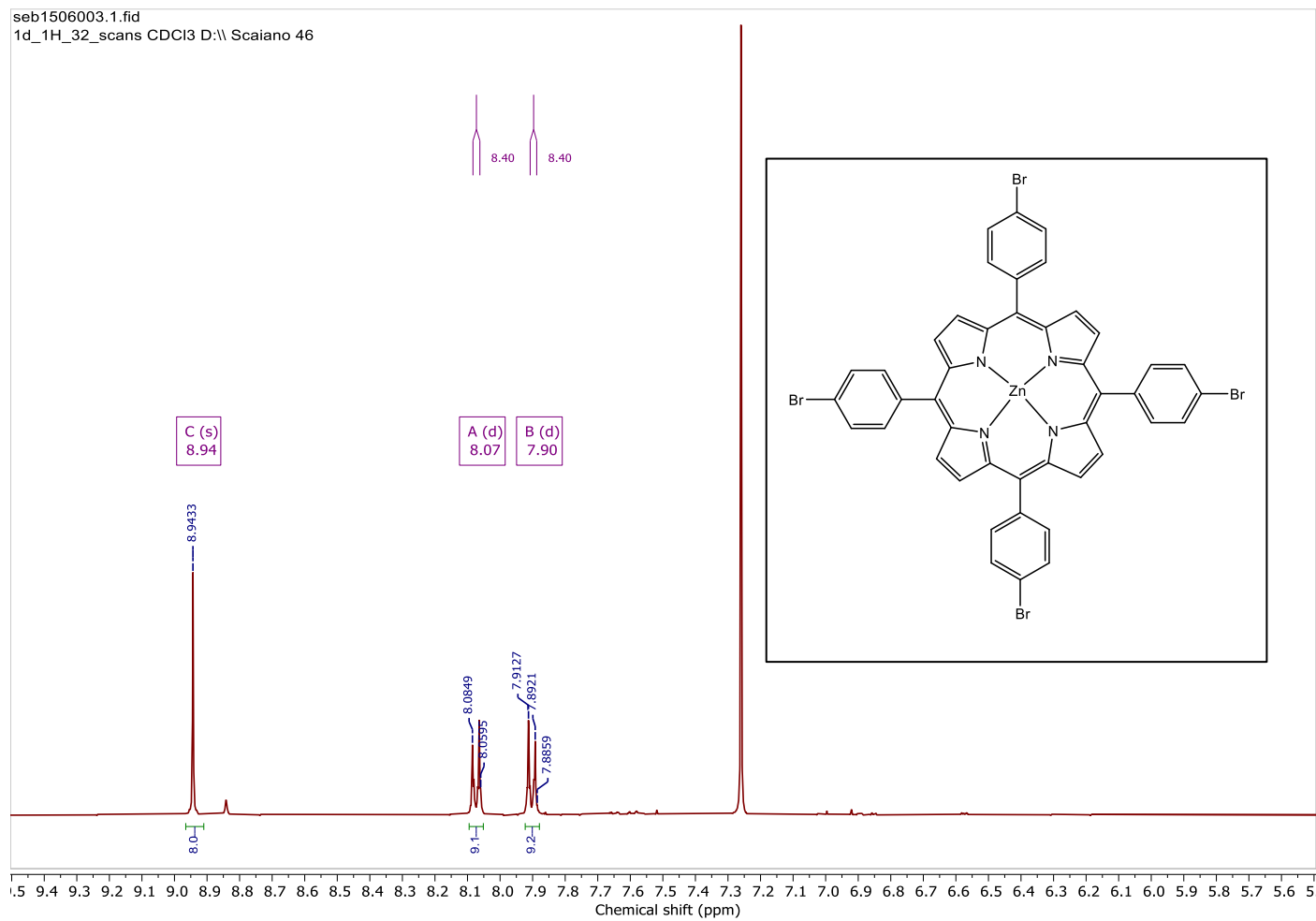
Figure D1: NMR spectrum for ZnPP1

Figure E1: Mass spectrum for PP2. The *m/z* peaks lie at 638.66, 718.71, 796.73, 876.77, 954.78
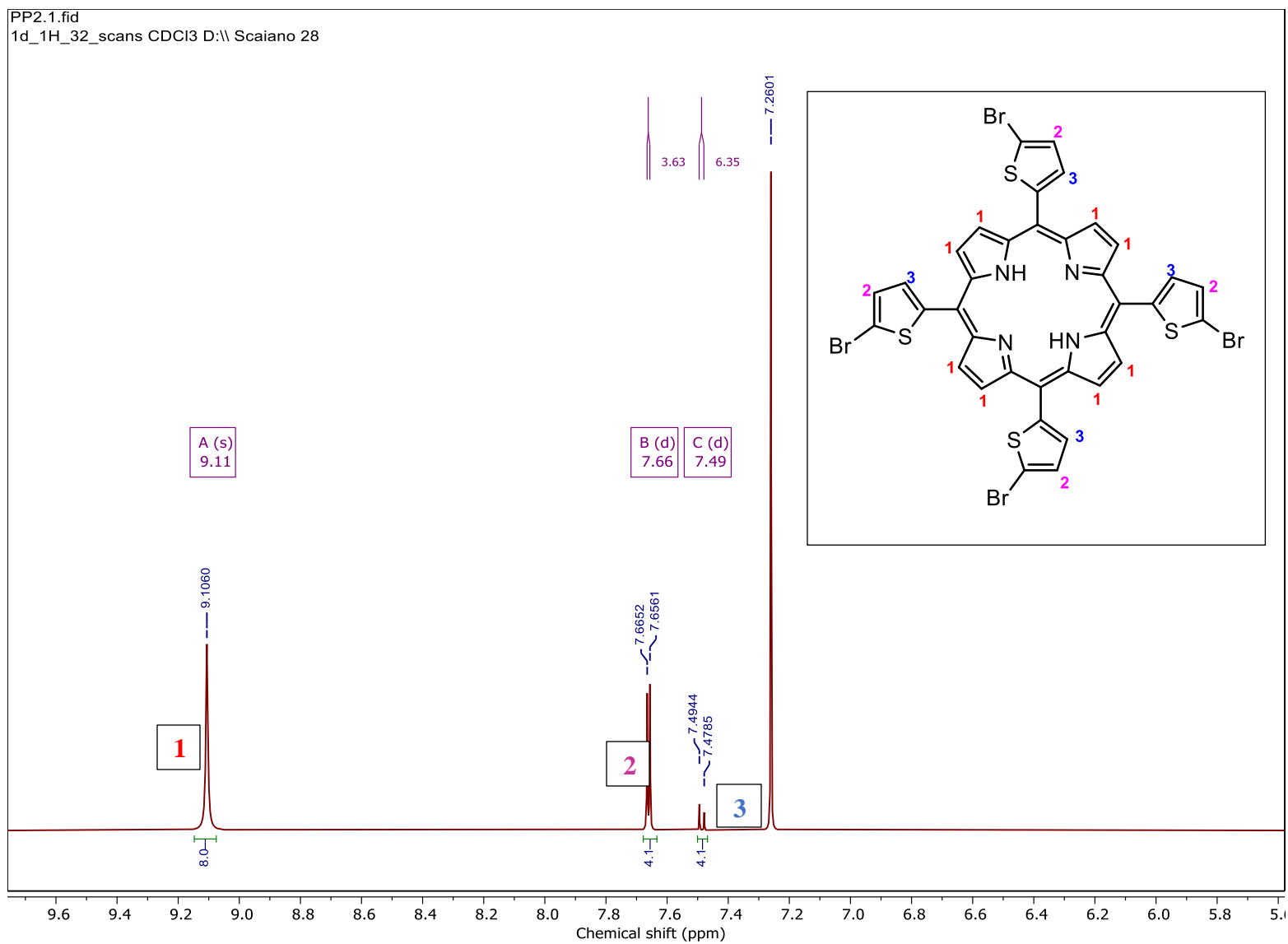
Figure E2: NMR spectrum for PP2
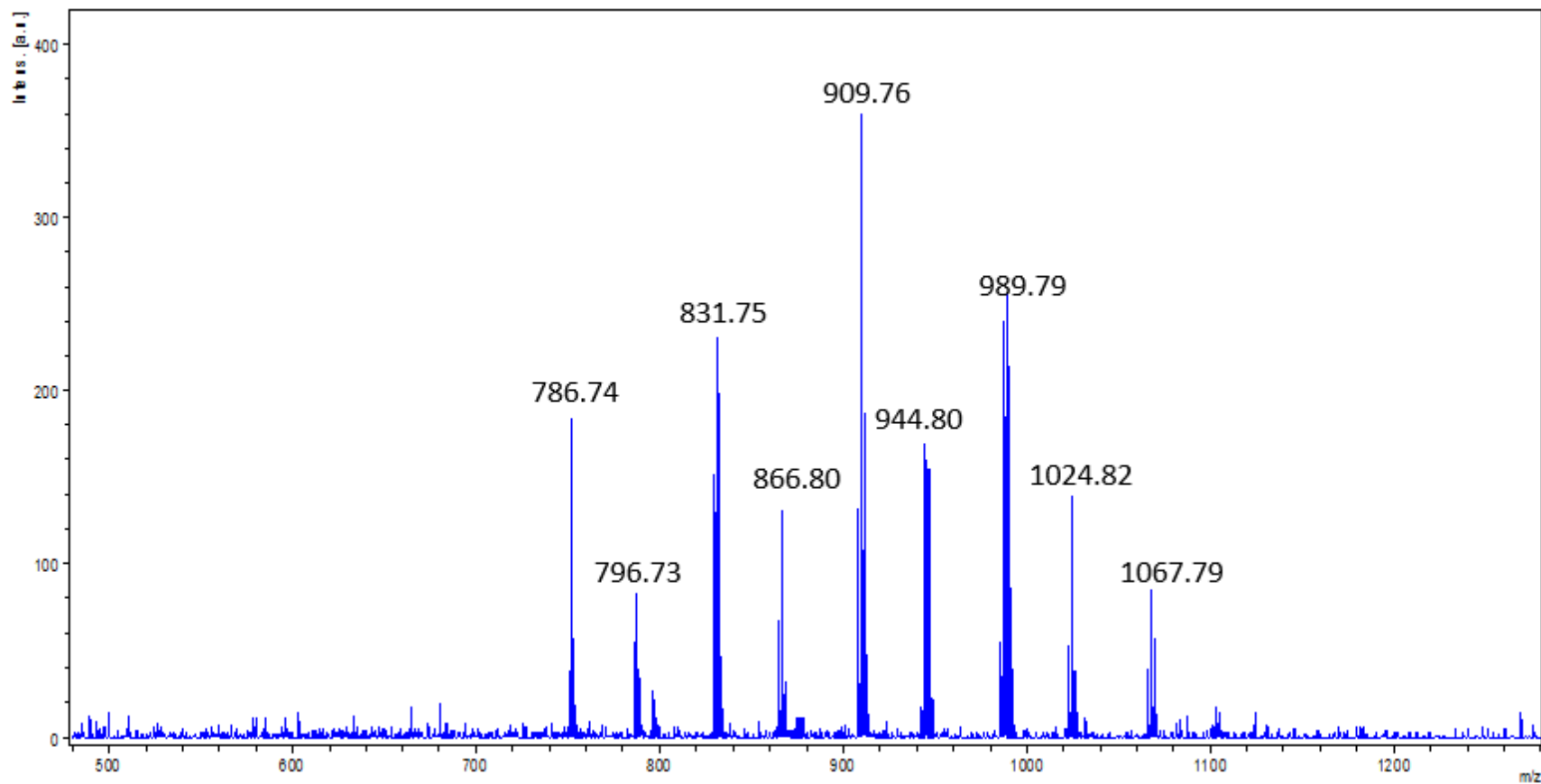
Figure F1: Mass spectrum for InPP2. The *m/z* peaks lie at 786.74, 796.73, 831.75, 866.80, 909.76, 944.80, 989.79, 1024.82, 1067.79
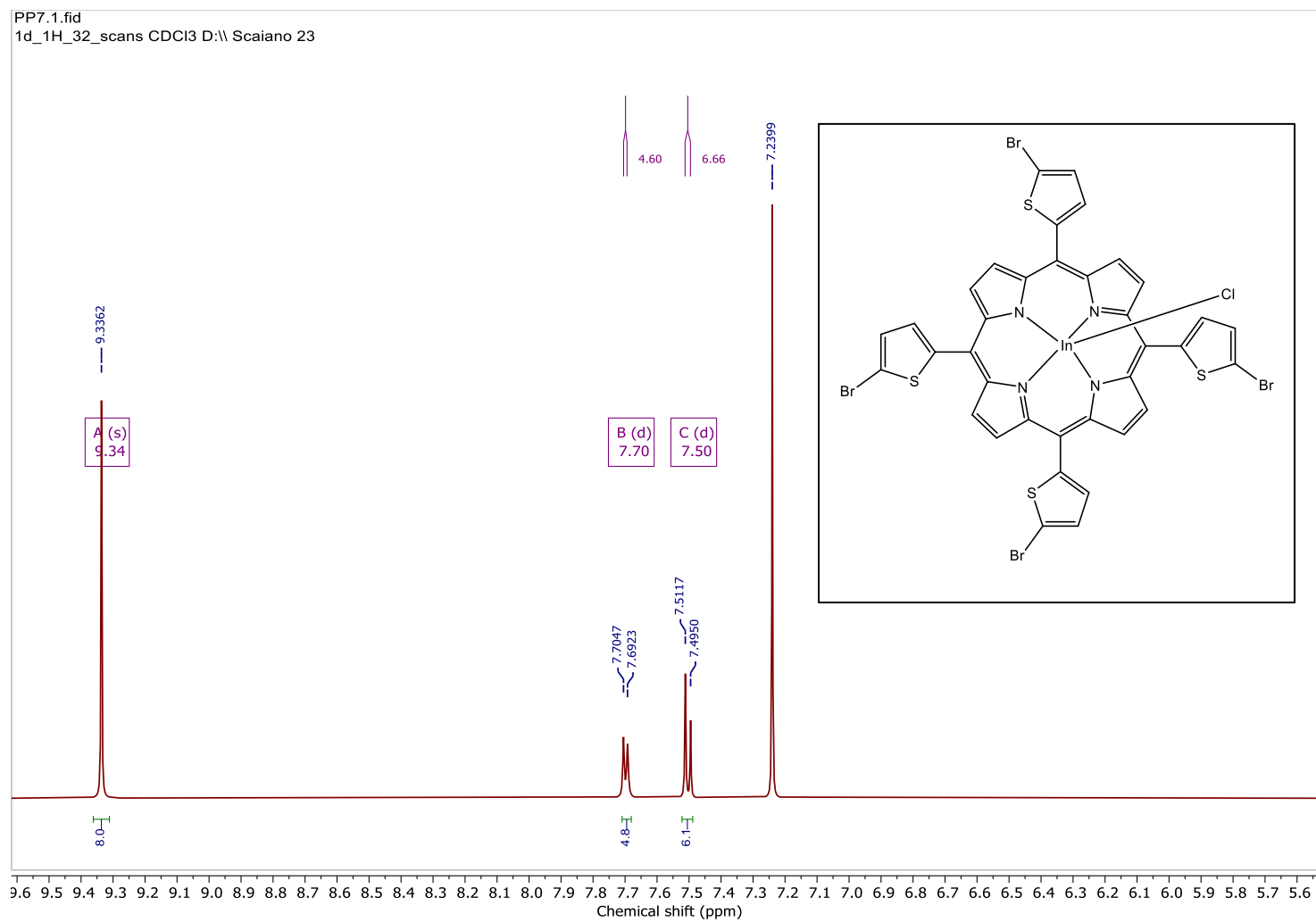
Figure F2: NMR spectrum for InPP2

APPENDIX G: CHARACTERIZATION OF GaPP2
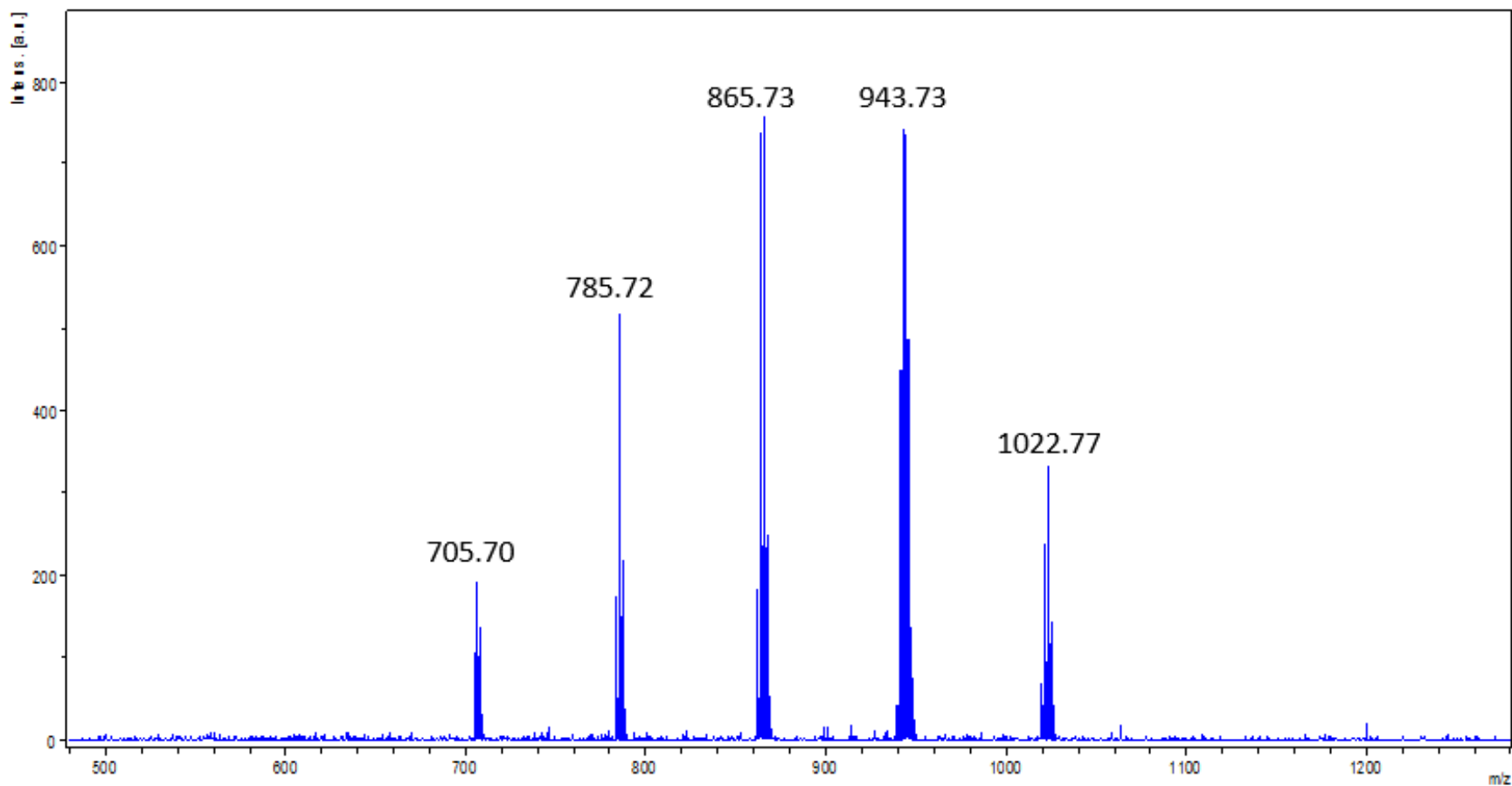
Figure G1: Mass spectrum for GaPP2. The *m/z* peaks lie at 705.70, 785.72, 865.73, 943.73, 1022.77
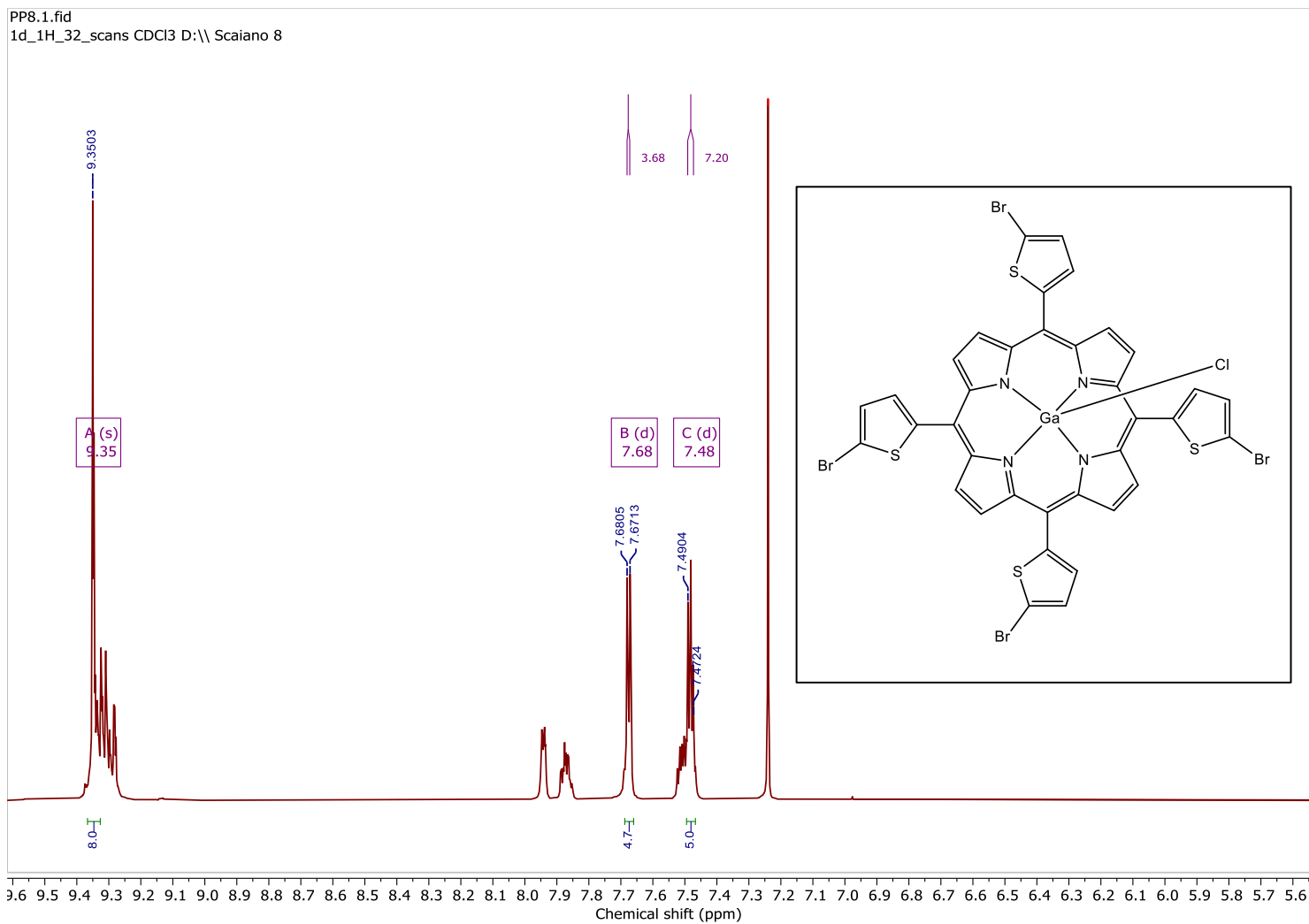
Figure G2: NMR spectrum for GaPP2
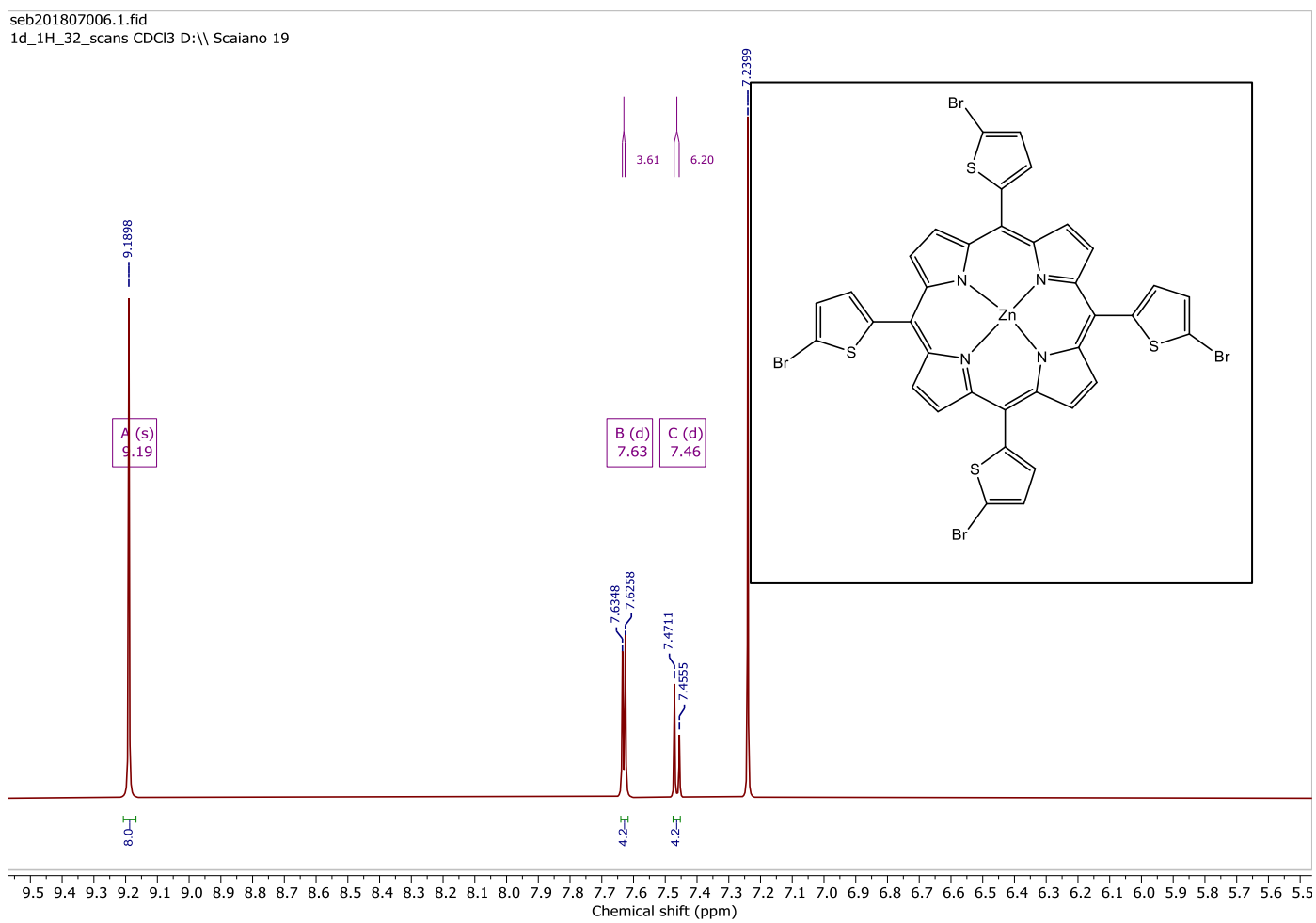
Figure H1: NMR spectrum for ZnPP2
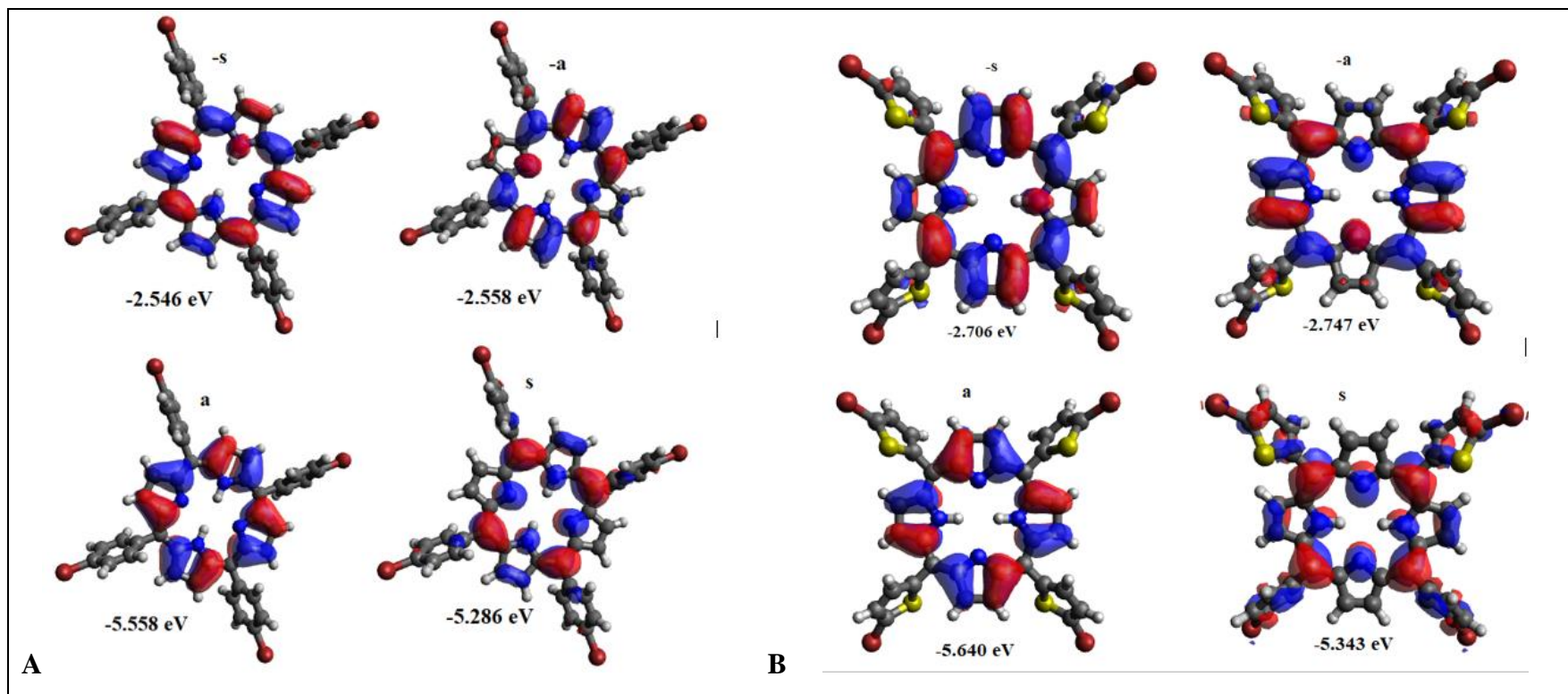
Figure I1: Optimized Geometry of Frontier molecular orbitals for PP1(A) and PP2 (B)
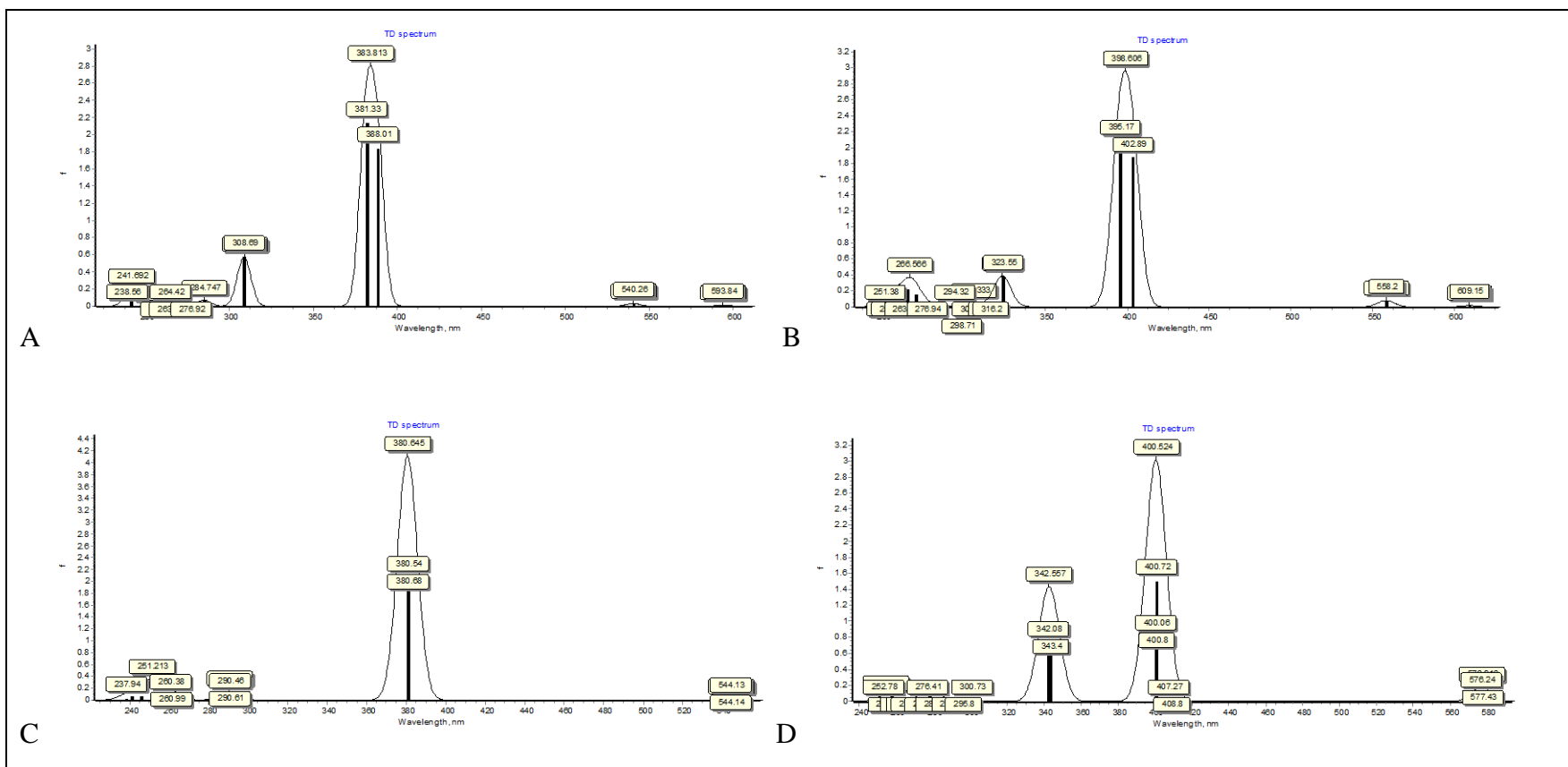
Figure I2: Calculated TD-DFT electronic spectra for PP1 (A), PP2 (B), ZnPP1 (C) and InPP1 (D)
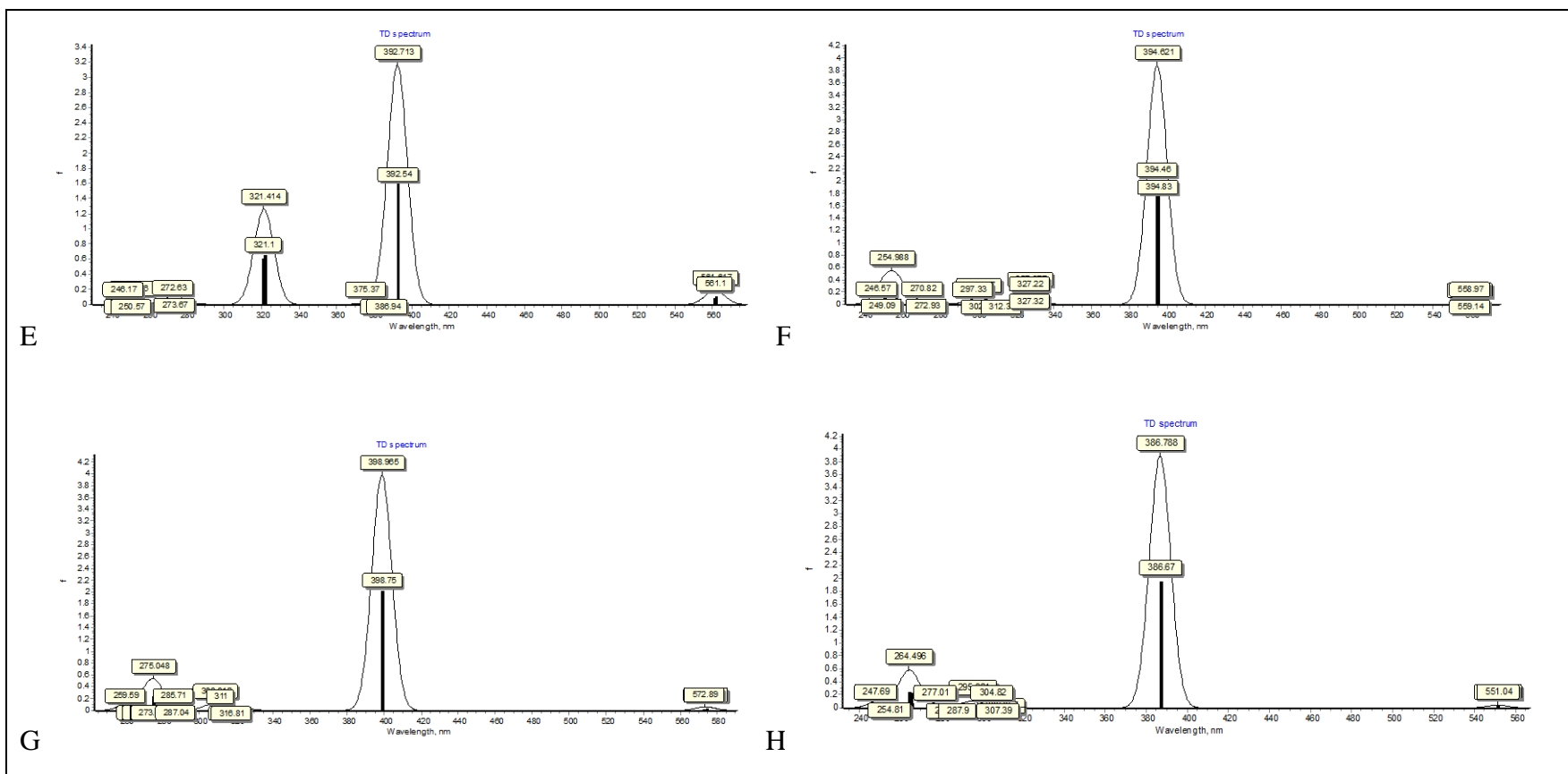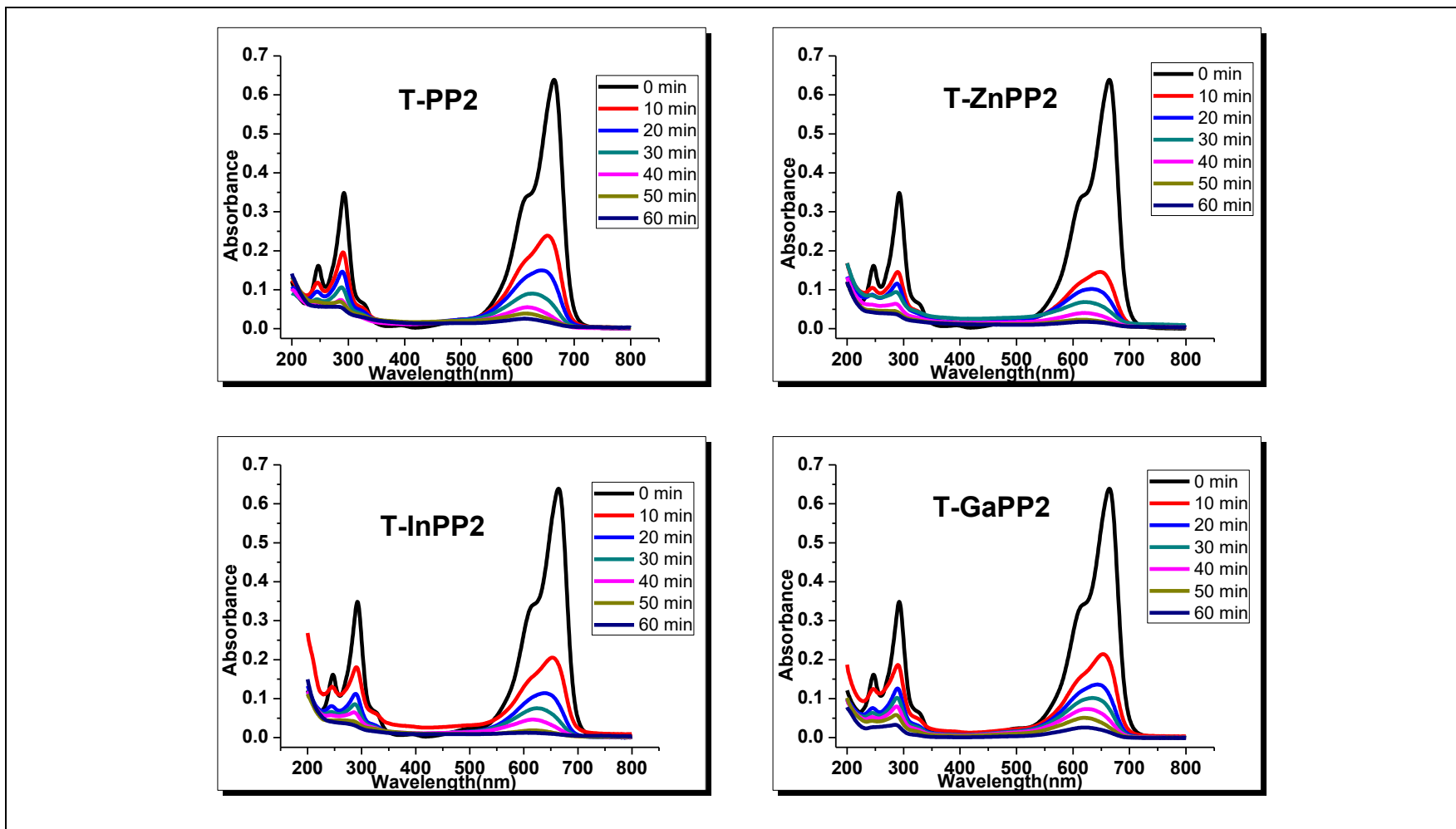
Figure I2: Calculated TD-DFT electronic spectra for GaPP1 (E), ZnPP2 (F), InPP2 (G) and GaPP2 (H)

APPENDIX J: DEGRADATION PROFILE FOR THE PHOTOCATALYSTS
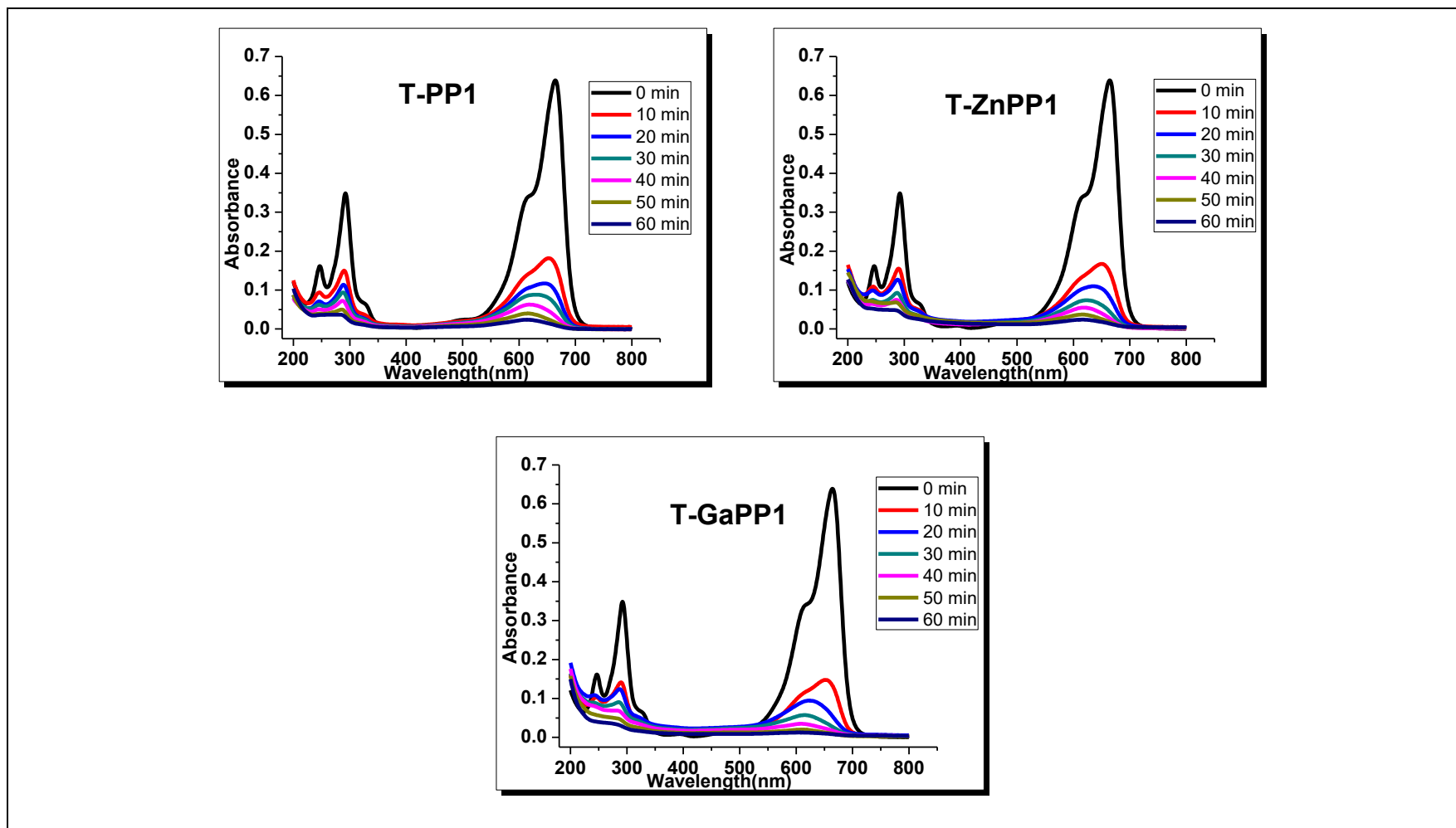
**Figure J1**: Degradation profile for PP1 and its complexes

**Figure J2**: Degradation profile for PP2 and its complexes

APPENDIX K: HYDROGEN GENERATION DATA

Photocatalyst	Hydrogen Production (mmol/g/h)
PP1-TiO_2	0.043 ± 0.001
ZnPP1-TiO_2	0.013 ± 0.002
InPP1-TiO_2	0.005 ± 0.001
GaPP1-TiO_2	0.018 ± 0.002
PP2-TiO_2	0.032 ± 0.002
ZnPP2-TiO_2	0.018 ± 0.002
InPP2-TiO_2	0.016 ± 0.003
GaPP2-TiO_2	0.027 ± 0.001
TiO_2	0.022 ± 0.003

APPENDIX L: LINEAR REGRESSION FIT FOR MB DEGRADATION
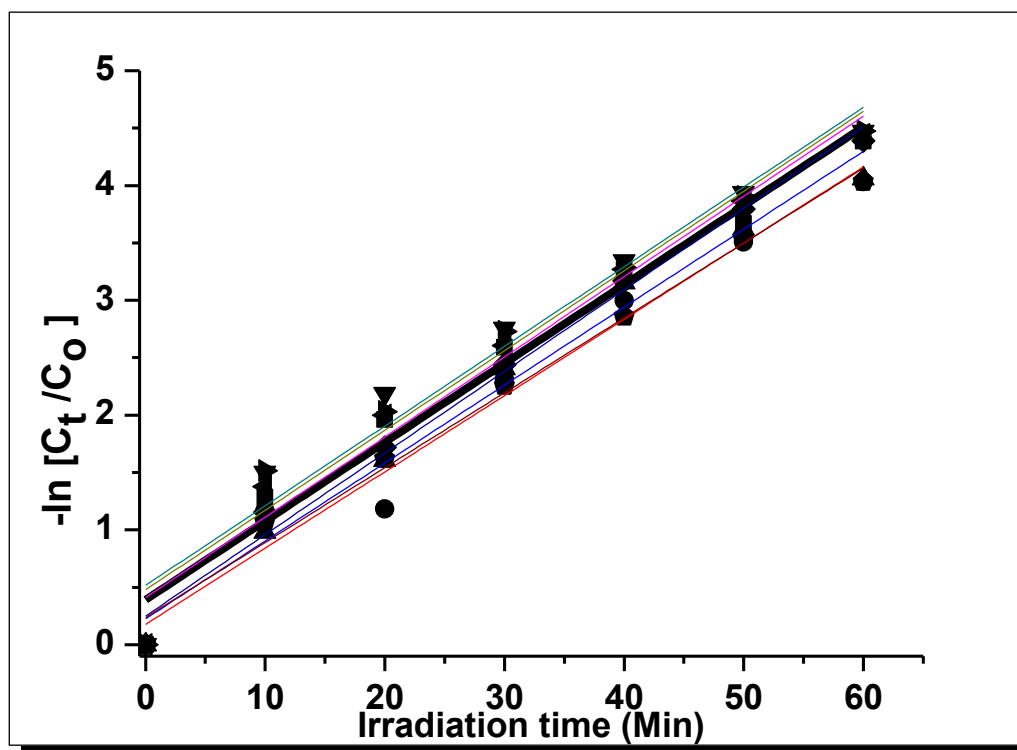
APPENDIX M: CALIBRATION CURVE FOR MB DEGRADATION

Calibration curve for MB degradation
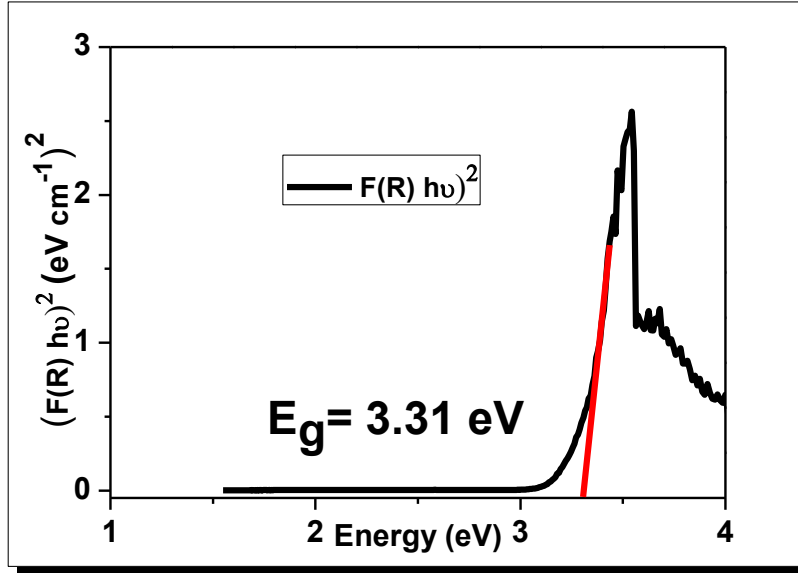
$y = 115260x - 0.0031$
$R^2 = 0.997$
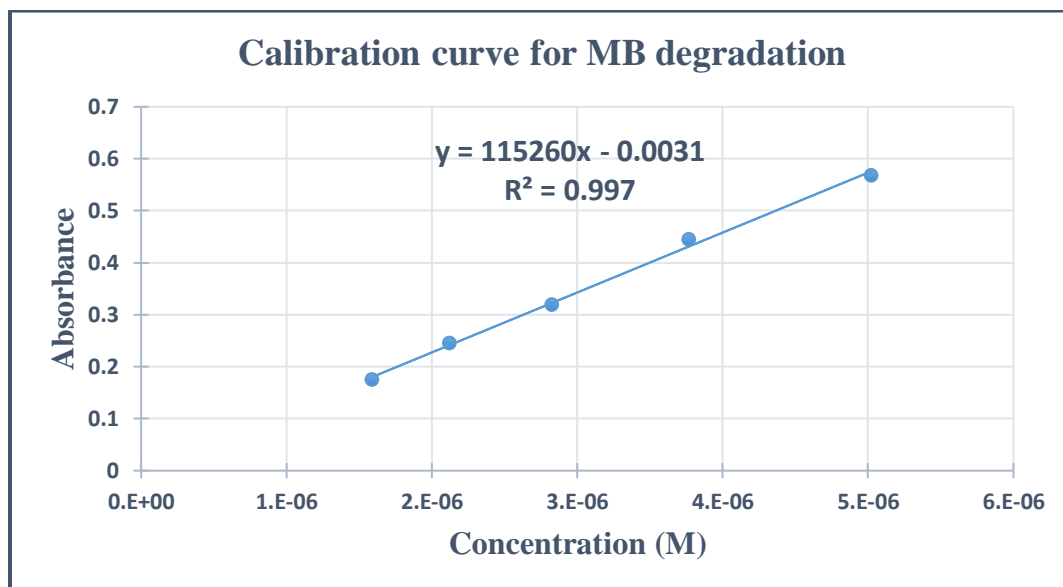
APPENDIX N: LIGHT SPECTRUM OF THE SOLAR SIMULATOR AT AM 1.5
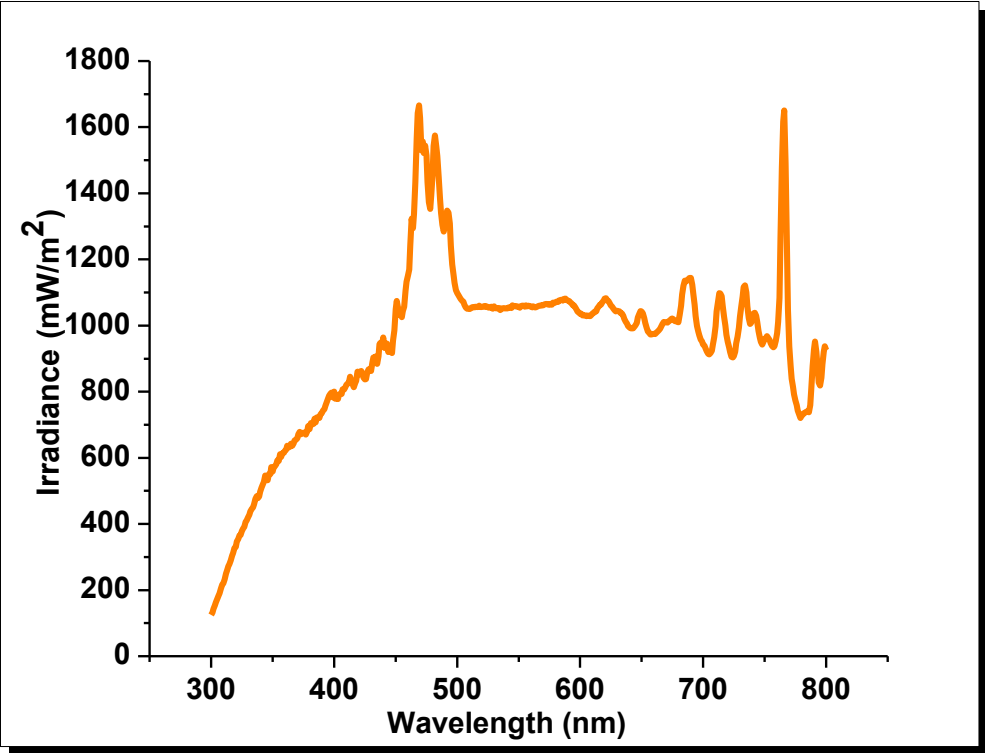
APPENDIX O: KUBELKA MUNK FUNCTION PLOT

Kubelka –Munk function can be used to estimate the optical band gap energy from DRS data.

X- axis	=	$h\nu$	(A1)
Y- axis	=	$(F(R)h\nu)^n$	(A2)
$F(R)$	=	$Kubelka + Munk\ function\ \dfrac{K}{S}$	(A3)
K	=	$(1-R)^2$	(A4)
S	=	$2R$	(A5)

Where K is the molar absorption coefficient, S is the scattering factor and R is the reflectance of the material.